Multiscale Modeling of High and Low Reynolds Number in Small and Large Volume Volcanic Events.

by

Allison Kubo

A dissertation accepted and approved in partial fulfillment of the

requirements for the degree of

Doctor of Philosophy

in Earth Sciences

Dissertation Committee:

Josef Dufek, Chair

Leif Karlstrom, Core Member

Brittany Erickson, Core Member

Hank Childs, Institutional Representative

University of Oregon

September 2024

DISSERTATION ABSTRACT

Allison Kubo

Doctor of Philosophy in Earth Sciences

Title: Multiscale Modeling of High and Low Reynolds Number in Small and Large Volume Volcanic Events

Worldwide, 500 million people live on volcanoes and face their hazards. At the high Reynolds number end of the spectrum are pyroclastic density currents (PDCs), which are granular flows ranging from bed load to dilute suspension. Due to their mobility, high velocities, and high temperatures, these turbulent events are particularly sensitive to topography and channelization into drainage basins. Understanding the flow transition initiated by overspill from valley-confined PDCs to unconfined PDCs is necessary to mitigate their damage. We present three-dimensional multiphase models using the National Energy Technology Laboratory's Multiphase with Interphase Exchange (MFiX) to model channelized PDCs and establish a link between the generation of overspill currents and channel geometry (width, depth, and curvature). We show that the main overspill mechanism can include significant portions of the insulated underflow layer from the channel, leading to a dangerously hot overspilled current. In all sinuous channel simulations, the underflow of the current becomes superelevated when it encounters bends, potentially overwhelming channel walls. Superelevation of the current increases with channel curvature and decreasing channel width, but is underestimated using traditional estimates of superelevation due to the lack of a free surface in these flows. Meanwhile, in the low Reynolds number regime, dikes transport magma from reservoirs to the surface. Large Igneous Provinces are the largest known magmatic events and are associated with strong climate perturbations and mass extinctions. Huge amounts of magma and gases are transported by a crust-spanning dike system. However, spatial complexity, protracted emplacement history, and uneven surface exposure typically make it difficult to quantify patterns in dike swarms on different scales. First, we address this challenge using the Hough Transform to objectively link dissected dike segments and analyze multiscale spatial structure in dike swarms. We show that for both the Columbia River Flood Basalts and Deccan Traps, a single radial or circumferential swarm does not accurately characterize the data. Finally, apply state-of-the-art computer modeling to cooling dikes using Idaho National Lab's Multiphase Object-Oriented Simulation Environment (MOOSE) porous flow and Navier-Stokes modules. We investigate the effect of advective heat transport in the partially molten dike. We calculate the effective heat conductivity with a hydrothermal system over time. This dissertation includes previously published co-authored material.

CURRICULUM VITAE

NAME OF AUTHOR: Allison Kubo

GRADUATE AND UNDERGRADUATE SCHOOLS ATTENDED:

University of Oregon, Eugene, OR, USA
University of California, San Diego La Jolla, CA, USA

DEGREES AWARDED:

Doctor of Philosophy, Earth Sciences, 2024, University of Oregon
Bachelors of Science, Earth Sciences, 2018, University of California, San Diego

AREAS OF SPECIAL INTEREST:

computational fluid dynamics
volcanology
multiphase flow

PROFESSIONAL EXPERIENCE:

Research Assistant, University of Oregon, 2018-2024
President, Women in High Performance Computing, 2020-2021
Science Writer, American Physics Society, 2020-2021
Director & Science Lead, Yonder Dynamics UCSD, 2017-2018

GRANTS, AWARDS AND HONORS:

American Geophysical Union Michael Freilich Vizualization Contest Runner-Up, 2021
UO Jay McMurray Scholarship Recipient, 2020
University of Oregon Women in Graduate Science Science Slam Winner 2020
University of Oregon Promising Scholar Grant, 2018

University Rover Challenge John Barranca Award for Outstanding Science Presentation 2018
San Diego Association of Geologists Outstanding Research Award, 2018
Warren College Undergraduate Research Award 2016
GLADE REU Award Recipient, 2016
AMNH Physical Sciences REU Award Recipient, 2015

PUBLICATIONS:

Kubo Hutchison, A., & Dufek, J. (2021). Generation of overspill pyroclastic density currents in sinuous channels. *Journal of Geophysical Research: Solid Earth*, 126(10), e2021JB022442.

Kubo Hutchison, A., Karlstrom, L., & Mittal, T. (2023). Multiscale spatial patterns in giant dike swarms identified through objective feature extraction. *Geochemistry, Geophysics, Geosystems*, 24(9), e2022GC010842.

Hutchison et al., (2024). LinkingLines: Using the Hough Transform to Cluster Line Segments and Mesoscale Feature Extraction. *Journal of Open Source Software*, 9(98), 6147, 10.21105/joss.06147

ACKNOWLEDGEMENTS

I cannot leave it unsaid: the degree to which I am grateful to the people who have shaped my path, walked with me along it, and guided me through it. How can a page explain it all, the depth of my privilege and gratitude? Six years of work, meals made, flights flown, dogs walked, and papers published.

The mentorship of my co-advisors, Leif Karlstrom and Joe Dufek, has helped me flourish as a scientist. I appreciate their rigor, insight, and flexibility in letting me pave my own path. I am indebted many times to Marla Trox for keeping me on target with all things logistical, practical, and emotional. To my friends and labmates: Paul Regensburger, Chris Harper, Helena Machado, Eric Breard, Annika Dechert, Nate Klema, and Kellum Tate-Jones, who have helped me through this work with humor, emotional support, technical support, and encouragement. To my good friends at home and abroad: Kasuni Bodinayake, Rachel Novotny, Alex Smith, Liberty Pugh, and Emily Colicchio. To the Department of Earth Sciences for providing me with a community and academic springboard.

Eager teachers and listeners, my parents have unfailingly supported my academic journey from preschool to doctorate. They helped me learn how to learn through concerted effort, especially in reading, which set a strong foundation for academic exploration. My mother's steadfast emotional, nutritional, and logistical support has been my anchor to reality, sanity, and hope. She is simply my rock. My father has nurtured my curious spirit from my earliest days in Science Olympiad to today through long technical conversations about nuclear power. Their incredible bond and tireless love for my daughter have brought me unquantifiable joy and countless hours of work time.

From beach rock collecting to college field trips to this work, my love of rocks and nature originates with my grandmother, Ila Ringland. Poggy, as her grandchildren call her, taught me to have high standards for myself and my work. Her love of rocks has shaped my life in tectonic ways. From a pocket full of pebbles to a dissertation, she forms ripples throughout my life and my research.

Finally, to my husband, Kirk Hutchison, for his tireless support and grace. My husband has tended to me through nights debugging, tended to our family during conferences, and listened to countless hours of dimensional analysis. He followed me up and down the West Coast multiple times. You have celebrated my smallest victories and encouraged me through the toughest days, never letting me lose sight of my goals. Since we had our daughter, he's shown me a new reserve of patience, compassion, and love. He's hiked with her ever-increasing weight on his back across all of Southern California while I was completing this thesis.

Thank you.

This work is dedicated to to my daughter, Magnolia Pearl. You are my gem.

TABLE OF CONTENTS

Chapter | Page

Chapter Page

LIST OF FIGURES

Figure | Page

Figure Page

Figure Page

Figure Page

Figure Page

Figure Page

LIST OF TABLES

Table Page

CHAPTER I

CHAPTER 1: INTRODUCTION

1.1 The Reynolds Number: A tale of two flows

Over 500 million people live on or around volcanoes (Chester, Degg, Duncan, & Guest, 2000). Pressures of urbanization and natural resource development have increased the exposure and density of people living close to volcanic hazards (Small & Naumann, 2001). A myriad of hazards exist around volcanoes, such as lava flows, ash falls, pyroclastic flows, phreatic eruptions, gas emissions, and landslides. Volcanoes are by their very nature dynamic. One simple way of distinguishing different flows is the Reynolds number. The Reynolds number is a scale which measures how turbulent or laminar a flow is. The formula for Reynolds number (Re) is given by:

$$Re = \frac{\rho v L}{\mu} \tag{1.1}$$

where ρ is the density of the fluid (kg / m^3); v is the flow velocity (m/s); L is the characteristic length (m); and μ is the dynamic viscosity of the fluid (Pa s). In the realm of fluid dynamics, where the interplay of motion and medium takes center stage, there lies a dimensionless quantity that captures the essence of flow: the Reynolds number. Picture the Willamette river meandering through Eugene, Oregon. The Reynolds number, much like a river, charts the journey from orderly to chaotic, from the laminar whispers of a gentle stream to the roaring turbulence of constricted high flow. It is a tale of inertia against viscous forces, a battle between the swift momentum of motion and the drag that seeks to tame it. When the Reynolds number is low, the flow is serene and predictable, akin to the slow, deliberate movement of honey slipping from a spoon. Viscous forces dominate, creating a harmonious ballet of fluid layers that glide past each other in a symphony of smooth, ordered patterns.

As the Reynolds number rises, the flow becomes a dynamic dance, where inertia starts to take the lead. Picture now the roaring river, where water rushes over pebbles and boulders, its path no longer smooth but filled with eddies and swirls, each a testament to the increasing complexity. Here, the Reynolds number reaches a threshold, a critical juncture where laminar grace yields to turbulent fervor.

The Reynolds number is more than just a mathematical construct. It is a bridge between the placid at $Re << 100$ and the wild at $Re >> 1000$, a narrative of how fluids behave under different forces. In the case of pyroclastic flows, the velocities are high and the viscosities are low which leads to $Re \sim 10^6$, a highly turbulent and inertial flow. On the low end, magma flow in dikes has velocities less than or around 1 m/s and high viscosities $\mu \sim 100$ or higher, with a Reynolds number of approximately $Re \sim 10$. Our work spans these two regimes.

1.2 Volcanoes: Multiscale Phenomenon

Understanding these dynamics is crucial when examining volcanic phenomena at different scales. The interplay between extremes in Reynolds numbers exemplifies the diversity and complexity inherent in volcanic systems. Just as the Reynolds number provides insights into fluid behavior, it also frames our understanding of volcanic processes across varying conditions and environments. Clarence Edward Dutton in Geographical and Geological Survey of the Rocky Mountain Region (U . S.) (1880) wrote that:

> Each volcano is an independent machine—nay, each vent and monticule is for the time being engaged in its own peculiar business, cooking as it

> were its special dish, which in due time is to be separately served. We have instances of vents within hailing distance of each other pouring out totally different kinds of lava, neither sympathizing with the other in any discernible manner nor influencing the other in any appreciable degree.

This vivid description underscores the complexity and unpredictability of volcanic systems, highlighting the challenges faced by volcanologists in predicting eruptions and assessing hazards. Given the diverse and unpredictable nature of volcanic hazards, understanding these phenomena requires sophisticated tools. This is where multiphase and multiscale modeling become indispensable. It offers a framework for understanding the intricate and often independent behavior of different volcanic features, enabling the development of more accurate forecasting models. By integrating data from various disciplines, including geology, chemistry, and physics, multiphase models aim to capture the essence of volcanic diversity and dynamism, paving the way for safer and more resilient communities living in the shadow of volcanoes and diving into the physical mysteries associated with the mantle, the physics of magma transport, and the effect of volcanoes on long-term climate. Volcanic eruptions play a significant role in Earth's climate system, with long-term effects that can alter global temperatures and atmospheric compositions for years to decades. Large Igneous Provinces (LIPs) such as the Deccan Traps and Siberian Traps are strongly temporally associated with mass extinctions like the K-T extinction and the largest mass extinction of all time, the end-Permian Extinction (B. A. Black, Karlstrom, & Mather, 2021; Fendley et al., 2019a; Mittal & Richards, 2021a; Self, Widdowson, Thordarson, & Jay, 2006). These large-scale eruptions can significantly influence atmospheric CO_2 levels over geological timescales, thereby impacting global temperatures, ocean acidification, and mass extinctions (B. A. Black et al., 2021). The effects of these eruptions can persist much longer than their duration. The view of many geologists is summed up in this quote from McPhee (1990):

> A million years is a short time - the shortest worth messing with for most problems. You begin tuning your mind to a time scale that is the planet's time scale. For me, it is almost unconscious now and is a kind of companionship with the earth.

To appreciate the excitement, trepidation, and struggle with which we approach the physics of volcanoes and their products, one must try to grasp the staggering dimensions in which we work. The length and time scales of volcanic phenomena reach the inconceivable and require special methods to deal with such vast gaps. Length and time scales of concern range from the micrometer and microsecond—in the roiling base of the pyroclastic flow, two glass particles slam into one another, producing a lineage of daughter particles spanning finer and finer resolution, which race to settle in a far-off deposit—to hundreds of kilometers and millions of years—far below, the mantle groans as the thermal insurgency of a plume rises toward the surface, inexorable and austere. Studying volcanoes is a lesson in long-term thinking. The magma in the reservoir took thousands of years to rise to the near surface and may stay in the reservoir for that time or more. And yet, this understanding also lives with the knowledge that fast-moving pyroclastic flows can erupt and decimate a settlement in only hours. Modeling phenomena at every scale, from ash particle to edifice, is impossible and impractical. We must try to bring the important physics from the small scales, such as turbulent eddy formation, into the models using tools such as scaling analysis or experimental work. We must also attempt to draw large-scale conclusions from the limited modeling available. This is part of the experience of multiscale thinking.

Part of multiscale thinking is the transient nature of phases. Building on the principles of multiscale thinking, multiphase modeling has become a cornerstone of volcanology. This approach offers critical insights into the intricate interactions between gas, liquid, and solid phases within volcanic systems. The essence of volcanology pivots on the cusp of phase change. The disequilibrium of temperatures and pressures drives phenomena. We often deal with systems in which the presence of multiple phases, for example a gas and a solid particle, severely change the dynamics. Consider how even a small weight percent of particles suspended within a gas flow can influence the gas's viscosity (Raju & Meiburg, 1995). This influence is not linear but complex. The introduction of a slightly larger particle plays a role akin to a damper on the strings of a piano, absorbing kinetic energy. This interplay of scales and phases forms the crux of volcanic complexity, reminding us that in volcanology, as in nature, the whole is often staggeringly different from the sum of its parts. Multiphase modeling has emerged as a pivotal tool in volcanology, providing insights into the complex interactions between gas, liquid, and solid phases within volcanic systems. This approach allows for a more nuanced understanding of volcanic processes, including magma ascent, fragmentation, and eruption dynamics. By incorporating physical and chemical properties of magmatic systems, multiphase models offer predictions on eruption styles, magnitudes, and potential hazards. Seminal work such as Cashman, Stephen, and Sparks (2013) has laid the foundation for current methodologies, highlighting the role of multiphase flow in controlling eruption behavior. The integration of computational fluid dynamics, thermal and chemical proxies, analog experiments, and field observations, such as Benage et al. (2014); E. Breard et al. (2016); Dufek, Esposti Ongaro, and Roche (2015), further demonstrates the applicability of multiphase modeling in predicting volcanic phenomena.

1.2.1 Pyroclastic Density Currents.

We will address one of the most dynamic and dramatic hazards around volcanoes in **Chapter Two**: pyroclastic density currents (PDCs), sometimes referred to as pyroclastic currents or flows. These roiling beasts of burden hurtle down the slopes of volcanoes at speeds of 10 to 100 m/s, carrying deadly hot gases and ash that reach $1000°C$. They are some of the most dynamic volcanic phenomena due to the complex play of particle and thermal mass partitioning in the flow. Within the flow, the volume fraction of particles (a term we will continue to refer to often in **Chapter Two**) can vary by eight orders of magnitude, from a dense bed load region to a dilute buoyant suspension (E. C. Breard, Dufek, & Roche, 2019; Dufek et al., 2015; Lube, Breard, Esposti-Ongaro, Dufek, & Brand, 2020). The resulting flow is extremely dangerous due to its mobility and potentially high temperature and pressure. These flows can auto-fluidize due to the production of a "magic carpet"-like gas or due to fragmentation (E. C. P. Breard et al., 2023; Roche, 2012a). The significant changes along the height of the PDC make it sensitive to the wavelengths of topography around it. In **Chapter Two**, we will show how sinuous valleys can cause overspilling of the flow and the resulting hazards. This chapter includes published work with co-authored material.

1.2.2 Dike Swarms.

While **Chapter Two** focuses on the dramatic surface phenomena of pyroclastic currents, **Chapters Three, Four, and Five** shift our attention to the subsurface, exploring the intricate structures and processes of dike swarms across varying scales. Dike swarms are present on all the terrestrial planets and represent the frozen plumbing system of an ancient magma system. They are the afterimage of bright thermal pulses into the crust. When you have big eruptions, it is assumed you must have large amounts of diking into the crust—approximately $2 : 1$ ratios of intrusive to extrusive activity (O'Hara, Karlstrom, & Ramsey, 2020). The transport of magma through the crust is a battle of heat loss against heat production. **Chapter Three** deals with the question of heat loss. In **Chapter Three**, we zoom into a single segment and model the thermal effects of a circulating hydrothermal system around the dike. Permeability, the interconnected pores in the host rock, is a major control on heat loss. This is one example of how the small scale (millimeters) could affect the large scales (kilometers). We extract the effective values for thermal conductivity. This chapter includes unpublished co-authored material. After exploring the thermal dynamics of individual dikes in **Chapter Three**, **Chapter Four** broadens our focus. We will depart from detailed multiphase modeling to examine extensive dike swarms, such as the Cenozoic Chief Joseph Dike Swarm in Eastern Oregon, USA, and the Mesozoic Deccan Traps in India, each encompassing thousands of dike segments. We apply a linking and clustering algorithm to the dike datasets and show that linked packages of dikes reach lengths of $10 - 100$ km, whose methods are the subject of **Chapter Five**. We examine the complex patterns of single dike segments, packets of dikes, and the overall swarm for a multiscale spatial approach to the magmatic system. Additionally, we can quantitatively show that the dike swarms do not follow the pattern of a radial or circumferential swarm associated with a plume head. Instead, the dike swarms show complex overlapping patterns which may represent different stress states over time or localized magma systems. **Chapters Four and Five** contain previously published co-authored material.

CHAPTER II

CHAPTER 2: GENERATION OF OVERSPILL PYROCLASTIC DENSITY CURRENT IN SINOUS CHANNELS

This chapter was previously published in Kubo Hutchison, A., & Dufek, J. (2021). Generation of overspill pyroclastic density currents in sinuous channels. *Journal of Geophysical Research: Solid Earth*, 126(10), e2021JB022442.

2.1 Introduction

Due to their incredible mobility, even over substantial obstacles, pyroclastic density currents (PDCs) are a major hazard to people living around volcanic centers. Much of the uncertainty in the flow path of PDCs is related to the interplay of topographic elements and a highly variable particle concentration field. As noted by simulations and inferences from deposits, PDCs are often density stratified gravity currents and form a particle-concentrated underflow and an overriding dilute region sometimes referred to as the ash-cloud surge (ACS) as seen in Figure 1 (Dufek, 2016; Lube et al., 2020; Sulpizio, Dellino, Doronzo, & Sarocchi, 2014). Large silicic eruptions can produce flows that travel hundreds of kilometers (J. Branney & Kokelaar, 2002; Roche, Buesch, & Valentine, 2016; C. J. Wilson, 1985), while more frequent, small-volume eruptions can initiate flows that travel on the order of tens of kilometers from the initiation point (Bourdier & Abdurachman, 2001; Capra et al., 2016; Flynn & Ramsey, 2020; Fujii & Nakada, 1999; Komorowski et al., 2013; Ui, Matsuwo, Sumita, & Fujinawa, 1999; Voight & Davis, 2000; Zobin, 2018).

Small-volume dense PDCs are particularly sensitive to topographic forcing that can abruptly modify the density stratification and force transitions in their behavior. Most of our understanding of the effect of flow obstacles and topographic effects are garnered from the study of PDC deposits (J. Branney & Kokelaar, 2002; Ogburn, Calder, Cole, & Stinton, 2014; Sheridan, 1979). However, these deposits mainly record the flow conditions at the interface of the flow and the substrate, so there is little record of the complex interactions that occur vertically within the flow. Because measurements within PDCs are scarce and difficult (Scharff, Hort, & Varley, 2019), volcanologists use analog models (Andrews, 2014; Andrews & Manga, 2012a; Dellino et al., 2007; Lube, Breard, Cronin, & Jones, 2015; Roche, 2012a) and numerical methods (Dartevelle, Rose, Stix, Kelfoun, & Vallance, 2004; Doronzo & Dellino, 2011; Dufek & Bergantz, 2007; Esposti Ongaro, Orsucci, & Cornolti, 2016) to investigate the dynamics of PDCs and the ways they interact with topography.

At one time, a PDC may exist as both a dense granular flow and a dilute turbulent suspension in different parts of the flow (Dufek, 2016; Lube et al., 2020). In the dilute regime, turbulent forces and settling of particles dominate, while the dense underflow can exhibit solid-like to gas-like rheologies over time depending on the local volumetric fraction of particles (E. C. Breard, Dufek, & Roche, 2019; Dartevelle et al., 2004; Dufek et al., 2015; Lube, Cronin, Thouret, & Surono, 2011; Roche, 2012a). The dense underflow can rapidly slow due to friction or be highly mobile due to self-generation of elevated pore-fluid pressures (E. C. Breard, Dufek, & Lube, 2018; Lube et al., 2019; Roche, 2012b; Roche et al., 2016). The mass exchange between the suspended load and underflow is an important control on the density stratification. Multiple segregation processes have been suggested, including settling from the suspended load into the underflow (Fisher & Schmincke, 1984; C. J. N. Wilson, 1980), entrainment of air and thermal expansion (R. S. J. Sparks, 1976), and formation of a turbulent boundary layer (Burgisser & Bergantz, 2002;

Denlinger, 1987). Large scale experiments of PDCs have shown that the dilute and concentrated portions of the flow are coupled with low shear between the head of the underflow and the suspended load (E. Breard & Lube, 2017). The concentration gradients and dominant modes of momentum transmission are thought to be particularly important when the gradients are of the same scale as topographic elements. The dense underflow of a PDC is affected by the topography it flows over, and changes in topography such as break in slope effect the runout distance (Sulpizio, Zanella, Macías, & Saucedo, 2015).

Channelization of PDCs, particularly block-and-ash flows (BAFs) into drainage valleys, can impact the runout distance and is associated with increased hazards (Albino et al., 2020; Capra et al., 2018; S. J. J. Charbonnier et al., 2013; Flynn & Ramsey, 2020; Fujii & Nakada, 1999; Macorps et al., 2018; Ogburn et al., 2014; Saucedo et al., 2002; Sulpizio et al., 2010; Woods et al., 1998). Repeated events down the same channel such as seen in the Colima 2015 eruption (Capra et al., 2016, 2018) indicate that these features are important to the evaluation of hazards in volcanoes that see frequent, small volume events. In addition to the dangers of increased runout distances, there have been numerous fatalities due to PDCs overriding the edges of the channel, that is, avulsing, into unconfined areas (e.g. Unzen, 1991; Merapi, 2010; Volcán de Fuego, 2018). During the 2018 eruption of Volcán de Fuego, at least two PDCs avulsed from the channel and into populated zones; these flows displayed complicated overspill and re-channelization processes (Albino et al., 2020; Flynn & Ramsey, 2020).

The detachment of the PDC can occur at the distal reaches of the channelized flow and can inundate communities situated at channel edges or continue for kilometers in the case of rechannelization (Calder, Sparks, & Woods,

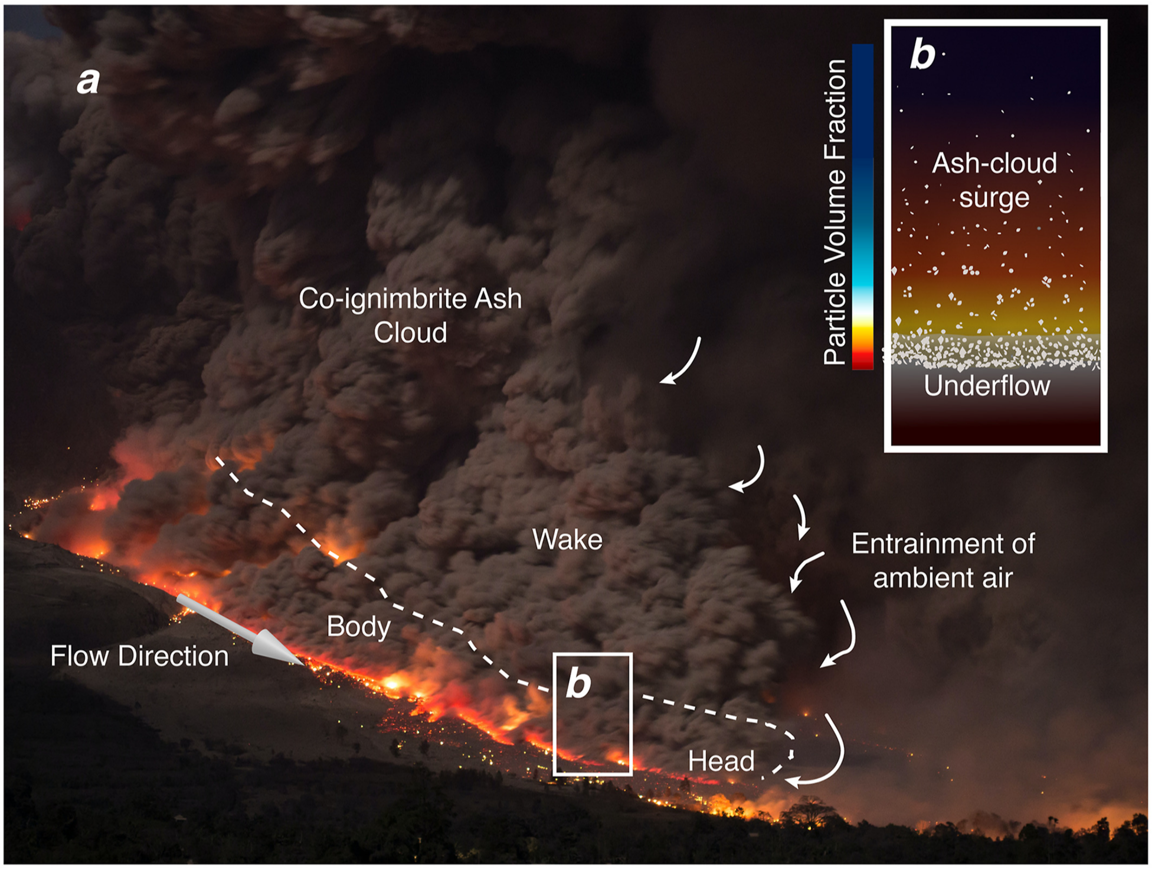

Figure 1. Annotated image of PDC occurring at Sinabung, Sumatra in January, 2014. Photo by Marc Szeglat. (a) The main portions of the flow are the head, body and the wake and co-ignimbrite ash cloud which are produced as the mixture shears and entrains ambient air. (b) Shows an illustration of the internal structure of the PDC which is volumetrically is dominated by a dilute turbulent cloud while the majority of the mass resides in a thin underflow of significantly higher particle fraction. The dilute layer, the ash-cloud surge, is primarily dominated by turbulence and entrainment. The underflow layer, however, experiences little entrainment and is dominated by granular interactions.

1997; S. J. J. Charbonnier et al., 2013; Cole et al., 2002; Flynn & Ramsey, 2020; Loughlin et al., 2002; Ogburn et al., 2014). Propagating at velocities of greater than 10 m/s, these flows can inundate large areas and quickly change hazard conditions (Bourdier & Abdurachman, 2001; Ogburn et al., 2014). Some of the detached surges such as those in the Merapi 2010 eruption have relatively low dynamic pressure (>1kPa) estimated by Baxter et al. (2017), however similar detached surges in 1994 were able to fell trees suggesting dynamic pressure greater than 35 kPa (Kelfoun et al., 2017).

High temperatures are a particular hazard of channelized PDCs which can transport material nearly isothermally from initiation to runout (Trolese, Cerminara, Esposti Ongaro, & Giordano, 2019; Wibowo, Purnama Edra, Harijoko, & Anggara, 2018). The overspilled portions show similar or slightly lower temperatures to the valley confined deposits (Baxter et al., 2017; Pensa, Capra, & Giordano, 2019; Pensa, Capra, Giordano, & Corrado, 2018; Trolese et al., 2018). In the Merapi 2010 eruption, lethal PDCs overspilled at Bronggang, approximately 13.5 km from the summit, causing fatalities both outside and inside homes due to burns (Baxter et al., 2017; Jenkins et al., 2013). The temperatures in the overspilled current and the channelized flow are estimated at 200-300 °C for Merapi (Trolese et al., 2018; Wibowo et al., 2018) and 300-350 °C for the Colima 2015 eruption (Pensa et al., 2019, 2018). These high temperatures suggest that the decoupled current was fed by the insulated dense underflow and not fully detached. Understanding the complex mass exchange between the thermally insulated channelized and the detached PDC is vital to estimate the thermal hazards of the flow.

Predicting avulsion locations, runout of secondary currents, thermal gradient, and velocity structure of these currents is essential to accurately assess these hazards. Small volume events exhibit complex interactions with topography and to mitigate hazards we must understand how PDCs with stratified structure are affected by encountering obstacles. Recent progress has been made incorporating the effects of channelization and topography into hazards modeling (Aravena et al., 2020; Gueugneau, Kelfoun, Charbonnier, Germa, & Carazzo, 2020); however, more work is necessary to investigate the dynamics of overspill and to quantify what topographic conditions lead to hazardous overriding ash clouds. Cole et al. (2002) found that there was no systematic relationship between the volume erupted and the area covered by the dilute PDC suggesting that topography and other initial conditions were the main drivers for detachment. The occurrence of channel overspilling has been related to several topographic features such as decreasing cross-sectional channel area (S. J. J. Charbonnier et al., 2013; Lube et al., 2011; Macorps et al., 2018; Ogburn et al., 2014), break in slope (Bourdier & Abdurachman, 2001; Martí, Doronzo, Pedrazzi, & Colombo, 2019; Valentine, Doronzo, Dellino, & de Tullio, 2011), topographic barriers (Komorowski et al., 2013), and bends in the channel (Ogburn & Calder, 2017).

The mechanism of overspill in stratified currents, including PDCs and turbidites, has been debated with proposals including decoupling of the suspended load from the underflow (flow stripping or splitting) (Piper & Normark, 1983), partial lofting (Gardner, Andrews, & Dennen, 2017), and flow spilling (Lube et al., 2011; Straub, Mohrig, McElroy, Buttles, & Pirmez, 2008). Flow stripping or flow splitting occurs when the upper portions of the flow detach from the body of the current to flow over the topography while the body continues along the channel or is blocked by an obstacle (Piper & Normark, 1983). Partial lofting occurs when the current detaches from the ground after meeting an obstacle and follows a ballistic trajectory before reattaching (Gardner et al., 2017; Hákonardóttir, Hogg, Batey, & Woods, 2003). However, flow spilling or passive overspill occurs when underflow of the current becomes superelevated over the obstacle due to its momentum and the suprachannel portion of the flow spreads laterally from the current. The dynamics of the overspill mechanism will control the initial temperature and density conditions of the overspilled current and the hazards associated with it. We choose to focus on sinuous channels, which are common on highly dissected volcanic terrains such as Merapi, to investigate the avulsion mechanism.

To investigate channelized and overspill currents we apply three-dimensional multiphase numerical models of PDCs after (Dufek & Bergantz, 2007) using a series of idealized channels. We first generalize the dominant channel conditions experienced by small volume PDC by examining a set of well-studied PDC localities on stratovolcanoes. We survey the width, depth, dominant wavelengths and associated amplitudes at six volcanoes. These are used to examine the critical conditions for avulsion and to quantify the amount of material in the overspill and channel compared to reference straight channels and unconfined flow. We examine the mass overspilled, area innundated, and distance travel within these idealized geometries. We also observe the thermal evolution of the channelized and unconfined currents. Finally, we examine the internal dynamics of avulsed currents to better understand the overspilling mechanism and implications with regards to hazards.

2.2 Materials and Methods

2.2.1 Definitions. We define several terms specific to the issue of channelized PDCs. First, the channel referred to here is the entirety of the incised drainage valley including the fluvial channel and floodplain. Second, overspilling or avulsion specifically refers to portions of the current that escape the confines of the channel and are denser than the ambient atmosphere, and hence transported as a gravity currents. In field studies of the overspill PDCs they are separated into two units, a poorly sorted massive overbank deposit and a more fine grained ash-cloud surge deposit (S. J. Charbonnier & Gertisser, 2008; S. J. J. Charbonnier et al., 2013; Cole et al., 2002; Lube et al., 2011; Macorps et al., 2018). First, a poorly sorted unit near the channel is sometimes described as a massive veneer or overbank deposit. For example, field studies have shown that the overspill PDCs can transport large blocks (+1m) out of the channel into the nearby interfluves (Gertisser, Cassidy, Charbonnier, Nuzzo, & Preece, 2012). A second widespread deposit is associated with the ash-cloud surge which is fine grained, often massive and may exhibit cross-bedding and stratification. The overbank deposits overlay or are interbedded with the surge facies. We use the term overspill to encompass the flow states that generate these two deposits since the model does not directly account for deposition. While the rheology of the continuum granular mixture is sensitive to particle volume fraction we do not attempt to resolve deposits and in these single-grain size calculations we do not focus on particle sorting behavior indicative of many deposits (E. C. Breard, Dufek, & Roche, 2019; Dartevelle et al., 2004; Dufek & Bergantz, 2007). Particle and gas mixtures that are able to rise from the channel due to buoyancy are not counted in the overspilled volume and instead we refer to these portions of the current as plumes.

For the purposes of this paper we will use the boundaries delineated by Lube et al. (2020) to refer to the "dense" and "intermediate" and "dilute" ranges of the flow which respectively represent flow exceeding particle volume fraction of $\Phi < 0.3$, the intermediate range spans $0.3 < \Phi < 10^{-2}$, and the dilute range is $\Phi<10^{-2}$. These ranges represent rheological changes in the behavior of the flow, although the concentration limits are approximate and sensitive to particle shape, stress conditions and grain size distribution of the granular material. In the dense regime, friction between particle contacts dominate the rheology and pore pressure feedback can create fluidized flows. In the intermediate region of the flow, particle clustering dominates the settling behavior. In both the intermediate and dense regimes, four-way coupling between particle and gas occur however in the dense regime there is prolonged contact between particles. In the dilute regime, beginning at $\Phi \approx 10^{-2}$ particles experience two-way and one-way coupling as the volume fraction decreases to $\Phi \approx 10^{-6}$. At very low particle concentrations drag dominates. Large scale PDC experiments have observed all three regimes coexisting in a variety of flow conditions (E. Breard et al., 2016). We will also refer to the dense basal part of the PDC as the underflow which represents a dense, thermally insulated layer (Benage et al., 2014).

2.2.2 Topography Analysis. Erosional channels on the slope of volcanoes are ubiquitous with a range of morphologies shaped by the interaction of volcanic and fluvial processes. To focus the parameter range of our overspill analysis, we performed a survey on the channel forms seen on six PDC producing volcanoes as proxies for volcanoes that produce frequent, small volume PDC: Mount Merapi, Central Java province, Indonesia; Soufriere Hills Volcano (SHV), Montserat; Unzen, Nagasaki Prefecture, Japan; Sakurajima, Kagoshima, Prefecture,

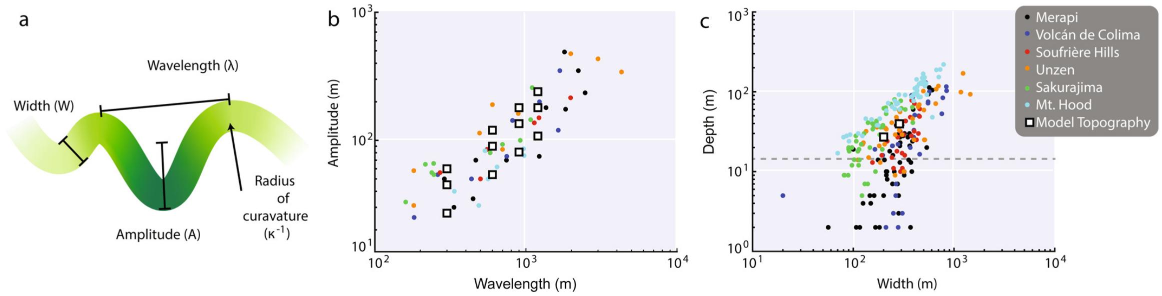

Figure 2. Example of channel measurements used in simulations. (a) An annotated channel showing the width, amplitude, wavelength, and radius of curvature along a sinuous channel. (b) Results of amplitude and wavelength measurements of the 6 volcanoes with the parameters of the idealized models overlaid in the white square with amplitude wavelength ratios of 0.20, 0.15, and 0.09. (c) Results of 184 channel transects with width and depth measurements with the parameters of the idealized models overlaid in the white squares with a single width depth ratio of 7.7.

Japan; Volcán de Colima (Tonaltepetl), Jalisco, Mexico; and Mount Hood (Wy'east), Oregon, USA. This data was used to provide a basis for creating idealized terrains for the multiphase models.

Thirty individual valley forms were quantified using the STRM 30m DEM and georeferenced satellite imagery available in Google ™ Earth Pro (Google Inc., Mountain View, CA) to measure channel length, down valley length, width and depth profiles, and measure the dominant wavelengths (Figure 2). We utilize this dataset due to ease of access, high resolution satellite imagery, and our focus on large scale topographic features on the order of tens to hundreds of meters. Here we do not consider the effects of roughness or fine scale topographic features. The intent of this survey was to develop a range for idealized geometries rather than detailed geomorphic analysis. Based on both the elevation data and satellite imagery, we manually picked the outlines of the channels based on both the satellite imagery and the DEMs and traced the center line to find the channel length. Widths and depths were measured at 100 to 500m intervals along the channel.

Wavelengths and amplitudes, distance from the edge of the channel bend to the channel average centerline, were measured at bends where at least two wavelengths were observable and measurements were averaged across the available curves. We took the maximum depth of the channel at the cross-sections. The Google Earth digital terrain model (DTM) which is derived from the STRM 30m DEM has vertical errors between ±9-16 m depending on the slope of the area (Richard & Ogba, 2016; Werner, 2001) but is accurate for the X-Y plane (Zeba, Rehana, Meghwar, Jatoi, & Shaikh, 2017). Our survey shows that maximum channel depths are strongly associated with channel widths in these dominantly fluvial channels, although they varied significantly from channel to channel and along their downstream length. Approximately seventy percent of channels have an aspect ratio ($\frac{W}{D}$) of between 5 and 15. Although the average channel depth was 33.7 m the distribution shows that much deeper channels (+50m) while relatively less prominent were also observed. Channel sinuosity is measured as the ratio of the curvilinear length and the Euclidean distances of the channel, and had values between 1.08 and 1.26 with an average of 1.13. There were observed wavelengths of features between 150 m and up to 1900m. There is a clear correlation between wavelength and associated amplitude and generally, the wavelength is 4-10 times the amplitude. The average slopes of the channels varied between 9 and 19 degrees with an average of 10.2.

Based on the survey results, we build a range of topographic parameters to utilize in 3D multiphase modeling of idealized channelized flows as described in Section 2.3. The slope (10 degrees) is held constant to focus our analysis here on the impact of channel curvature on avulsion and to isolate this effect from change in slope effects that may also cause avulsion events. We choose to focus the majority of our parameter variation in the wavelength and amplitude ratio parameter space to investigate the effect of curvature specifically. To generate simple idealized sinuous channels, we employ a sine curve with set wavelength and amplitude-wavelength ratios and use a rectangular shaped channel. The measured channels exhibited a variety of channel shapes from U-shaped common on Mount Hood to more V-shaped channels. We test a rectangular shaped channel, which was observed at all volcanoes although not all channels, to isolate how the vertical stratification is affected by hitting the abrupt sinuous edges of the channel. We test two widths, five wavelengths (one being a straight channel with infinite wavelength), and three wavelength-amplitude ratios totaling in 24 sinuous channel geometries and 2 straight channel geometries. In Figure 2, we indicate the simulation topographic properties (white squares) within the range of natural terrains observed in our survey. This is not meant to span all possible channel geometries as natural channels are far more complex in shape, but to ground the simulations in the physical world and provide a basis for comparison. For each geometry, we apply different flow inflow heights to establish the effect of initial flow height compared to channel height and to simulate eruptions of different magnitude.

2.2.3 Multiphase Modeling. Various numerical approaches have been applied to the dense and dilute concentration regimes in PDC. In the dilute regime, workers have applied a box model approach where flows are assumed to be well-mixed with constant or no entrainment (Bursik & Woods, 1996; Dade & Huppert, 1995, 1996). Depth-averaged models focus on granular flow (Esposti Ongaro, Cavazzoni, Erbacci, Neri, & Salvetti, 2007; Esposti Ongaro et al., 2008; Kelfoun & Druitt, 2005; Kelfoun et al., 2017; Patra et al., 2005) in either a single or coupled two-layer models which incorporate a dilute and dense layer and a parameterization for entrainment and exchange between layers (Doyle, Hogg, Mader, & Sparks, 2008; Kelfoun et al., 2017; Shimizu, Koyaguchi, & Suzuki, 2017). These models are advantageous for hazard modeling and provide constraints on run-out distances and areas inundated by implementing high-resolution digital elevations model. In contrast, multiphase models of PDCs can be used to explore how vertical concentration gradients evolve within the flow (Benage et al., 2014; Dartevelle et al., 2004; Dufek & Bergantz, 2007; Esposti Ongaro et al., 2016). Multiphase models do not implement assumptions about entrainment or density profiles, but rather these emerge as outcomes of the conservation relationships. Large computation demands limit the resolution and domain size of multiphase models; however, they are a powerful tool for delving into the internal dynamics of PDCs and can be used to explore thermal and density changes within the flow.

In a channelized flow which collides with obstacles, the investigation of vertical heterogeneity in is essential. We apply three dimensional multiphase numerical simulation to simulate flows over the idealized topography to evaluate vertical structure. We employ the National Energy and Technology Lab Multiphase Flow with Interphase Exchange (MFIX) (Syamlal, 1998) in methods outlined in detail in Dufek and Bergantz (2007) and Benage et al. (2014) using an Eulerian-Eulerian approach where the equations of momentum, mass, and energy are solved for two phases, representing water vapor and a single solid particle component. Water vapor is used as the interstitial gas phase since it is generally the most abundant volatile phase in explosive eruptions. Each phase is treated as an interpenetrating continuum in each control volume where the solid phase is able to move separately from the gas and can both accumulate and dilute due to settling, drag, and turbulence. Density of the gas phase is determined by the ideal gas law assuming water vapor while the bulk current density is calculated using a mixture model. Entrainment of the ambient gas can cause the bulk current density to change and is not set by a single entrainment coefficient. Entrainment is defined as the flux of gas perpendicular to the isosurface of equal solids volume fraction (Ellison & Turner, 1959; Morton, Taylor, & Turner, 1956; Turner, 1986). This method will allow the entrainment to evolve due to flow conditions and interactions with the topography. Of particular interest is how the stratified flow impacts topographic obstacles and how this will modify entrainment.

The initial conditions were chosen to reflect small volume pyroclastic density currents as exemplified from numerous events at Merapi, SHV, Volcán de Colima, or Unzen. However, we did not try to match the dynamics of any single eruption. All simulations begin with the same initial temperature for the gas and solids ($T = 800K, 527°C$). This temperature was chosen to reflect peak emplacement temperatures established from temperature proxies such as thermal remnant magnetism (Aramaki & Akimoto, 1957; Sulpizio et al., 2015), charcoal reflectance (Hudspith, Scott, Wilson, & Collinson, 2010; Pensa, Porreca, Corrado, Giordano, & Cas, 2015), textural clues such as bread crust bombs (Benage et al., 2014), or field evidence such as melted plastics or eyewitness accounts (Baxter et al., 2005; Jenkins et al., 2013; Loughlin et al., 2002; Voight & Davis, 2000). These temperatures are lower than eruptive temperatures due to entrainment before the initiation of the PDC as in column collapse or before emplacement due to topographic effects (Benage et al., 2014; Trolese et al., 2019, 2018).

The initial conditions are set to mimic an initially low velocity and high concentration current similar to low column collapse, dome collapse, or spatter fed PDC (Calder et al., 1999; Komorowski et al., 2013; Loughlin et al., 2002). We set the initial velocity (U_0) of the gas and solid as 10 m/s to allow the current to gain velocity from the slope and channel geometry and allow it to evolve over time. The initial particle volume fraction is set to 0.6 for the inflow. We employ a single particle size with a drag relationship equivalent to spherical particles with a diameter 50 µm and a density of 1950 kg m^{-3}. The chosen density lies between common ranges for pumice (700 − 1200 kg m^{-3}) and glass shards which consists of mainly pumice fragments composed of pure glass and minor crystal or bubble contents 2350 − 2450 kg m^{-3}) and is consistent with several BAFs (Komorowski et al., 2013). This is also consistent with Sauter mean diameter (area weighted particle mean diameter) of polydisperse PDC mixtures (E. C. Breard, Dufek, & Roche, 2019). This yields a Stokes number (St) of order 10^{-3} where the Stokes number is defined as the ratio of the particle timescale (t_v) to the fluid timescale (t_f):

$$St = \frac{t_v}{t_f} = \frac{\rho_p d^2 U_0}{18 \mu D} \tag{2.1}$$

where ρ_p is the particle density, d is the particle diameter, μ is vapor viscosity, U_0 is the initial velocity, and D is the characteristic height, in this case the channel depth, as a proxy for the largest eddies in the current (Burgisser et al., 2006). The particles have a settling velocity of 1.2 m/s in water vapor. The Stokes number of 10^{-3} leads to small slip velocity between particles and fluid and flow stratification occurs due to gravity and concentration is modulated by the unsteady behavior associated with drag (Raju & Meiburg, 1995). The particles have a fall velocity of 1.4 m/s in air and the simulation becomes stratified within 5s from inflow. Real flows show a large range of particle size spanning bombs and blocks to fine ash $St \approx 10^{-3}$ to 10^{1} ; however, we employ a single particle size to isolate the effect of topography on the flow stratification. Polydispersity is an important aspect to the rheology of PDCs and may act to increase fluidization (E. C. Breard, Jones, et al., 2019; R. S. J. Sparks, 1976; Sulpizio et al., 2014). In these simplified calculations we use Sauter mean diameters in the range of natural mixtures, but more detailed effects associated with sorting in polydisperse mixtures were not examined.

One challenge for models of dense granular flows is that the rheology of dense granular mixtures, especially polydisperse mixtures, is difficult to capture with constituent equations (Delannay, Valance, Mangeney, Roche, & Richard, 2017; Lube et al., 2020). Recent benchmarking of MFIX in 2D has indicated that for monodisperse and bidisperse particle mixtures the model can match experiments in the dense regime (E. C. Breard, Dufek, & Roche, 2019). We choose a resolution (3 m) significantly less than the height of the flow (50m) to enable modeling of the basal dense granular avalanche. This grid spacing allows us to investigate large scale topography features while still resolving the internal stratification. The total domain size is 1200 m by 900 m by 450 m which resolves multiple bends of the sinuous channel and 230-330 m on each side of the channel for the overspilled current to propagate. Due to the high resolution and size, the temperature, volume fraction, velocity vector, gas pressure are recorded for the whole domain every 5 s for a total of 35 s.

The simulations span a range of volume flux of between 7200 and 32400 m^3 /s. The simulations volume flux is determined by the width and depth of the channel so that each inlet is equal to the channel width, to avoid dilution, and the ratio of height of the inlet and height of the channel is varied at either a ratio of initial inflow height to depth of the channel (H_i) as 0.4 or 0.7. With the same initial velocity, this yields two different volume fluxes for each geometry. This tests how the initial height of the flow relative to the depth of the channel changes the overspilled current. For comparison, the volumes erupted in the simulations fall in the upper half of the range of BAFs as surveyed by Ogburn (2012) and is consistent with volume flux of PDCs (Calder et al., 1999; Gueugneau et al., 2020; Komorowski et al., 2013).

We ran a total of 53 simulations over 26 geometries with two volume fluxes and one unconfined flow (Table S1). In all simulations, the initially well mixed mass inflow segregates into a stratified flow. After approximately 10 to 15 s, or 100-200m from initiation, the flows segregate into a thin underflow, thickness on order of meters and a dilute volumetrically dominate layer. The initial inlet is set to the width of the channel to avoid dilution at the beginning of the simulation which would significantly cool the current. The simulations range several order of magnitude in volume fraction solids (0.4 to 10^{-7}) . The volume fraction of solids measures the fraction of each grid cell (9 m^3) filled by the solid particles described above. The bulk density of each cell is determined using a mixture density of the solid particles and gas density calculated by the ideal gas law.

We calculated a proxy for entrainment, volume change over time, for different particle volume fraction isosurfaces ($\Phi \approx 0.3, 10^{-2}, 10^{-6.5}$) of the flow by taking the difference in volume between timesteps, after the mass inflow finishes at 15 s. Since there is no deposition or erosion in the model the change in volume represents the volume of gas entrainment and subsequent thermal expansion of entrained gas. We will refer to the volume change as proxy entrainment as it is not a direct measure of flux of gas into the current.

Distance traveled is measured along the channel; thus for straight channels the maximum distance is the length of the domain but for sinuous channels it is larger. Dynamic pressure is used to estimate the physical damage due to these currents (Baxter et al., 2005; Clarke & Voight, 2000; Gardner et al., 2017; Valentine, 1998). We calculate the dynamic pressure as:

$$P = \frac{\rho_c U_s^2}{2} \tag{2.2}$$

where ρ_a is the bulk density of the current U_s is the magnitude of the solids velocity combining all components.

To determine the Froude number of the current, first the height of the head was identified by a dilute isosurface of $10^{-6.5}$ particle volume fraction and averaged over the width of the channel. Where the Froude number is defined as:

$$F_d = \frac{U}{\sqrt{\frac{\rho_c - \rho_a}{\rho_c} gH}} \tag{2.3}$$

where U is the depth averaged velocity of the current (m/s), ρ_a is the ambient fluid density (kg/m^3), and H is the height of the head (m).

2.3 Results

We first focus on three example simulations with the same volume flux: an unconfined flow, a straight geometry (label: SV7, 200 m wide, 27m deep) flow, and a sinuous geometry (label: BVY7, 200 m wide, 27m deep, 600 m wavelength, 90 m amplitude) flow as seen in Figure 3 to illustrate the general dynamic evolution of these multiphase currents. In particular, we examine the evolution of gradients in velocity, density and temperature. Then we compare the mass overspilled, distance traveled, area inundated and the magnitude of cross-stream velocity in separate simulations.

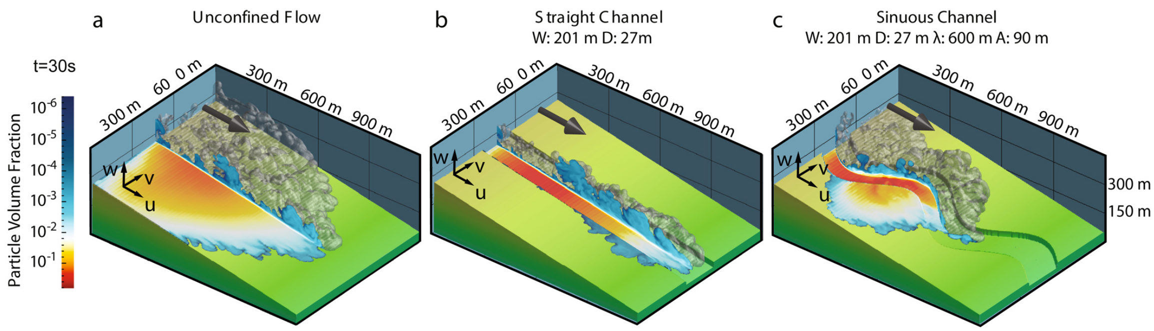

Figure 3. Simulation results for three geometries (UNCON7, SV7, and BVY7 respectively) at the same volume flux and timestep (30 s). The color bar indicates particle volume fraction in a negative log scale and the grey isosurface is set at 10−8. (a) Shows the unconfined flow. (b) Shows a straight channel (SV7 W:201 m, D:27 m) where the simulation stays within the bounds of the channel except for minor dilute billows. (c) Shows a sinuous channel (BVY7 W: 201 m, D: 27 m, λ: 600m, A:90) with significant overspill from the edges of the channel some of which is dense and hot.

2.3.1 Unconfined Flow. In the unconfined flow, the simulation quickly spreads along the flat topography (Figure 4). Due to the spreading, the current did not maintain a dense underflow layer for the entire simulation and by 30s there were no cells with volume fraction above the dense cutoff value. The underflow of the current lags behind the more dilute front of the current in the unconfined simulation by 300 m at 30 s. Despite being unconfined the flow was able to flow to a distance of 1100 m from the inlet over the simulation time of 35 seconds. At the end of the simulation the flow did not show signs of liftoff which would indicate it had reached its runout distance and likely could continue on past the cutoff of the simulation. The average height of the head was 45 ± 7 m leading to a ratio of head to current body height of 2.5.

2.3.2 Straight Channel. Straight channels were able to transport material in the underflow nearly isothermally from initiation. The height of the underflow was measured in the channel based on an isosurface of 0.3 particle volume fraction and for all straight geometries did not exceed 9 m with the majority measuring only 3 m. Entrainment was not efficient enough to cool the underflow. Even outside the underflow, the lower 12 m of the flow maintained hot temperatures (<500 °C) in both the head and body of the current (Figure 4b). These temperatures are maintained up to a particle volume fraction of $\Phi \approx 10^{-3}$ and decrease linearly to the edge of the current with an average of approximately 250 °C within and above the head of the current. The flow generates clear Kelvin-Helmholtz instabilities along the interface between the flow and the ambient air. These billows are quite dilute generally with an average particle volume fraction of less than 10^{-3}. Entrainment occurs along these billows and along the backside of the head (Andrews, 2014). An average temperature of $250°C$ indicates a mixing ratio of hot pyroclastic gases and cold ambient air of approximately unity indicating efficient entrainment in the billows.

The head of the current (grey line Fig 4b) is more well-mixed than the body of the current which displays a sharper concentration gradient. The height of the head varied between 40 m and 50 m depending on simulation and remained steady over time after 10s. To investigate the degree of fluidization, we take integrated weight of the current divided by the gas pressure times the cell area. The body of the current is more fluidized than the head with up to 20% of the current weight supported by gas pressure compared to >5% in the head. Using the height of the head and the depth averaged velocity of the current (30 m/s), we calculate a Froude number of approximately 1.2 for the example flow. This is consistent with inviscid gravity currents with Froude number near unity (Simpson, 1987). The straight channels develop billows around the head that do reach out of the edges of the channel but do not propagate outside the channel as an overspilled current.

The straight channels flows had the highest velocities and all straight geometry simulations hit the edge of the domain within 30s. Before hitting the edge of the domain, all straight channel geometries travel over 1000 m. As part B of Figure 3 illustrates, the dense underflow of the current lags behind the head in this case by up to 300 m. Simulations of higher volume flux produce slightly taller dense underflows of up to 9 m but the height of the head remained between 40 – 50 m for all straight simulations approximately 1.25-1.5 times the depth of the channel. As they flow the velocities increase from 10 m/s to up to a peak velocity of 55 m/s in head of the current. The maximum velocity of the simulation, 55 m/s was offset from the base of the flow occurring between 9-12 meters ($0.20H_c$). The maximum dynamic pressure reached 100 kPa at 5 m ($0.1H_c$) from the base of the flow in the body of the flow. The dynamic pressure max was offset from the velocity max due to the density gradient in the flow.

2.3.3 Sinuous Channel.

A pervasive feature of all the sinuous channel simulations was overspill features along the channel margins. Overspill is focused along the inflection point of the curve approximate $.25\lambda$ to $.75\lambda$. There can be multiple overspill events at a single timestep at multiple locations in the channel. These overspilled currents are able to travel hundreds of meters from initiation in the duration of the simulation. The overspill currents are stratified showing a more concentrated underflow and voluminous dilute billows above (Figure 4 g-j, gray line). Both the density and temperature gradient of the overspilled current is stratified. Sampled 100 m from the edge of the channel, there is a thin layer of higher particle volume fraction $\Phi \approx 10^{-2}$ followed by a decrease to a semi-constant value 10^{-4} indicating the presence of well-mixed billows above the main body. Due to their low particle volume fraction the overspill currents were highly mobile but showed lower pore fluid pressure than in the channel. While the temperatures in the overspill remained hot ($> 500°C$) for the lower ten meters of the flow then rapidly cool to $100°C$ in the well mixed billows above the current. These plumes are on average $150°C$ lower in temperature than the dilute billows associated with the head of the straight channels indicating significantly more mixing of ambient air. The height of the head is approximately 20 m but can be difficult to distinguish by visual inspection due to the plumes associated with overspill. The downstream velocity (U) reaches up to 30 m/s in the overspill, with a depth-average velocity of 20 m/s, and in some cases was higher than the depth averaged velocity in the channel. Based on the height of the head and depth-averaged velocity 100 m from overspill initiation, the Froude number is estimated at 1.5, slightly higher than the straight geometries. Currents reach a maximum dynamic pressure of 10kPa, 5 m ($0.25H_c$) from the top of the topography. This low dynamic pressure but high temperature is consistent with observations from the damage and causalities in the 2010 Merapi eruption (Jenkins et al., 2013).

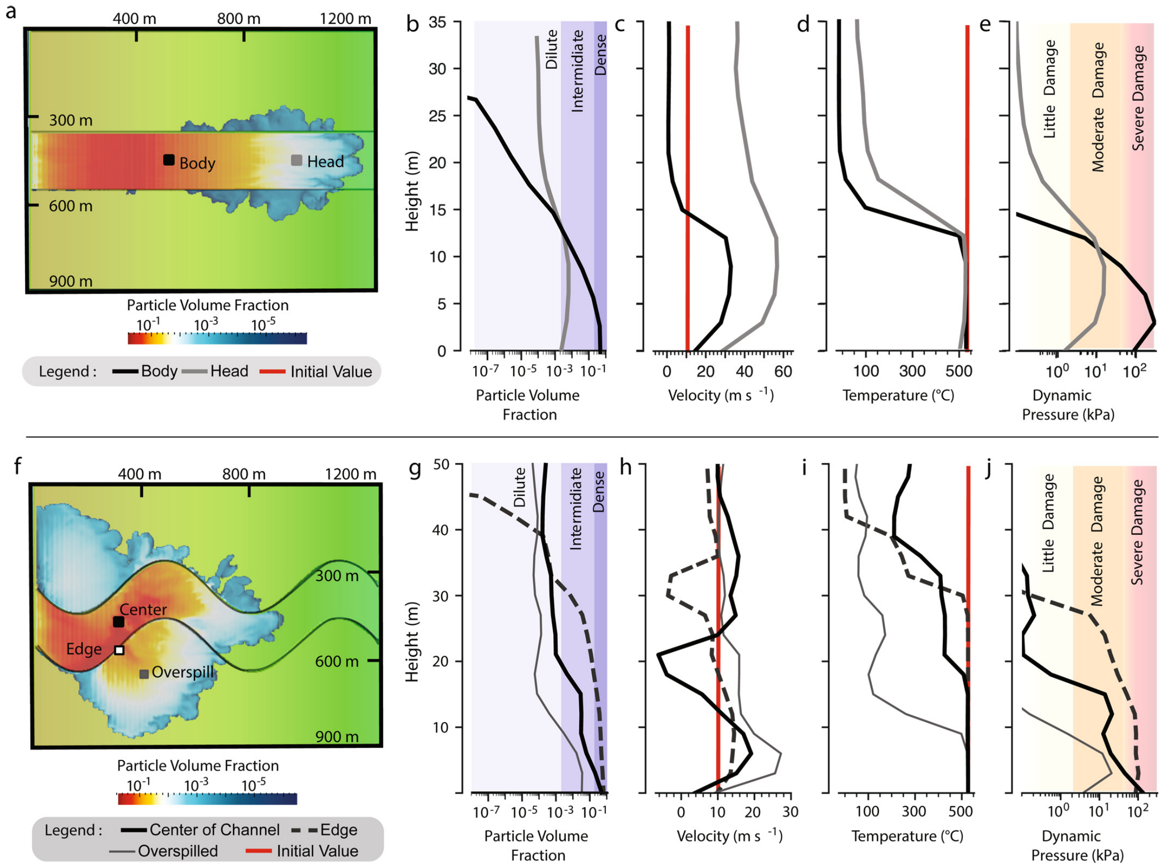

Figure 4. Simulation results for a straight channel and sinuous channel at a time of 30 seconds showing the vertical stratification of particle volume fraction (b,g) , velocity (c,h), temperature (d,i), and dynamic pressure (e,j) with estimation of damage from Baxter et al. [2005]. (a, f) Show a map view of a straight and sinuous channels respectively where the colored regions indicate the particle volume fraction 5 m above the surface of the topography. The marked locations indicate the position of the sampled profiles in b-e and g-h.

Within the channel, the underflow layer does not follow the centerline of the channel and instead flows straight into the edge of the channel and then is reflected off the edge and hits the other edge of the channel in a “zig-zag” motion. The dense underflow lags behind the front of the current and often spans between two bends of the sinuous channel (Figure 4f). At the overspilling edge the current in the lower 10 m, up to half of the current weight by is supported by the gas pressure indicating partial fluidization. The center of the channel, at the time it was sampled, showed up to 12% bed support. The level of the underflow is higher on the overspilling side reaching up to 30 m tall whereas in the center only measures 6 m. At the edge of the bend, approximately 0.25λ the underflow of the simulation collides with the wall of the channel and yields the highest dynamic pressure of any point in the simulation where the pressures approach 100kPa for up to 15m from the base of the channel (Figure 4h, dashed line).

The temperature of the flow at this point was over 500 $°C$ for 30 m within in the channel while in the channel the flow maintained near initial temperatures for 20 m (H_c) from the base then decreased to 200° . The height of the underflow here is significantly thicker than those seen in the straight channels reaching over 20 m. In the center of the channel the density gradient is near linear with a thin dense layer at the base. The velocity observed in sinuous channels is less than the maximum observed in straight channels and reaches 30 m/s. In addition, there is an increase in downstream velocity along the edge of the channel where overspilling occurs.

2.4 Discussion

2.4.1 Overspill Mechanism. Our simulations show the underflow layer of the flow hits the edge of the curving channel. This causes material accumulation at the edge of the channel and ultimately overspills when its height reaches the height of the channel. In this wedge (Figure 5i), the temperature remains over 500 degrees for 30m above the topography, leaving 3 m of the underflow over the channel top situated at 27 m. When the underflow impacts obstacles with significant momentum, the flow splashes up and out of the channel and collapses into two parts: the overspilled current that spreads away from the channel and a cross-stream current flowing perpendicular to the primary flow direction. This splash and collapse disrupt the stable density stratification and increases entrainment along the edge of the flow. At the edge of the current, the highest pore fluid pressure was observed. Some compaction against the wall of the channel may increase the fluidization and splash heights. The resulting dilution causes a buoyant cloud to rise at these margins. In simulations with overspill, there is increased production of the buoyant plumes than in the straight channels (Figure 7, green dots) . Impacts with obstacles has been observed to increase entrainment and liftoff (Andrews & Manga, 2012b; Gardner et al., 2017). The underflow colliding with the edge of the channel and reflection of the cross-stream current generates shear stress within the channel. The hot previously insulated portion of the current mixes with ambient air and produces voluminous rising plumes. This overspilling mechanism allows for the hot portions of the current to breach the confines of the channel and significantly increases hazards on the channel edges due to the heat and mobility.

The simulation results are consistent with field evidence from Lube et al. (2011) where workers also observed passive overspilling from the channels associated with sediment-trapping sabo dams. We show the same behavior can occur with a channel of consistent width and depth due to the curve of the channel. In some cases, the cross-stream flow is of sufficient magnitude to cause a secondary overspill on the opposite edge of the channel. This secondary overspill is significantly more dilute ($\Phi >> 10^{-3}$) and colder than the initial overspill due to entrainment as it moves perpendicular to the main channel direction. Despite this, they are still able to propagate away from the channel for hundreds of meters over the course of the simulation. There are at least three sources of deposits related to overspill events described in these simulations: 1) main hot overspill, 2) dilute surge-like secondary overspill, and 3) buoyant plumes co-incident with main overspill at the channel edges. These plumes have low volume fraction particles ($\Phi < 10^{-3}$) and quickly cool due to entrainment of ambient gas then rise buoyantly.

2.4.1.1 Curvature and width as a primary control.

The sinuous channel geometries increase the area inundated, mass overspilled, and cross stream flow compared to straight channels. We introduce a metric for determining whether the channel geometry will increase mass overspilled. We represent this in a normalized form using the wavelength, amplitude, and width:

$$\kappa^* = \frac{\kappa\lambda^2}{W} = \frac{A}{W} \tag{2.4}$$

which in a simple sine curve reduces to a function of amplitude and width. The normalized curvature represents a ratio of the channel amplitude and the width suggesting that as the amplitude relative to the width increases the amount of mass overspilled will increase. Simulations which take place over a range of κ^* show how increasing κ^* increases area inundated and mass overspilled but decreases distance traveled (Figure 6). As overspill events occur, it removes momentum from the current in the channel, it decreases the downstream velocities and the distance traveled. In straight channels the underflow lags behind the head of the current. However, in the channels with high curvature, a portion of the underflow layer is trapped in the bends while the head of the current continues downstream. Lower volume fluxes had lower distances traveled for sinuous channels but small differences in straight channels. It appears there is a critical curvature for overspilling events at approximately $\kappa^* \approx 0.2$ in this simple, idealized geometry after which the mass overspilled increases linearly with normalized curvature. Wide channels with gentle meanders would have relatively less mass overspilled than thin channels with tight curves for similar initial conditions. This work shows that the interplay between width and curvature is important to understanding avulsion; natural channels with changing curvature and width would have complex effects on mass overspilled.

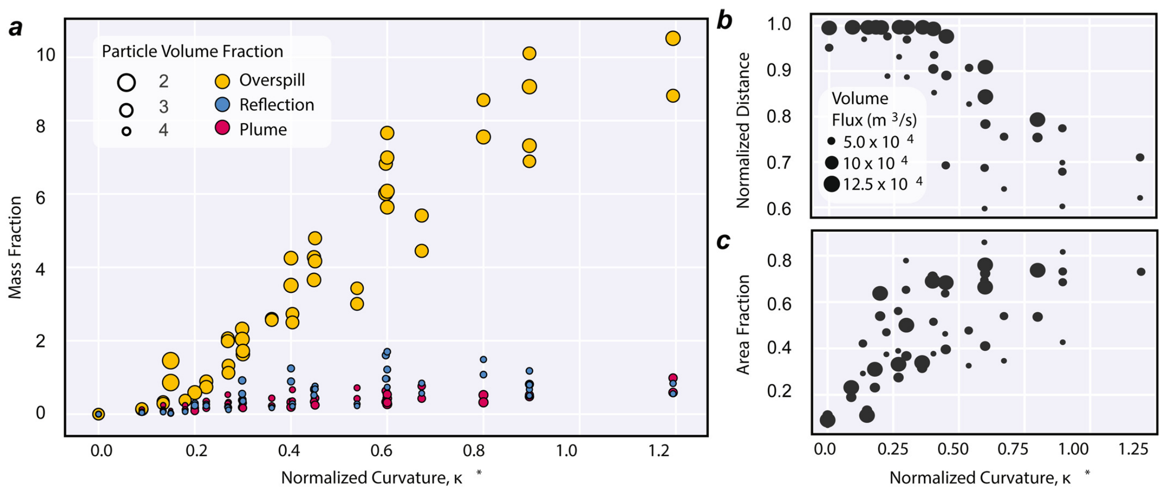

Figure 6. Plots of the normalized mass fraction (a), area inundated (b), and distance traveled (c). The normalized mass fraction of the overspilled (orange), cross-stream reflection (blue), and plume (green) portions of the current is plotted against the normalized curvature where the dot size represents the average particles volume fraction in the respective regime in a -log scale. The normalized mass fraction is calculated based on the amount of mass outside the channel normalized by the total mass in the simulation then divided by Hi which normalizes it relative to volume flux. (b) Shows the normalized distance, the distance from the inlet normalized by the channel length, decreases as normalized curvature increases. (c) Shows area inundated as the normalized curvature increases.

The mass fractions of the flow involved in the total overspill (including primary and secondary), plume, and cross stream reflection within the channel increase with normalized curvature (Figure 6). The mass fraction overspilled is significantly larger than the portion allocated to the plume or reflection. Mass overspilled increases with normalized curvature and it shows a higher volume fraction particles than the other two portions of the current. The reflected portion is a smaller portion of the mass than the overspilled currents. It increases with

normalized curvature until $\kappa^* \approx 0.6$ then decreases. The plume portion represents the smallest portion of the mass and increases with normalized curvature.
The average particles volume fraction in the plume and reflected portions are comparable indicates are both less than the overspilled current. The reflection increases with curvature until $\kappa^* \approx 0.6$ then decreases and the plume mass fraction surpasses the reflection at $\kappa^* \approx 0.6$.

These results highlight the curvature and width as important scaling factors when considering avulsion. However, these simulations represent an idealized channel which neglects changes in width over the channel, topographic roughness, and the effects of deposition and erosion.

2.4.1.2 Superelevation within the channel. We measured the maximum superelevation of the wedge and splash by looking at the top extent of an intermediate isosurface ($\Phi = 0.1$) along the channel from 0.25 λ to 0.75 λ. We found large superelevations and splashes reaching up to 78 $\pm$ 3 m from the bottom of the channel, 39 $\pm$ 3 m from the top of the channel in the channels with the highest curvature. Superelevation height increases as the curvature increases and increases the average density of the overspill current. There are two main contributions to superelevation described in fluvial settings; centrifugal forces contribute as mass moves around the bend and runup due to the kinetic energy of the current converted to potential energy. The first contribution can be described after Straub et al., (2008):

$$Y = \alpha \frac{\kappa W U^2}{2 \frac{\rho_c - \rho_a}{\rho_c}} \tag{2.5}$$

where α is a parameter near unity (Engelund, 1974) and Y is the superelevation (m). This is based on two assumptions, first the fluid must remain contained in the channel and second the streamlines should run parallel to the channel centerline. Using the average densities (590-785 kg m^{-3}) and average velocities (10-19 m/s) within the underflow current one timestep before the largest superelevation incident within the channel, the contribution from centrifugal force alone cannot account for the observed superelevations. These estimations underestimate the superelevations by up to a factor of 5. The second contribution from runup can be expressed as :

$$Y = \frac{\rho_c U^2}{2g\left(\rho_c - \rho_a\right)} \tag{2.6}$$

by solving for the conversion of kinetic into potential energy. Using the same values from above we can calculate the contribution from runup and find that it also underestimates the superelevation and splash heights by up to 5 times. We compare our results with experimental studies of superelevation in turbidity currents using a curved sinuous channel which show similar scaling properties to the PDC numerical studies. This is similar with Straub et al. (2008) which found superelevations of higher than predicted by either standard momentum balance or centrifugal force. We also found that the mismatch between the expected values and the observed values increases in intensity as curvature increases. This increase in the observed values relative to the scaling relationships above is more pronounced after $\kappa^* \approx 0.2$, the critical curvature level. This understanding of superelevation does not accurately capture the more complex physics of multiphase currents due to the lack of the free surface. Our three-dimensional simulations reveal that the body of the current does not follow the center line of the channel and rather is reflected by the curves which violates the assumptions of these equations.

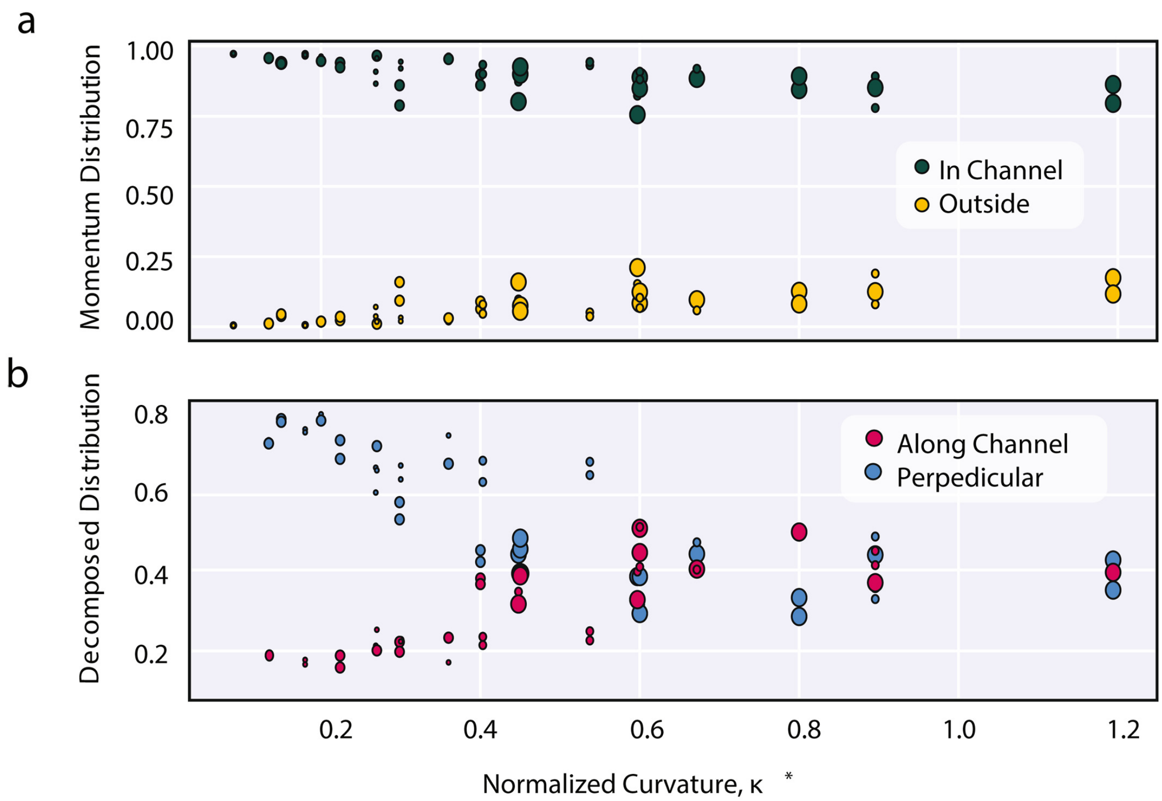

Figure 7. The results of the simulations momentum distribution plotted against normalized curvature at a time of 20s . (a) Shows the total momentum within the channel and outside the channel. The total momentum within the channel decreases to about 0.8 as normalized curvature increases. This momentum is transferred to outside of the channel to a maximum of 0.10. (b) Shows the decomposed momentum distribution of component along the sinuous channel and component perpendicular to the wave of the channel.

One feature not included in the model is valley filling due to PDC deposition. Deposition may make it much easier for a PDC to avulse by building up the ramp to the edge of the channel. Field studies indicate that deposition of between 1-15 m can occur in channelized flows (Bourdier & Abdurachman, 2001; Gertisser et al., 2012; Komorowski et al., 2013). This feature would be most significant for successive PDCs down the same channel and should be considered when modeling more realistic systems. In our simulations, considering the limited duration of the flow (30 s), the particle settling velocity (1 m/s), and scale heights of the current (30-50 m) we do not estimate that deposition will be major in the simulation. Deposition could also result from jamming in the dense, granular regions of the flow and in the continuum approach there will always be some non-zero velocity. However, over simulations durations such a small amount of deformation compared to the current velocity would act effectively like a deposit from the perspective of the flow. Additionally, erosion within the PDC has been shown to increase runout distances through the addition of mass (Albino et al., 2020; Bernard, Kelfoun, Le Pennec, & Vallejo Vargas, 2014). Erosive behavior in PDCs has been linked to the slope it flows over with higher slopes (10°) leading (Calder, Sparks, & Gardeweg, 2000; Cole et al., 1998; R. S. Sparks, Gardeweg, Calder, & Matthews, 1997) and to pore pressure where erosion occurs via an upward pore pressure gradient that can entrain coarse particles (Brand et al., 2014; Roche et al., 2013). Our results suggest that width is an important scaling factor to consider which is less likely to be significantly altered by deposition and erosion. However, more work is necessary to better account for deposition and erosion in the context of multiphase numerical models especially those with larger length and time scales.

We employ a rectangular shaped channel which may change the degree of superelevation. However, we argue that this mechanism would likely still be present in a more gently sloped channel walls. Superelevation and runup are observed in many field sites with curved or sloped channel walls (Druitt et al., 2002; Lube et al., 2011; Macorps et al., 2018). However, the superelevation may be less dramatic depending on how momentum is partitioned in the channel due to interaction with the angled valley walls.

Analysis of the momentum distribution in the channel suggest a momentum capacity where channels can contain the runup of the underflow layer only to a certain momentum set by specific geometries (width, depth, shape, curvature). Overall the majority of momentum stays within the channel (>75%) while the overspilled currents represent up to 23% of total momentum (Figure 8) . Some of the momentum is converted to buoyant momentum but due to the dilute nature of the plumes this proportion is small ($> 7\%$). The momentum capacity occurs with the critical curvature at $\kappa^* \approx 0.2$ when the proportion of momentum perpendicular to the channel centerline show a maxima at 0.8. At low normalized curvature, the width of channels is high compared to their amplitude which allows the channel to contain more perpendicular momentum without overspilling. As curvature increases or width decreases the momentum pointing out of the channel is removed from the channel system increasing the momentum in the overspill. However, considering that the overspill represents a small portion of total momentum a larger portion of the perpendicular momentum is redirected into along channel momentum. The allotment of perpendicular and parallel momentum components reaches parity at $\kappa^*0.6$ where after the along channel momentum dominates the remaining flow within the channel. At $\kappa^* \approx 0.6$, we also see decreased portion of momentum in the reflected current (Figure 6, blue dots) but increasing mass overspilled, superelevation heights, and total entrainment. This point may show where secondary overspills, currents generated from splash collapses that travel to the opposite side of the current, are occurring with more frequency. As time progresses (t <30 s) and successive overspills occur momentum components even out in the high curvature simulations (κ^*>0.6) to approximately 0.5-0.4. Despite initially high proportions of along channel momentum, high curvature channels showed the lowest distances traveled and are slowed by encountering large bends. This along channel moment is converted to perpendicular momentum as the flow encounters the wall of the channel which occurs relatively later in the simulation for high curvature channels which travel relatively slower than low curvature channels. Similar proportions of along and perpendicular to channel momentum may also indicate that with in the body of the current, the main momentum bearing region, there is overspill and downstream movement occurring simultaneously.

2.4.2 Thermal Effects due to Channelization. Channelized flows maintain nearly the initial temperature in the underflow for the extent of the simulation (Figure 4). In the overspilled flows outside the channel, the temperatures are more variable because the flows are much thinner than inside the channel, and the avulsion process itself leads to greater engulfment of air and thinner subsequent currents.

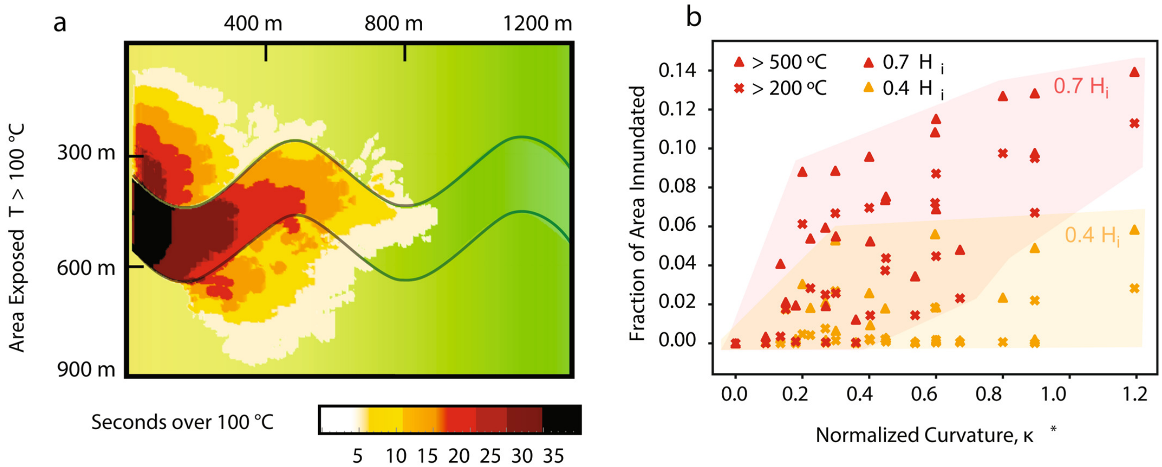

Figure 8. Map of the fraction of area exposed to temperatures over 100 °C as a proxy for this hazard in the example sinuous channel (width: 201 m; depth: 27 m; wavelength: 600 m; amplitude: 90 m) . (a) shows a map view of the channel showing the total time exposed to temperatures of over 100 C across the the domain. Exposure times of over 20 s are common in the channel and close to the channel edges. (b) Show the fraction of total area inundated as a function of normalized curvature for isosurfaces of 500 °C and 200 °C. Triangles indicate exposure to over 200 °C while 'X's indicate exposure to over 500 °C while the two color indicate the high and low volume flux simulations, red and yellow respectively. Outside the channel the area temperature exposure increases with normalized curvature with two clear trends differentiated by volume flux. The higher volume flux simulations show higher areas exposed to dangerous temperatures although total area inundated (Figure 6a) was divorced from volume flux.

The volume bulking, partly due to entrainment, increased as a function of superelevation in all isosurfaces. Superelevation and the resulting collapse initiate entrainment in the stably stratified current. Although the volume increase did correlate with curvature, the correlation is stronger with superelevation, this effect is decoupled from increased volume flux indicating that for these small volume flows the geometry can be a stronger control on the flow and thermal features than volume flux. Straight channelized flows exhibited the least amount of engulfment of air and expansion. The straight channelized flows did not overspill which can initiate voluminous entrainment; they only have one main surface to entrain air at the head of the current and in the wake. The bulk entrainment in the sinuous flows was significantly higher than straight channels and approached and surpasses the entrainment seen in the unconfined flow. More significant overspills were able to entrain significantly more ambient air due to their larger fronts. In addition, the splashes observed in simulations initiate shear due to cross stream flow and produce significant amounts of entrainment and a curtain-like plumes oriented along the edges of the channel. Although entrainment is the major control of temperature, the overspill currents maintained relatively hot currents when the overspill accessed the superelevated, hot underflow.

Due to their high velocity and vapor contact, temperatures over $100°C$ can cause fatal injuries or disfigurement (Baxter, 1990; Baxter et al., 2017). Over the domain, we calculated the time the simulation reached temperatures over 100, 200, $500°C$, then calculated the fraction of the total area that was exposed to these temperatures for over five seconds (Figure 8). The fraction of area outside the channel showed a clear relationship between area exposed and curvature. Additionally, area exposed to dangerous temperatures increases with increased volume flux. Although curvature was the main control on total area inundated in our simulations, the thermal exposure is controlled by both curvature and volume flux.

Pensa et al. (2018) estimated the temperatures of the unconfined ash cloud from the 2015 Volcán de Colima eruptions and found temperatures of $200°C$ which was approximately $170°C$ lower than that of the valley-confined area using charcoal reflectance methods. At Merapi using the 2010 deposits, Wibowo et al. (2018) estimated temperatures of detached PDC of the overbank to be $300 - 440°C$ which is close in temperature to estimates of the channelized flow. The significant cooling due to spreading on an unconfined surface is mirrored in our simulations. However, looking at the maximum temperature experienced outside the channel indicate substantial spatio-temporal thermal heterogeneities which may not be well recorded in the thermal proxies. Some narrow regions close to the overspilling location and sourced from the channelized underflow can also reach temperature near to the initial current temperature ($500°C$) for short periods of time. The temperature observed in these simulations confirms that despite their relatively low densities and dynamic pressures the overspilled currents maintain dangerous conditions for significant flow lengths, hundreds of meters. We also identify a secondary hazard associated with the overspill: the production of increased suspended ash. These plumes although cooler than the main overspill and channelized flow still represent a major hazard by increasing the suspended ash in the air which over minutes of exposure can cause asphyxia (Dellino, Dioguardi, Isaia, Sulpizio, & Mele, 2021).

2.5 Conclusion

The dominant overspill mechanism identified in these simulations is due to the superelevation or wedge formation of the underflow layer as it collides with the walls of the channel. To overwhelm a critical curvature and cause overspill requires high ratios of the channel amplitude to width, in our simulations over 0.25. This produces three distinct types of events of mass exiting the channels including the main overspill of hot material, a buoyant voluminous plume, and dilute secondary overspill across from the initial overspill initiated by cross-stream flow. These features are strongly controlled by the curvature of the sinuous channel. We show here that the overspilled currents generated by confined flows are a major hazard and have high mobility able to flow for hundreds of meters from initiation. These currents can transport hot material out of the channel and present significant dangers to humans. The events of secondary overspills identified here also increase the area inundated by unconfined overspilled flows. In areas where overspills may occur, the opposing banks of channel are also at risk of inundation.

This work also highlights that the overspill occurs due to superelevation of the dense portion of the flow but propagates in the dilute regime. In regards to hazards modeling, it also suggests regime transition and mass exchange is important when implementing overspill in two-layer coupled PDC models. More work is necessary to understand the deposits left by these features, the effect of more complex channel geometries, and the impact of topographic roughness. Multiphase models can provide a look into the internal stratification of the flow and are a vital step into understanding how PDCs interact with topography.

2.6 Bridge

As we conclude our exploration of the generation of overspill pyroclastic density currents in sinuous channels in **Chapter Two**, we have observed how the complex interplay of volcanic materials and topography influences the behavior and mobility of these currents. These insights into the physical characteristics and flow dynamics of pyroclastic density currents offer a fundamental basis for understanding the broader implications of volcanic activity, particularly in terms of thermal energy distribution.

Transitioning into **Chapter Three**, we shift our focus towards the low Reynolds number regime of Darcy flow. Specifically, we delve into the multiphase modeling of hydrothermal systems resulting from dike intrusions. This chapter will examine how the heat transferred from a cooling dike influences the development and behavior of hydrothermal systems using state-of-the-art modeling techniques. We will expand upon the techniques and modeling work developed in this chapter by exploring a new discretization technique in MOOSE. By investigating the thermal evolution of these systems, we aim to provide a clearer understanding of their role in shaping the energy landscape around volcanic dikes. We will explore how these hydrothermal systems impact the permeability and thermal conductivity of the surrounding rocks, and how they contribute to the broader geothermal gradients in volcanic regions. Through this lens, we will uncover the intricate relationships between magmatic intrusions and their hydrothermal aftermath, thereby enhancing our comprehension of the interconnected nature of volcanic and hydrothermal processes.

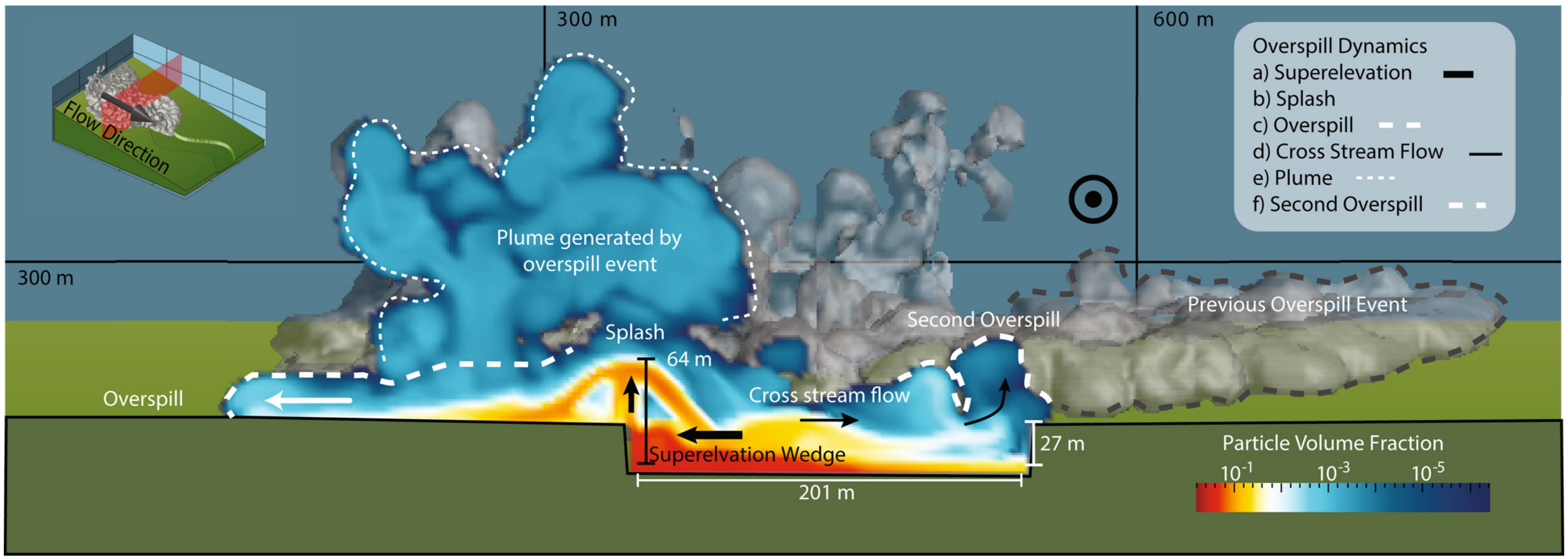

Figure 5. A cut perpendicular to the channel simulation shows the overspill mechanism in sinuous channels by the formation of a wedge shape superelevation as the denser portions of the flow hits against the edge of the channel of depth 27 m and width 201 m. Inset in the top left shows the position of the main figure in red relative to a 10^{-8} isosurface and flow direction.

CHAPTER III

CHAPTER 3: CONDUCTIVE AND ADVECTIVE HEAT TRANSPORT SYSTEMS AROUND SMALL SHALLOW DIKE INTRUSIONS

3.1 Introduction

Dikes play a critical role in transporting magma and volatiles from the deep mantle to the atmosphere, acting as conduits through the Earth's crust. They are ubiquitous in many types of magmatic activity, including fissure eruptions, mid-ocean ridges, and flood basalts. In any magma transport problem, the balance (or imbalance) of heat and mass transport, modulated by the mechanical state of the crust, allows the magma to erupt. Bottom-up forcing from magma reservoirs and the ease of transport due to fracturing are key factors in eruption dynamics. The propensity of the crust to fracture and transport magma is a major control of the mass flux in eruptions. Therefore, the interplay between heat transfer in the crust and the dynamics of magma reservoirs is critical in understanding the tempo and nature of volcanic eruptions in flood basalt regions. Several factors need to align for the magma to reach the surface or shallow crust, allowing the volatiles it contains to affect the atmosphere. The dynamics of mass transport within a single dike and the resulting eruption tempo are crucial for understanding the integrated hazards of an eruption. Most dikes observed with geophysical instrumentation are in the shallow crust, and understanding the interplay of heat transfer from the dike is important for hazard management. Tracing the thermal history of a dike is crucial for understanding its lifetime and can be integrated with field observations, chemistry, and geochronology to provide a comprehensive history of an eruption. Within a single dike, there is a race between the overpressure of the dike (bottom-up forcing) and the solidification of the magma in contact with the cool host rock. Most research has focused on the role of conduction, thermal boundary layers in the magma, and their effects on magma cooling rates. However, modeling and isotope work has shown that large-scale hydrothermal systems (100 meters) around shallow dikes can systematically alter the heat conductivity of the crust. The addition of hydrothermal circulation can speed up heat transfer and effectively increase the thermal footprint of a single eruption.

This work develops a model for hydrothermal circulation around dikes using state-of-the-art finite element methods. Understanding the dynamics of hydrothermal circulation and its impact on magma transport in flood basalt events is crucial for interpreting past volcanic activity and predicting future hazards. Using the Multiphase Object Oriented Simulation Environment (MOOSE), we apply this Department of Energy code, which is well-suited for geologic modeling but has had limited usage in this field. To demonstrate the usage of the code and investigate a simple parameter sweep, we model hydrothermal circulation around a dike at varying permeabilities. This represents the first step, and a technically challenging one, in using MOOSE for the simulation of complex geologic domains. As expected, we show that fluid advection due to porous flow around dikes and changing permeability significantly affects heat transport. Later, we calculate the effective conductivity and show that it changes significantly with both time and space around the intrusion, highlighting the usefulness of 2D models when dealing with fluid advection.

3.2 Methods

3.2.1 Multiphase Object Oriented Simulation Environment (MOOSE). Multiphase effects are ubiquitous through volcanology, from magma solidification to pyroclastic flow. The main challenges of multiphase computational modeling are the numerous scales (for example single crystals in a magma chamber), spatially and temporally changing material properties, and of course phase change. When modeling multiphase systems, it is important to consider the range of scales you can reasonably include and the level of coupling in your equations. Direct numerical simulation where each particle in a pyroclastic flow is impractical and prohibitively expensive in nearly all cases. This is where MOOSE (Multiphysics Object Oriented Simulation Environment) proves to be a valuable tool. MOOSE is designed to handle complex multiphysics problems, offering robust capabilities for simulating coupled processes over a wide range of spatial and temporal scales. Its flexible and modular architecture allows researchers to integrate various physical models and customize simulations to suit specific volcanic processes.

MOOSE is a software framework developed at Idaho National Laboratory, designed primarily for the solution of coupled systems of PDEs (Lindsay et al., 2023; Permann et al., 2020). MOOSE is built on an object-oriented structure that enables the seamless integration of various modules, tools, and solvers, facilitating the efficient solution of highly nonlinear and tightly coupled problems in a parallel computing environment. It utilizes Portable, Extensible Toolkit for Scientific Computation (PETSc) solvers for PDEs and libMesh for parallel adaptive finite element applications (*Balay: PETSc users manual - Google Scholar*, n.d.; Kirk, Peterson, Stogner, & Carey, 2006).

We choose to use this software because of the integration with a variety of multiphysics problems including Darcy's Law above, solid mechanics, heat transfer, and fluid properties. We used the module `PorousFlow` to model the hydrothermal circulation within the host rock around the dike (Wilkins, Green,

& Ennis-King, 2020). MOOSE is well-suited for handling the diverse scales and heterogeneous properties typical of geologic formations. Hydrothermal circulation often occurs in environments with highly variable permeability, porosity, and thermal conductivity, which can span multiple orders of magnitude. MOOSE's adaptive mesh refinement (AMR) capability ensures that computational resources are efficiently allocated, providing high resolution in critical areas while maintaining computational efficiency. This feature is particularly valuable in geologic modeling, where capturing fine details, such as fracture networks or localized heat sources, can significantly impact the accuracy of the simulation. Furthermore, MOOSE's open-source nature and active user community provide extensive support and continuous development, ensuring that users have access to state-of-the-art methods and tools for their geologic simulations.

MOOSE takes advantage of the duplicate nature of many PDEs, boundary conditions, and even post-processing needs and leverages `C++` class inheritance, which minimizes the need to develop new code. For example, one could inherit from the `Diffusion` Kernal in which the residual is $\langle \nabla\phi_i, \nabla u\rangle$ and create a `HeatConduction` kernal in which the residual inherit the same form but adds a heat conduction component $\langle \nabla\phi_i, k\nabla T\rangle$. Kernals can then be combined for various variables for each corresponding term in the PDE where the residual is the sum of each kernals contribution. This allows for easy addition and subtraction of terms in a PDE. Additionally, MOOSE implement `AuxKernals` that can span the spatial and temporal domains but are not incorporated in the residual thus allow for a wide range of post-processing and the loose coupling of variables.

The `MultiApp` system and `StochasticTools` module in MOOSE provide powerful features for advanced geologic modeling and uncertainty quantification. The `MultiApp` system allows users to run multiple, coupled simulations concurrently, allowing simulation of complex interactions between different physical domains or scales. Additionally, the Stochastic Tools module facilitates the incorporation of uncertainties inherent in geologic systems, such as variations in material properties or boundary conditions. By integrating stochastic methods, users can perform probabilistic analyzes, sensitivity studies, and uncertainty quantification, providing a more comprehensive understanding of the range of possible behaviors and risks associated with hydrothermal systems. This capability is essential for making informed decisions in geoscience and engineering applications, where uncertainty often plays a critical role.

3.2.2 Governing Equations.

In this section we will show the equations governing the fluid and heat flow in the system based on the simplifications of the equations in (Wilkins et al., 2020) where the units and symbols are listed in Table 1. First the momentum balance equations for porous media:

$$0 = \frac{\partial}{\partial t}(\Phi \sum_{\beta} S_{\beta}\rho_{\beta}\chi_{\beta\kappa}) + \sum_{\beta} \chi_{\beta\kappa}\nabla \cdot F_{\beta_{advective}} \tag{3.1}$$

where $F_{\beta_{advective}}$ is governed by Darcy's Law:

$$F_{\beta_{advective}} = -\rho_{\beta}\frac{k k_{r,\beta}}{\mu_{\beta}}(\nabla P_{\beta} + \rho_{\beta} g) \tag{3.2}$$

Meanwhile the heat equation is set by

$$0 = \frac{\partial}{\partial t}\left((1-\Phi)\rho_R C_R T + \sum_{\beta} \Phi S_{\beta}\rho_{\beta}E_{\beta} + \kappa\right) + \nabla \cdot \left(-\lambda\nabla T + \sum_{\beta} h_{\beta}F_{\beta_{\text{advective}}}\right) \tag{3.3}$$

Then the following constitutive equations are required for closure; first $\sum_{\beta} S_{\beta} = 1$ and $\sum_{\beta} \chi_{\beta} = 1$. These constitutive equations ensure the conservation of species and the normalization of mass fractions within the mixture.

Parameter	Units	Description
t	s	time
β	Dimensionless	Phase indicator
Φ	Dimensionless	Porosity
S_β	Dimensionless	Saturation of phase β
ρ_β	kg/m^3	Density of phase β
χ_β	Dimensionless	Mass fraction of phase β
$F_{\beta_{\mathrm{advective}}}$	m^3/s	Advective flux of phase β
k	m^2	Permeability of the porous medium
$k_{r,\beta}$	Dimensionless	Relative permeability of phase β
μ_β	Pa·s	Dynamic viscosity of phase β
P_β	Pa	Pressure in phase β
g	m/s^2	Acceleration due to gravity
ρ_R	kg/m^3	Rock density
C_R	J/(kg·K)	Specific heat capacity of rock
α	m^2/s	permeability
T	K	Temperature
E_β	J/kg	Internal energy of phase β
κ	W/m·K	Heat conduction term
λ	W/(m·K)	Thermal conductivity
h_β	J/kg	Specific enthalpy of fluid phase β

Table 1. Parameters of the fluid and heat flow equations in Porous Flow MOOSE Module.

3.2.3 Finite Element Method. After formulation of our equations, we need a method to project these continuous equations onto a discrete computational domain. One of a variety of discretization techniques for partial differential equations (PDEs), the Finite Element Method (FEM) obtains an approximate solution to the equations by converting the problem into a system of equations. The discretization process involves subdividing the computational domain into smaller elements interconnected at discrete points called nodes. Each element is associated with a set of basis functions that approximate the solution over that element. Thus, the FEM forms a set of approximate solutions from boundary condition to boundary condition across nodes which differs from Finite

Volume in Chapter 2 in that it focuses on continuous solutions over elements rather than cell averages over control volumes. In the FEM, first the weak form of the equation is found where the weak form allows solutions that may not possess derivatives everywhere in the domain but still satisfy the integral form of the equation. We will provide an example of this using a simple diffusion equation. Suppose that we have a PDE of a variable u^* which is governed by this equation:

$$\nabla^2 u^* = f \tag{3.4}$$

which is accompanied by some boundary conditions across a spatial domain Ω. The exact solution may be difficult to solve for especially if the domain is complex; in real life of course u^* is real and differentiable however our guess function u may not be. We can try to approximate a solution with which will not be exact and we will "test" it against an arbitrary smooth function ϕ to obtain this equation

$$\phi f = \phi \nabla^2 u \tag{3.5}$$

To produce the weak form first we integrate over the boundary Ω:

$$\int_\Omega \phi(\nabla \cdot \nabla u) = \phi f \tag{3.6}$$

where we've rewritten the Laplacian operator ∇^2 as $\nabla \cdot \nabla$. Using the product rule we rewrite it as follows:

$$\int_\Omega \nabla\phi \cdot \nabla u - \int_\Omega \nabla \cdot (\phi \nabla u) = \phi f \tag{3.7}$$

then using the divergence theorem

$$\int_\Omega \nabla\phi \cdot \nabla u - \int_\Gamma \phi \nabla u \cdot \hat{n} = (\nabla\phi, \nabla u) - \langle \phi, \nabla u \cdot \hat{n} \rangle = \phi f \tag{3.8}$$

where $\Gamma = \partial\Omega$ is the surface of the domain Ω. This can then be expressed as inner project notation where the $(\nabla\phi, \nabla u)$ is a `Kernal` object in MOOSE and $\langle \phi, \nabla u \cdot$

$\hat{n}\rangle$ is a `BC` object. The residual, which is the misfit from the approximation to the true solution, is calculated as:

$$R = \phi(\nabla^2 u - f). \tag{3.9}$$

In this method, using Newton iterations, we seek to minimize R to a specified small value. Notably, the residual is not $u^* - u$ because u^* is unknown. We can also rewrite R as follows.

$$\int_{\Omega}(f - \nabla^2 u)\phi_i d\Omega = R \tag{3.10}$$

which enforces the fact that the test functions ϕ_i are orthogonal to the vector of the residual R. This is also known as the Galerkin method. The basis functions ψ_i and test functions ϕ_i are known integrable functions, where $\mathbf{U}$ is a vector of coefficients at nodes. In the Galerkin method, which is used in MOOSE, the test functions ϕ_i are chosen to be the same as the basis functions ψ_i.

The Galerkin method is an effective choice because its effectiveness is independent of the problem formulation. This allows it to be applied to a variety of PDEs that are coupled together in a single framework. The simplicity and elegance of this method is based on the coincident choice of both the test function and the basis function. We can rewrite the equation for the residual as follows.

This is how we handle the PDEs but to finish the discretization we need a set of discrete or finite elements, which we will iterate over to solve for an approximation of u. This process is visually demonstrated in Figure 9. A finite domain is broken up into pieces called elements of various types (rectangular, triangular, etc.), and the points where element corners touch are called nodes. The solution u is only defined on the nodes in this method as opposed to in the faces in an FV method. The vector of coefficients U is "projected" into the basis functions ψ so that

$$u = \sum_i U_i \psi_i \tag{3.11}$$

where the basis functions typically are 1 at the node and 0 elsewhere. Combined with the application of the test function ϕ, this transforms the problem into a finite dimensional approximation where as N, the number of elements, becomes large the approximate solution converges to u^*. When we substitute Equation 3.11 into 3.8 we can transform it into a set of matrix operations using the following:

$$\int_\Omega \nabla \left(\sum_{i=1}^{N} U_i \psi_i \right) \cdot \nabla \phi \, d\Omega = \phi f \tag{3.12}$$

We then distribute the gradient and the summation:

$$\int_\Omega \sum_{i=1}^{N} U_i \nabla \psi_i \cdot \nabla \phi \, d\Omega = \phi f \tag{3.13}$$

Since integration and summation are linear operations, we can interchange the sum and the integral:

$$\sum_{i=1}^{N} U_i \int_\Omega \nabla \psi_i \cdot \nabla \phi \, d\Omega = \phi f \tag{3.14}$$

In the Galerkin method, the test functions ϕ are chosen to be the same as the basis functions ψ_j. That is, $\phi = \psi_j$ for $j = 1, 2, \ldots, N$.

Substituting $\phi = \psi_j$ into the weak form gives yields a system of linear equations:

$$\sum_{i=1}^{N} U_i \int_\Omega \nabla \phi_i \cdot \nabla \phi_j \, d\Omega = \phi f \quad \forall j = 1, 2, \ldots, N \tag{3.15}$$

Define the stiffness matrix K and the load vector F as:

$$K_{ij} = \int_\Omega \nabla \phi_i \cdot \nabla \phi_j \, d\Omega \tag{3.16}$$

$$F_j = \int_\Omega \phi_i f \, d\Omega \tag{3.17}$$

Thus, the system of equations becomes:

$$\sum_{i=1}^{N} K_{ij} U_i = F_j \quad \forall j = 1, 2, \ldots, N \tag{3.18}$$

In matrix form, this is:

$$\mathbf{KU} = \mathbf{F} \tag{3.19}$$

This results in a system of linear equations involving the stiffness matrix $\mathbf{K}$ and the load vector $\mathbf{F}$, which can be solved for a vector of points U_i of size N, approximating the solution u over the domain Ω. The stiffness matrix is of size NxN. The names "stiffness matrix" and "load vector" come from the use of FEM in solid mechanics, especially in engineering applications, but can easily be substituted with the idea of a material properties matrix and source term vector.

Again, this work occurs not in the continuous space of our physical life, but in the discrete memory of a computer. Integration in Equation 3.15 requires Numerical Integration also refered to as Gaussian integration or Gaussian Quadature although sometimes other formulations are implemented. It uses specific points (called quadature points) and corresponding weights to evaluate the function and sum these evaluations to approximate the integral. Correspondingly in MOOSE, every kernal object includes the `computeQpJacobian()` function which computes the value of the weak form at every quadature point. This method is integral to achieving high accuracy in simulations, particularly when dealing with nonlinear materials or complex geometrical domains, as it efficiently handles the polynomial approximations typical of FEM formulations.

Finally, in Figure 9 we see a variety of irregularly shaped and sized elements. Some are triangular, and others are rectangular. This is a strength of FEM.

There are a variety of element types available in MOOSE via integration with `libMesh` such as quadratic or triangular (Kirk et al., 2006). The type of element can be set using the `MeshGenerator` system in MOOSE. For each element type, one can select an order of shape function that governs the interpolation of values between nodes, which can be set when the variables are defined using `ORDER=LAGRANGE` . When solving Equation 3.15 for each element N it is useful to use a local coordinate system with evenly sized and shaped elements, this is shown in the bottom right of Figure 9 where the local coordinates (s, r) can be written as the linear transformation of global coordinates using the Jacobian Matrix. This is shown simply in Figure 9, but in practice it requires the partial derivatives of the kernal objects which themselves depend on the properties of the material, spatial derivatives and temporal derivatives. Taking these derivatives by hand is challenging, time-consuming, and prone to error. Exclusion of a material property or kernal object may lead to incorrect or incomplete Jacobian formulation, which will either result in the wrong result or the problem will not be able to be solved. Any issues in the formation of the numerical integration will also significantly affect the formulation of the Jacobian, leading to a cascade of errors.

Finally, this system is solved iteratively using Newton's method for root finding. We can start with the residual vector for U_i the vector of the solution written as $R(U)$ with our initial approximation of the solution U_0 also known as initial conditions. Using a Taylor expansion:

$$R(U) = R(U^0) + (u^* - U^0)\frac{\partial R}{\partial U} \tag{3.20}$$

where U^0 is the initial estimate (initial conditions at the start of the algorithm before any updates). Since $R(u^*) = 0$,

$$\frac{\partial R}{\partial U}(u^* - U^0) = -R(U^0) \tag{3.21}$$

which shows the importance of correctly evaluating $\frac{\partial R}{\partial U}$ since it determine the next step of the algorithm and again depends on the correctness of the Jacobian and integration at quadature points.

Key settings that influence the performance and convergence of Newton's method in MOOSE is the "nonlinear absolute tolerance". This parameter is critical because it defines the absolute convergence criterion for the nonlinear solver, indicating how close the solution needs to be to the actual root, based solely on the residual norms, before the iterative process can terminate. Setting this tolerance appropriately is crucial: if it is too tight, the solver may perform unnecessary iterations, increasing computational cost; if too loose, the solution may not be accurate enough, potentially leading to erroneous simulation results. This balance is vital for the efficient and effective application of Newton's method in the diverse and challenging simulations handled by MOOSE.

3.2.4 Model Setup. The hydrothermal circulation model was developed using the Multiphysics Object Oriented Simulation Environment (MOOSE). The domain consists of a half-space of host rock with a dike instantaneously intruded on one boundary, and the model simulates thermal and fluid flow processes within this system.

3.2.4.1 Domain and Mesh Generation. The computational domain is a two-dimensional rectangle with a width (W) of 2000 meters and a length (L) of 1000 meters. The depth at the top of the domain is set at 1500 meters. The mesh is generated using 50 elements along both the x and the y

Table 2. Material Properties for each domain in MOOSE simulation. Density, heat capacity, thermal conductivity, length, width, and rock porosity all have units as described in Table 1

Subdomain Label	ρ	c_p	k	L	W	ϕ
host	2400	790	3	2000	1000	0.1
dike	3000	1100	3	50	750	0.1

directions, and a bias factor of 1.2 is applied in the horizontal domain to ensure a finer resolution near the central region with. The domain is subdivided into two subdomains: the host rock and the dike, with the dike occupying a central rectangular region of width W and length L. An interface is created between these subdomains to facilitate the coupling of physical processes. Each subdomain has specific material properties of density, thermal conductivity, and heat capacity as references in Table 2. The interface between the two domains is generated using `SideSetsBetweenSubdomainsGenerator` and labeled "interface". This is an important step to maintain continuity between domains so that nodes on either side match up correctly and all fields are conserved across domains.

3.2.4.2 Initial Conditions and Boundary Conditions.

The model incorporates gravitational effects, with gravity defined as $\vec{g} = (0, -9.81, 0)\,\mathrm{m/s^2}$. The hydrostatic pressure distribution is initialized using a function that accounts for the atmospheric pressure and the weight of the overlying water column including the 1500 m depth which is set to be the top of the simulation at Y = 1000 m. The initial temperature distribution in the host rock is defined by a geothermal gradient of 10 K/km, while the temperature within the dike is set to a constant value of 1438 K, the liquidus temperature of an andesitic basalt.

Boundary conditions are applied to simulate realistic geological settings. The temperature is fixed along the right Dirichlet boundary condition matching the initial geothermal gradient, which enforces the fact that this boundary is the far field temperature where there should be little effects of the dike instrusion. Neumann boundary conditions with zero flux are applied to the porepressure at the right, left, and bottom, ensuring no external fluid flow into or out of the domain. However, there is flow allowed in and out of the top of the model.

3.2.4.3 Materials and Kernels. The properties of the material are defined to simulate the thermal and hydraulic behavior of the porous media. The permeability is treated as isotropic and constant throughout the domain. Thermal conductivity, porosity, and other relevant properties are specified for both the host rock and the dike. The heat conduction, advective heat transport, and mass conservation equations are implemented using appropriate MOOSE kernels. These kernels ensure that the energy and mass balances are accurately represented in the numerical model. The kernals used are `PorousFlowHeatConduction` , `PorousFlowEnergyTimeDerivative` , `PorousFlowFullySaturatedAdvectiveFlux` , `PorousFlowMassTimeDerivative` , and `PorousFlowFullySaturatedUpwindHeatAdvection` . There are a variety of kernals available in the `PorousFlow` but these were chosen first because the simulation is fully saturated with water at all times and spaces ($S_{water} = 1$ everywhere). In a multiphase simulation where there are more than one phase, the unsaturated versions of the kernals are necessary. Upwinding within `PorousFlow` specifically deals with advective transport of heat or mass and increases the numerical stability of the simulation leading to better convergence for the price of introducing numerical diffusion and a slight increase in computational cost compared to the default version `PorousFlowHeatAdvection` . In simple terms, upwinding refers to the idea of considering the upstream values in a flow field when computing the value at a certain point. The upstream direction is determined by the direction of the flow. In full upwinding, the value at a point is computed entirely based on the upstream values. This is in contrast to other methods like central differencing or partial upwinding, where both upstream and downstream values (or a combination of them) are used. In the case of `PorousFlow` , this specifically deals with where the residual integral calculates the moblity $m = \frac{\rho k_r}{\mu}$ as part of the Darcy flow (Equation 3.2). This does introduce numerical diffusion, which occurs when sharp boundaries in pressure, temperature, or other tracers, for example, become more diffuse over time as they are advected. This can be combated via other stabliziation techniques, such as Kuzmin-Turek. However, in this case, the presence of numerical diffusion is considered acceptable since front tracking is not necessary in this problem.

3.2.4.4 Preconditioning and Solver Settings. To solve the coupled nonlinear equations efficiently, the model uses the MUMPS (MUltifrontal Massively Parallel Sparse) preconditioner with a direct solver strategy. Darcy flow problems typically result in large, sparse linear systems due to the discretization of the governing partial differential equations. MUMPS is designed specifically to handle sparse matrices efficiently by factorizing them into a series of smaller dense matrices which can also be handled in parallel, making it well-suited for these types of problem. In a simple simulation, Darcy flow depends on the nodes around it, however, this yields values only in the diagonals and off-diagonals off a matrix, which might be very large depending on the size of the problem which can lead to instability. Adding in material differences in the simulation, for example anisotropic permeability leads to a sparse matrix with a complex pattern of nonzero entries and preconditioning is necessary for the iterative solve. The transient simulation runs for a total of 3×10^9 seconds (approximately 95 years) with an initial time step of 2×10^6 seconds. The Newton method is employed to solve the nonlinear system, with automatic scaling and adaptive time-stepping to ensure convergence.

3.2.5 Simulations Performed. We performed one simulation with the same initial conditions but only utilizing heat conduction

$$\rho c_p \frac{\partial T}{\partial t} - \nabla^2 (kT) = q \tag{3.22}$$

Material properties in this simulation are different for the dike and host as in Table 2. This model can be taken to be the "control" to test the role of advective fluid dynamics in the heat transfer around the dike. Using the module `StochasticTools` , a parameter sweep was performed that tested six values of permeability: 10^{-11} to 10^{-15} meters squared. The low value of permeability may represent an extremely porous sandstone, while the high value of permeability result should start to converge with the control simulation.

3.3 Results and Discussion

The results reveal that higher permeability values ($log(k) = -11.0$ and -12.0) lead to a rapid increase in the initial temperature, which peaks early before gradually decreasing (Figure 11).

This behavior can be attributed to the enhanced fluid flow and heat transfer, which quickly dissipates the initial thermal energy from the dike. In high permeability cases, a plume forms from the dike intrusion and rises to the top of the simulation. In contrast, lower permeability values ($log(k) = -14.0$ and -15.0) demonstrate a more gradual temperature rise, with the maximum temperature stabilizing over time. This is indicative of restricted fluid flow, resulting in slower heat transfer and a prolonged temperature increase. The low permeability results converge to the temperatures predicted by the conduction-only example.

In the low permeability simulations, the average and maximum hostrock temperatures reach a maximum value soon after dike emplacement and then decrease showing a short lived (2-20 years) pulse of heat. In the medium permeability (10^{-13}m^2) example, the pulse of maximum temperatures is significantly smoother, and high temperatures (more than 800 K) persist for $\sim$ 85 years. In simulations where conduction dominates, the maximum temperatures in the host rock increase over time to a maximum of approximately $750K$.

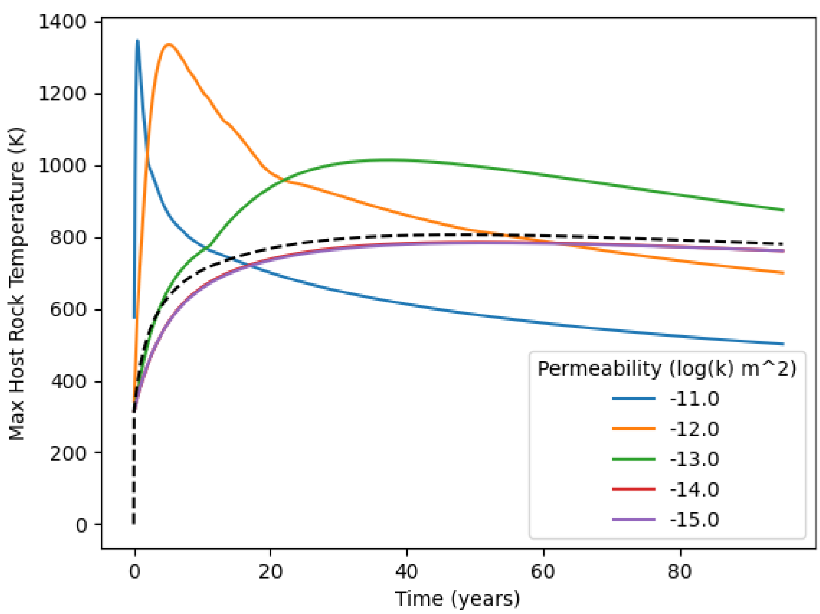

Figure 11. Variation of the maximum host rock temperature over time for different permeabilities, indicated by the logarithm of permeability (log(k) in m^2). The graph shows the temperature evolution for five different permeability values, ranging from -11.0 to -15.0. The temperature peaks early and then stabilizes over time, with higher permeability leading to higher initial temperatures and faster stabilization.

Heat flow coming out of the dike shown in Figure 12 shows a pulse of heat associated with the dike. The length of time and peak of the pulse of heat is strongly controlled by permeability with highly permeable simulations showing quick, short, bursts of heat while the conduction only simulation shows a long heating trend over time.

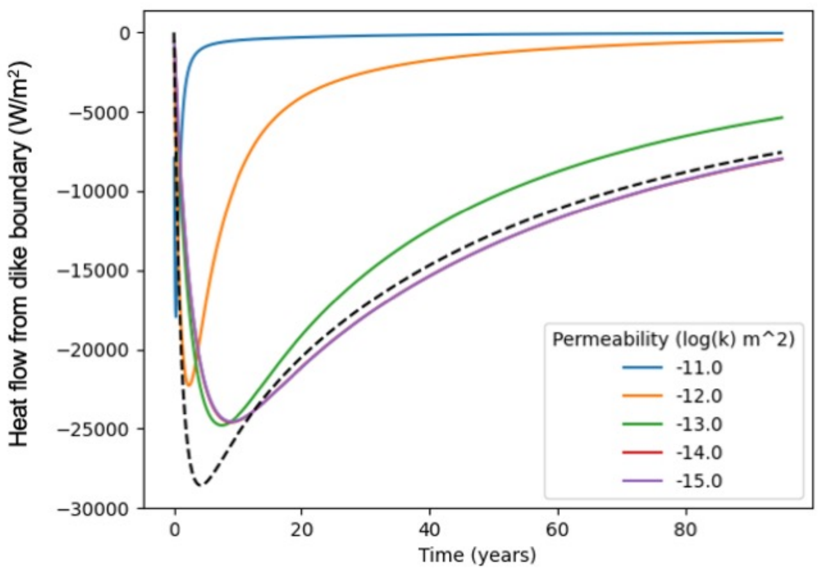

Figure 12. Heat flow from the dike over time for different permeability values (log(k) in m^2). Higher permeability values show a rapid initial heat flow decrease followed by a gradual increase, while lower permeability values exhibit a more consistent and prolonged heat flow. The dashed line represents the reference scenario.

3.3.1 Role of Advection. To compare the conductive and advective components of the heat transport we introduce two timescales firstly

$$\tau_c = \frac{L_c^2}{\alpha} \tag{3.23}$$

the timescale for conduction which is a function the lengthscale L_c and the thermal diffusivity. Secondly, in the case of advection with velocity magnitude u we have the timescale

$$\tau_{ad} = L_{ad}u \tag{3.24}$$

We can combine these into a Peclet number, the ratio of advective versus conductive transport. If we set the length scales equal to eachother $L_c = L_{ad}$ (equivalent to saying the time it takes for heat to travel L distance in conduction and advection respectively) it can be expressed as :

$$Pe = \frac{\tau_{ad}}{\tau_c} = \frac{\rho c_p L u}{k} \tag{3.25}$$

where we take L to be the characteristic length scale in the simulation of $1000m$. Examining the Peclet number in two simulations of 10^{-13} and 10^{-15} you can see that in the lower permeability case advection dominates over conduction with high Peclet numbers in the region of the dike ($Pe \sim 100 - 1000$). This is depite the fact that both simulations develop hydrothermal circulation cells as seen by the vector of darcy velocity.

This indicates that the Rayleigh number which is a function of temperature gradient and permeability is high enough in both simulations for circulation to occur but the permeability controls the velocity magnitude. In the $k = 10^{-13}$ simulation, the convection cell appears to span the 2000 km domain but show the most vigor in the first 600 m. In the 10^{-15} simulation the convection cell is signficiantly shorter only 700 m and 600 m wide. None the less these simulations show that a relatively small dike can affect 100s of meters around it. In both simulations the hightest values of the Peclet number are found inside the dike. But close inspection shows a lower value on the border of the dike and host rock in both examples. This is due to the fact that at this point the advection cell velocities cancel out partially leaving low velocities. Simulations show that water is sucked in from the bottom of the dike and up into the convection cell leading to non-uniform cooling at the base of the dike consistent with estimates of cooling as function of depth by Cheng et al. (1980). Essentially heat is sucked out from the dike and into a plume in the highly adjective simulations.

Continuing our scaling analysis the heat flow from the dike intrusion can be estimated as

$$Q = \rho c_p (T_{dike} - T_{host}) W \tag{3.26}$$

where Q is the heat energy per area and W is the width of the dike. For simplicity, this neglects latent heat of fusion would significantly change the results. We can normalize the temperature using the following equation:

$$T^* = \frac{T}{Q/\rho c_p \sqrt{\alpha t}} \tag{3.27}$$

where $\sqrt{\alpha t}$ is the length scale of diffusion rewritten from Equation 3.23. Finally we can plot the normalized temperature by the square root of time to see how the advective simulations diverge. The maximum temperature in the host rock shows three separate trends in Figure 14. First, in the two lowest permeability simulations, they follow the trend of conduction as expected. In the two highest permeability simulations, at the end of the simulated time they show lower temperatures than the conduction only indicating that they have effectively transported heat out of the simulation. Then in the $k = 10^{-13}$ simulation it shows a higher temperature than the reference simulation which indicates that it takes longer for strong advection to develop and move heat in the simulation to to the rest of the domain. Considering maximum dike temperature in Figure 15 all but two simulations follow the reference where as the most strongly advective simulations show significantly lower temperatures due to the effective removal of heat.

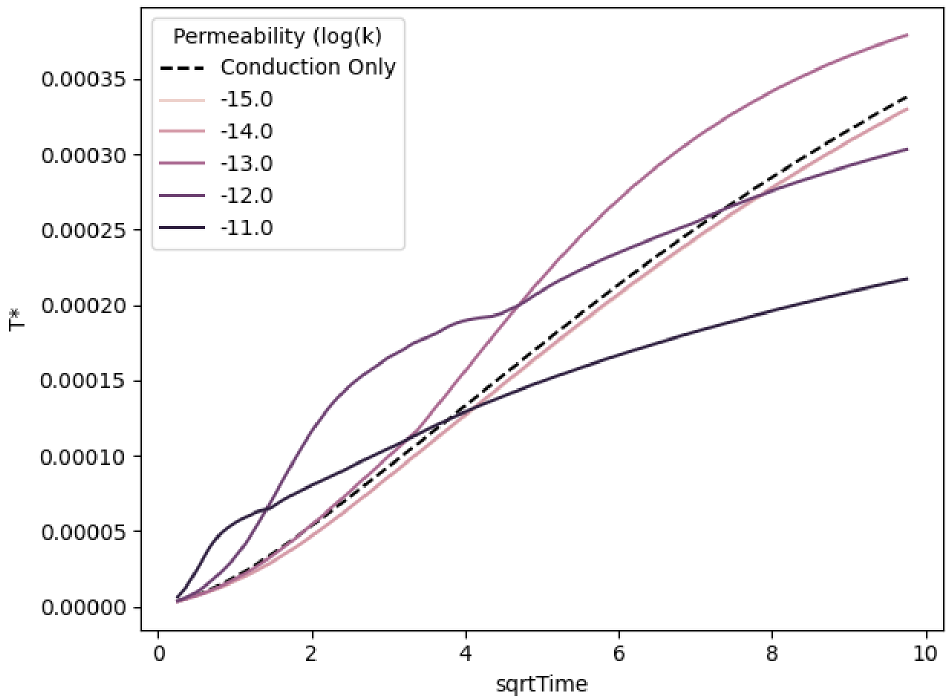

Figure 14. Temporal progression of the maximum host rock temperature, T^*, as a function of the square root of time for different permeability levels, indicated by $log(k)$. This plot illustrates five permeability scenarios from $log(k) = -15.0$ to -11.0. The dashd line represents a conduction-only scenario, contrasting with the colored solid lines that exhibit varying rates of temperature increase influenced by different permeabilities. This graph demonstrates how higher permeability values slow down the temperature rise, reflecting more effective thermal diffusion across the material.

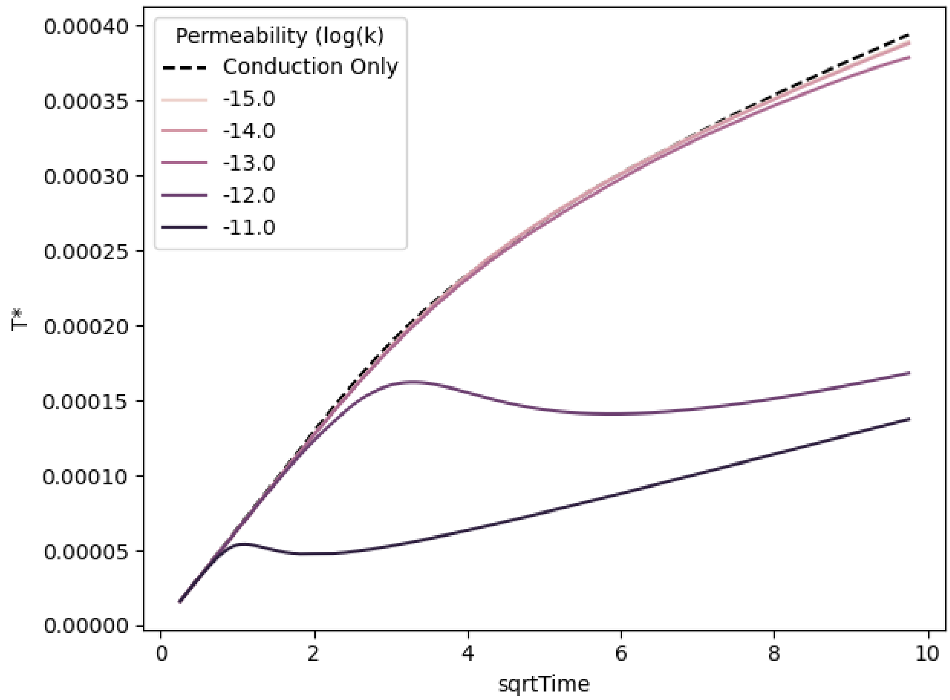

Figure 15. Evolution of the maximum dike temperature T^* as a function of the square root of time, shown for different values of permeability ($\log(k)$). The plot tracks changes across several logarithmic scales of permeability from 10^{-15} to 10^{-11} meters squared, with each line representing a different scenario. The dashed line denotes the behavior in a conduction-only model, serving as a reference.

In the case of simple unsteady conduction, one can derive an analytical equation for the temperature as a function of time and distance from the dike x (Turcotte & Schubert, 2002). Holding the far field temperature $x \to \infty$ to T_0 we can write the heat balance as :

$$Q = 2\rho c_p \int_0^\infty (T - T_0) dx \tag{3.28}$$

for all t. We can construct a similarity variable $\eta = x/2\sqrt{\alpha t}$ which utilizes the time scale of Equation 3.23. Combining this with the non dimensional temperature T^* in Equation 3.27 we can write Equation 3.28 as:

$$\int_0^\infty T^* d\eta = \frac{1}{2} \tag{3.29}$$

which can be used with Equation 3.22 to write the equation in terms of the similarity variable.

$$-2\frac{d}{d\eta}(\eta T^*) = \frac{d^2T^*}{d\eta^2} \tag{3.30}$$

which can be integrated combined with symmetry conditions and initial conditions to give a temperature distribution of

$$T(x,t) = T_0 + \frac{Q}{2\rho c_p\sqrt{\pi\alpha t}}e^{-x^2/4\alpha t} \tag{3.31}$$

where T_0 is the temperature at $t = 0$. Given this equation for temperature as a function of x, t we can use this to fit profiles of temperature from our models to back calculate the effective conductivity where ρ and c_p are kept to the values in Table 2. For each time t, the values of $T(x)$ from a profile along the horizontal axis from the edge of the dike to 300 m distance are used to fit Equation 3.31 using `scipy` . This gives a rough estimate for the value of conductivity if the solution was purely conductive. Results show that due to advection, conductivity varies greatly over time up to 20X the prescribed value (Figure 16).

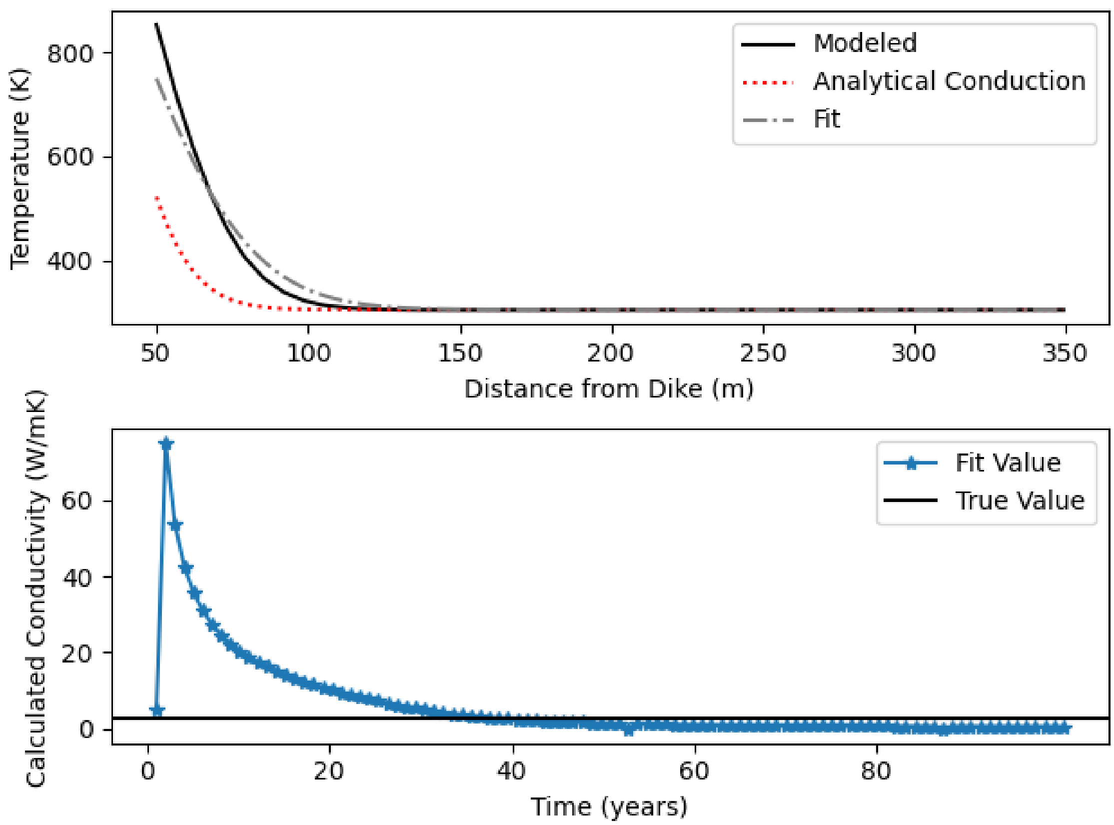

Figure 16. (Top) Temperature distribution as a function of distance from the dike. The black solid line represents the modeled temperature profile, the red dotted line shows the analytical conduction solution, and the gray dashed-dot line indicates the fit of the analytical solution. (Bottom) Calculated thermal conductivity over time. The blue line represent the fit values, and the black solid line represents the true value. The initial spike and subsequent decline in the fit value illustrate the adjustment period before stabilization around the true value.

This analysis can be used in the future in reduced order models such as Karlstrom et al., 2019 to account for the effect of advective transport which is shown to be significant over the first decades of dike cooling. It also highlights some of the difficulty in parameterizing the hydrothermal system which is spatially and temporally variable.

3.4 Summary

In this chapter, we introduce MOOSE and detail the usage of the finite element method (FEM), relating it to specific functions within MOOSE. FEM focuses on discretization with test functions using an approximation of the true solution and integrating these shape functions across a complex physical domain. This is a particularly useful method for geologic modeling because it allows for spatially variable material properties. We then show how we've applied this model to dikes using different subdomains to account for the dike and host rocks, and a specific stabilization technique for solving it. Following the methods, we apply this to varying permeability to emphasize the effect of fluid advection on heat transport, similar to other work such as Abbey, Randolph-Flagg, Villa, Kim, and Shuster (2024); Bindeman et al. (2020); Ingebritsen and Hayba (1994). We will now focus on future work enabled by this advanced modeling technique, which will add to our understanding of heat transport in dikes with multiphase flow.

3.5 Future Work

3.5.1 Multiphase Simulation Benchmark. Current simulations do not include the physics of boiling phase change and steam advection; however, these are an important dynamic to include. The formation of a boiling zone introduces an isothermal boundary layer around the dike in which steam rises relatively quickly, efficiently removing heat from the boundary of the dike, but also introduces significant changes in spatial heat transfer (Abbey et al., 2024; Cheng & Verma, 1980). MOOSE includes the ability to model phase change using the persistent variable approach similar to HYDROTHERM (Ingebritsen, Geiger, Hurwitz, & Driesner, 2010). This method relies on pressure and enthalpy as the main variables to increase numerical stability in two cases, first when one phase completely disappears (ie, no steam) and second in the two-phase region $\frac{\partial T}{\partial p} = 0$. We aim to compare results such as temperature profiles, phase saturations, and the spatial shapes of plume or aureole to HYDROTHERM as a benchmarking exercise for MOOSE. HYDROTHERM is a long-established and thoroughly benchmarked code for hydrothermal circulation, but lacks advanced capabilities in the MOOSE framework, such as adaptive mesh refinement, more complex mesh shapes, and coupling with other PDEs. MOOSE has been thoroughly benchmarked before for other parts of the framework, and this study will add another level of robustness specifically to the two-phase regimes (Green, Jackson, Gunning, Wilkins, & Ennis-King, 2024).

3.5.2 Coupled Magma Flow. After the addition of boiling, we will proceed to run a tightly coupled model of hydrothermal circulation and Navier-Stokes fluid flow within the dike. The aim of this model is to test how coupled flows interact via thermal boundary layer development and the effect of spatial heterogeneity. Currently, the dike is "emplaced" instantaneously and cools via both advection and conduction; water is able to circulate within the dike immediately. This is an inaccurate portrayal of the dynamics made for simplicity and because currently the timestep of the porous flow model is large compared to the dike lifetime. In a higher-fidelity simulation, we would first model flow within the dike and the heat transfer owing to latent heat of fusion. Previous work has established that modeling heat advection in the dike has important results on the total heat flow in the host rock (Petcovic & Dufek, 2005b). And as seen in this work the heat flow around the dike is significantly different in the porous flow regime compared to pure conduction. These two results will be combined to investigate the coupled problem shown in Figure 17. This leverages MOOSE's

MultiApp system. One could probably run all the physics for this problem in one application, but due to the small timesteps necessary for the Navier-Stokes equation compared to the Darcy flow equations. This framework allows one to spin up numerous “subapps” or “child apps” from a main MOOSE solve instance. In this case the main application is set to be the physics problem with the largest spatial and temporal domain, the host rock in which we solve Darcy’s equation as noted above. MOOSE offers various types of coupling. First, fully coupled would represent a system where all variables and their respective equations are included in a single Jacobian matrix and residual vector. The nonlinear solver operates on the entire system, considering the interdependencies between the different physics. However, tightly coupled separates physics and solvers then iterates among them using Picard iterations (Gaston et al., 2015; Permann et al., 2020). Typically, this involves setting when iteractions will take place amongst main and subapp timesteps. For example, heat flux may be calculated in the main app, transferred to the sub-app where temperature is calculated, then temperature is transferred in the main app and the process repeats until convergence criteria are met. An additional step is necessary than that shown in Figure 17 which is normalization of the transferred heat. Due to the transfer between simulation of different meshes, which involves interpolation between nodes, energy is not conserved. To combat this, the integral of the energy flux at the boundary is calculated in `hostApp` and this quantitity is used to normalize and the values are sent to `dikeApp` .

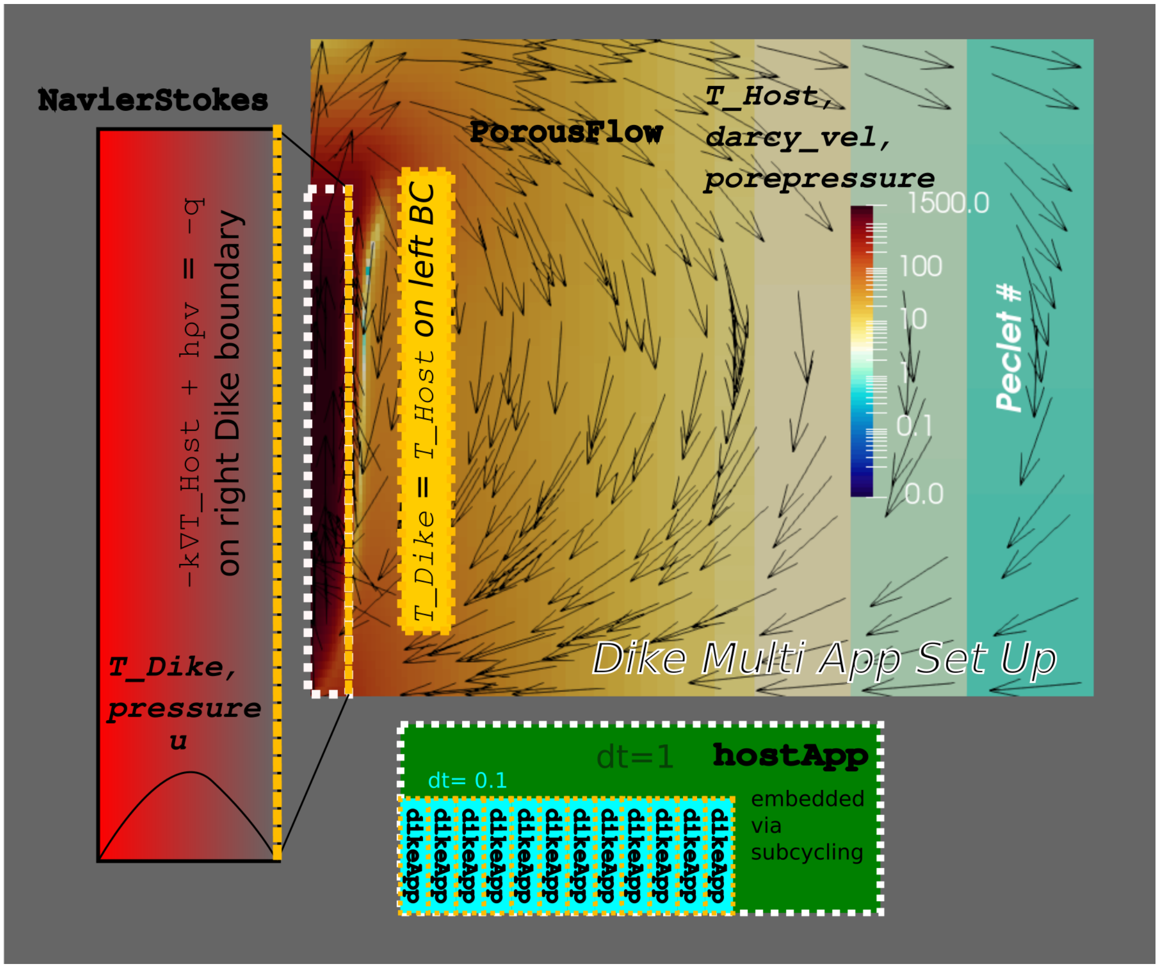

Figure 17. Schematic representation of the Dike MultiApp setup. The figure illustrates the coupling between the NavierStokes and PorousFlow modules. The left section represents the Navier-Stokes module, where the heat flux boundary condition is applied on the right Dike boundary. The central section shows the PorousFlow module with the darcy velocity vectors displayed and the Peclet number distribution is displayed, highlighting the flow dynamics. The bottom section depicts the subcycling approach, where the dikeApp operates with a smaller timestep (dt = 0.1) compared to the hostApp (dt = 1), enabling efficient and stable multi-scale simulations.

3.6 Bridge

In Chapter 3, we extensively examined the multiphase modeling of hydrothermal systems around dikes, emphasizing how heat and fluid transfer processes influence the geochemical and geophysical environment. This exploration not only shed light on the dynamic interactions within these systems, but also highlighted the importance of understanding the structural features that facilitate such interactions.

As we move into Chapter 4, our focus pivots from the dynamic processes to the structural complexities of dikes in a map view. We will explore multiscale spatial patterns in giant dike swarms, identified through objective feature extraction techniques. This chapter builds on the foundational knowledge of dike-induced hydrothermal systems by analyzing how the physical structure of dike swarms themselves can influence geological and geochemical processes. Using feature extraction methods, we investigate the spatial organization and distribution of these dike swarms, aiming to unravel the underlying patterns that govern their formation and propagation.

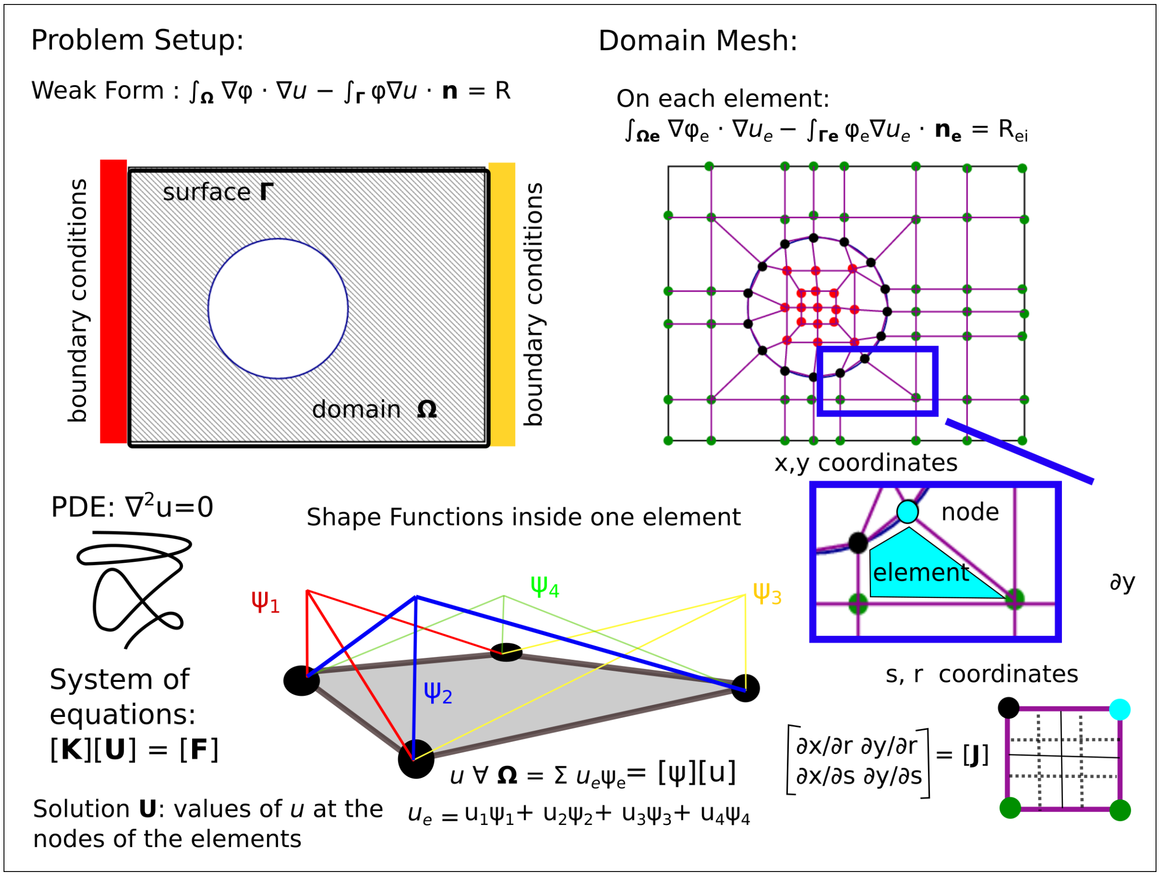

Figure 9. Illustration of the Finite Element Method (FEM) discretization process for solving the Poisson equation $\nabla^2 u = 0$. The figure demonstrates the problem setup, including the weak form of the PDE and the application of boundary conditions on the domain Ω with boundary Γ. The domain is discretized into a mesh of elements, where each element contributes to the overall solution. The local formulation of the weak form on each element Ω_e is shown, with contributions to the global system of equations $\mathbf{K}[\mathbf{U}] = [\mathbf{F}]$. The shape functions ($\psi_i$) inside one element are used to interpolate the solution u at the nodes, resulting in the approximate solution $u_h = \sum_i u_i \psi_i$ across the entire domain. The bottom right shows the transformation from an isoparametric element to the (x,y) domain and the formation of the Jacobian Matrix.

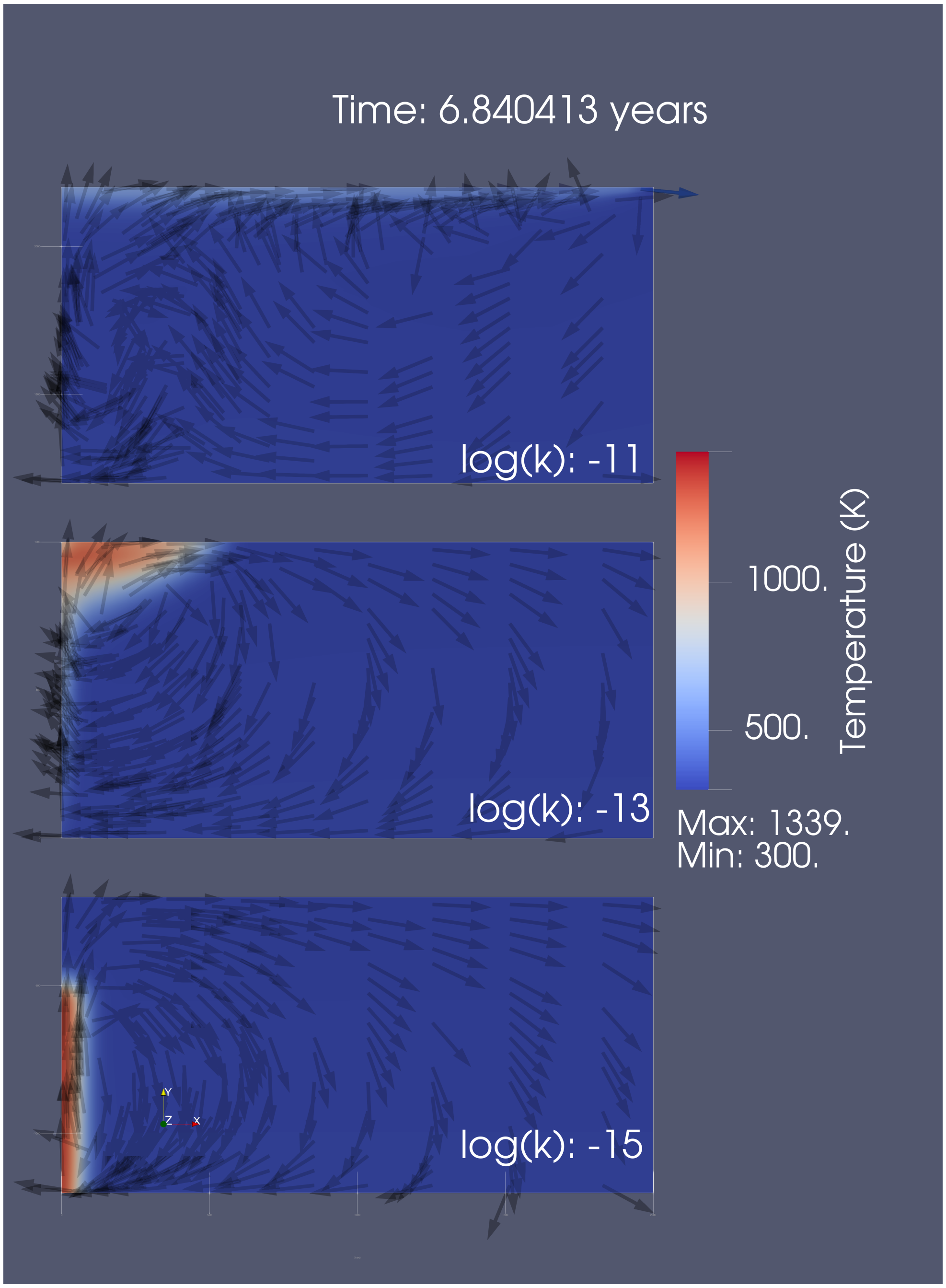

Figure 10. Visualization of temperature distribution and vector flow fields over a domain, captured at $t = 6.840413$ years. Three subplots represent different scenarios with varying permeability: 10^{-11}, 10^{-13}, and 10^{-15}. Each plot illustrates the spatial variation in temperature (color scale from 300 K to 1400 K) and directionality of heat flow (vector fields). The influence of decreasing permeability on heat transfer dynamics and temperature gradients is evident in the intensity and spread of thermal profiles.

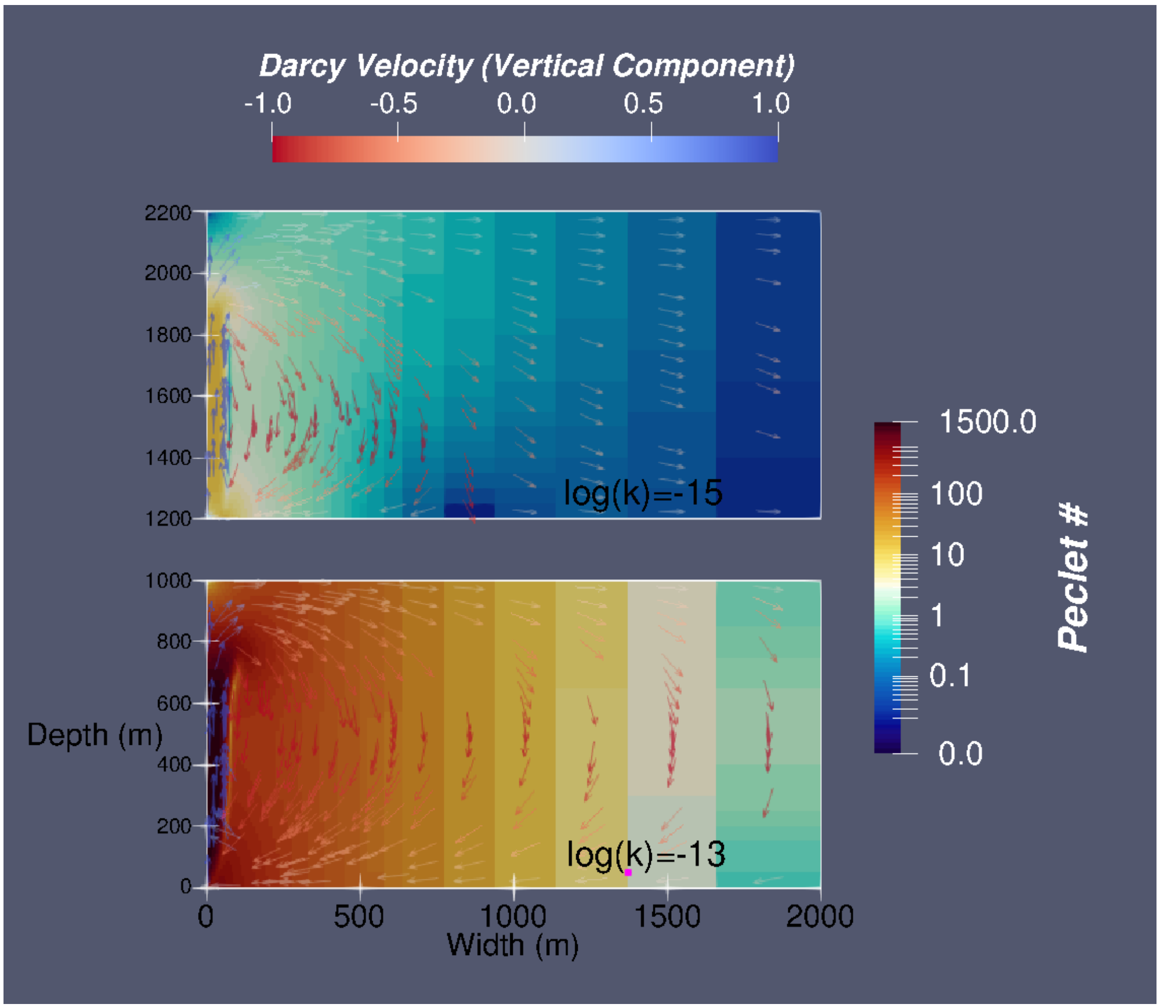

Figure 13. Distribution of Darcy velocity vector and Peclet number for two permeability values (log(k) = -15 and log(k) = -13). The top panel shows results for log(k) = -15, while the bottom panel shows results for log(k) = -13. Darcy velocity is represented by arrows and colored by the value of the Y component which is normalized by the maximum magnitude of the vector. The color bar represents the Peclet number, indicating the ratio of advective to diffusive transport, with arrows depicting the direction and magnitude of the vertical Darcy velocity.

CHAPTER IV

CHAPTER 4 : MULTISCALE SPATIAL PATTERNS IN GIANT DIKE SWARMS IDENTIFIED THROUGH OBJECTIVE FEATURE EXTRACTION

This chapter was previously published as Kubo Hutchison, A., Karlstrom, L., & Mittal, T. (2023). Multiscale spatial patterns in giant dike swarms identified through objective feature extraction. *Geochemistry, Geophysics, Geosystems*, 24(9), e2022GC010. I was the primary contributor for data analysis, methods, and paper writing. LK and TM contributed to conceptualization, data acquisition, and writing.

4.1 Story of the Land

Firstly, before this section, I'd like to acknowledge the story of the land of the Wallowa Valley and surrounding areas, which held and nurtured the indigenous people of the nimiipuu (Nez Perce) for generations before the colonial settlers violently displaced them. The Nez Perce lived in present-day Washington, Oregon, Montana, and Idaho along the Snake, Grande Ronde, Salmon, and Clearwater rivers, straddling buffalo and salmon country. They were known for their exceptionally strong bows and gorgeous horses bred through years of scientific husbandry. These valuable products, along with their strong morals and open-minded attitudes, allowed them to befriend most of the neighboring indigenous peoples and even the Lewis and Clark expedition. They rarely engaged in conflict with other tribes.

Hin-mah-too-yah-lat-kekt, popularly known as Chief Joseph (3 March 1860 - 21 September 1904), was a Nez Perce leader who led a group of 1,000 men, women, and children through their violent removal from the Wallowa mountain region of modern-day Oregon and pursuit for over 1,170 miles. Chief Joseph's home was the

Wallowa Valley, where his family and kin had lived for thousands of years. In 1855, 1863, and 1873, treaties were signed with the US Government, and both rights and goods were promised and then quickly and intentionally violated. Later in 1877, more Nez Perce were coerced into signing away more acres, including terms that all Nez Perce would move to a reservation east of Lewiston, Idaho. However, many Nez Perce, including the Wallowa Valley group led by Joseph, did not agree and were not consulted, and they refused to relocate.

The nontreaty Nez Perce, consisting of 600 women, children, elderly, and 200 fighters, started their journey on June 15, 1877, and ended on October 5, 1877, after 1,170 miles chased by over 2,000 soldiers of the U.S. Army. Forty miles from their goal, the Canadian border, Chief Joseph encouraged the few remaining leaders and young men to agree to stop fighting as they were freezing, starving, wounded, and scattered after three months of constant riding and fighting. The main leaders who had led the flight and outwitted the US Army had been killed along the way and in the final battle at Bear Paw. Chief Joseph was promised a safe return home for his people; however, they were taken in train cars and held as prisoners of war for over eight months, during which most of the initial survivors died.

After his release, Chief Joseph, who had gained fame and some respect among the U.S. Army and government after the killing of his people, met with President Rutherford B. Hayes, President Ulysses S. Grant, and President Theodore Roosevelt, to name a few, to plead for his land back according to the previous treaties and ceasefire promises. He was never able to return to the Wallowa Valley and is buried in Nespelem, Washington. He is noted by the naming of Joseph, Oregon; Chief Joseph Mountain, Oregon; Chief Joseph Pass, Montana; and Chief Joseph Dam on the Columbia River, which completely blocks salmon migration to the upper Columbia River system. Bill Taubeneck named the dike swarm focused on the Wallowa Mountains after Joseph in 1970.

Further reading about the history can be found at Josephy (1997); Nerburn (2005) and were used as sources for this section. More information about current efforts by Tribal members to restore salmon to the rivers can be accessed at the Columbia River Inter-Tribal Fish Commission (https://critfc.org/salmon-culture/tribal-salmon-culture/).

4.2 Introduction

Dikes are a primary mode of magma transport in the crust, connecting deep mantle melting with crustal magma storage zones and sometimes surface eruptions (Gonnermann & Taisne, 2015; Rivalta, Taisne, Bunger, & Katz, 2015). Dikes are sometimes known to spatially focus, across a variety of scales, into areas of high concentration known as dike swarms. These dike swarms may be associated with a single magmatic center such as the Spanish Peaks (kilometer scale) (Muller & Pollard, 1977; Odé, 1957) or extend to continental scale such as the Mackenzie Swarm ($>$ 1000km) (Baragar, Ernst, Hulbert, & Peterson, 1996; R. Ernst, Head, Parfitt, Grosfils, & Wilson, 1995; Fahrig & Jones, 1969). On Earth, the largest dike swarms are usually associated with anomalous mantle melting events that result in Large Igneous Provinces (LIPs) or tectonic breakups, and thus record significant magmatic-tectonic events in Earth's history (Bond & Wignall, 2014; R. E. Ernst et al., 2021a; Yale & Carpenter, 1998). Although we have observed a few instances of dike swarm emplacement in recent times (Ayele et al., 2007), we lack observations of active dike swarm of the scale that is often seen in the rock record, especially in the case of continental flood basalts (CFBs) (Bunger, Menand, Cruden, Zhang, & Halls, 2013; Bunger, Zhang, & Jeffrey, 2012). Dike swarms have also been observed or inferred on other planets such as Mars, Venus and Mercury, indicating that these features are essential to the movement of magma in a terrestrial planetary body (Crane & Bohanon, 2021; R. E. Ernst et al., 2021b; Grosfils & Head, 1994; Rivas-Dorado, Ruíz, & Romeo, 2022). Dike swarms also represent one of the most visually striking illustration of long-distance (10s to 1000s of km scale) vertical and lateral magma transport from crustal magma reservoirs.

Field studies of exhumed dikes swarms have provided insight into the dynamics and complexities of dike swarms at a range of scales (Jolly & Sanderson, 1995; Morriss, Karlstrom, Nasholds, & Wolff, 2020; Paquet, Dauteuil, Hallot, & Moreau, 2007; Ray, Sheth, & Mallik, 2007). Dike segment thickness varies from centimeter scale to 100s of meters while lengths vary from meters to 100s of kilometers or in cases such as the Mackenzie Swarms 1000s of kilometers (Baragar et al., 1996). At the largest end of the spectrum, CFB dikes have been observed to be over 100 m wide and kilometers to 100s of kilometers long, considerably larger than dikes associated with Ocean Islands or arc settings (Karlstrom, Paterson, & Jellinek, 2017; Mittal, Richards, & Fendley, 2021; Morriss et al., 2020; Thiele, Cruden, Micklethwaite, Bunger, & Köpping, 2020). Dike widths have been proposed to follow power-law distributions (Gudmundsson, 1995) although their is continued debate over whether log-normal or Weibull distributions may provide better fits considering issues with sampling the smallest scale of igneous dikes (Glazner & Mills, 2012; Jolly & Sanderson, 1995; Krumbholz et al., 2014).

Dike width distributions have been proposed to be controlled by magmatic overpressure (Babiker & Gudmundsson, 2004; Gudmundsson, 2002), host rock rheology (Karlstrom et al., 2017; Krumbholz et al., 2014), depth of emplacement (Delaney, Pollard, Ziony, & McKee, 1986), and the frequency of multiple injections within a single dike (Nicolas et al., 2008; H. C. Sheth & Cañón-Tapia, 2015). Some of these theoretical and field-based inferences have been tested by laboratory analog studies (Kavanagh et al., 2018; Kavanagh, Menand, & Sparks, 2006). These studies have highlighted the critical role of crustal layering (both rigidity and density layering), topographic stresses, magma buoyancy, and magma inflow rate in controlling the spatial pattern of dike propagation (e.g., vertical vs. lateral propagation) (Kavanagh, Boutelier, & Cruden, 2015; Urbani, Acocella, & Rivalta, 2018). Despite uncertainties about how well single dike models extrapolate to large dike swarms with complex inter-dike interaction (Gunaydin, Peirce, & Bunger, 2021), dike swarms have been widely interpreted in terms of paleostresses and as direct evidence of a transcrustal magma plumbing system (Mittal et al., 2021; Rivalta et al., 2015).

Remote sensing studies and field mapping have led to structural classifications of the largest scale structure of dike swarms (R. Ernst et al., 1995). Some dike swarms form radial or circumferential structures both focused on a localized center potentially associated with a magma reservoir or plume structure, while others are primarily linear bundles of subparallel segments. These two end members, which we will also focus on in this work, have largely been interpreted as representing two magmatic 'states': (a) the stresses are primarily endogenous to the magmatic system (e.g., a plume head) (Baragar et al., 1996; R. Ernst et al., 1995; Mège & Korme, 2004), magma chamber (Callot, Geoffroy, Aubourg, Pozzi, & Mege, 2001), or volcanic edifice (Acocella & Neri, 2009; Gudmundsson, 2006; Roman & Jaupart, 2014)) and (b) stresses are exogenous (e.g., tectonic stresses such as rifting (Buchan & Ernst, 2021a; John, Wallace, Ponce, Fleck, & Conrad, 2000)). Interpreted this way, the structure of dike swarms can illuminate the mechanism and driving forces of their emplacement (Mège & Korme, 2004), and provide a key tool for understanding the links between mantle melting, surface volcanism, tectonic rifting, and the Large Igneous Province (LIP) life cycle (B. Black, Mittal, Lingo, Walowski, & Hernandez, 2021).

Although it is clear that multiscale patterns exist in giant dike swarms, surface exposures of individual dikes are often dissected into individual segments due to erosion/exposure, topography, or limited physical access. This severely limits how we can directly infer the mesoscale (10-100 kms) and large scale structure ($>$ 100 kms) of dike swarms in a statistically robust manner from observations. For example, based on scaling analysis of Linear Elastic Fracture Mechanics (LEFM), dike segments in many databases are much shorter than predicted (Delaney et al., 1986; Morriss et al., 2020). At present, it is unclear if this mismatch is telling us something about the underlying magma transfer processes or is just a consequence of observational limitations. For dike segments datasets spread over large areas with many overlapping orientations, potentially spanning a long time, it is presently difficult to interpret the mesoscale structures in quantitative and statistically rigorous manner. In this study, we address this challenge by developing a novel method to objectively link dissected segments and utilize tools from image processing to analyze mesoscale and large scale structure in dike swarms. Our work builds upon existing work analyzing dike swarm geometries in a number of terrestrial and planetary LIPs (Buchan & Ernst, 2021a; R. Ernst et al., 1995; R. E. Ernst et al., 2021a).

To demonstrate the methods, we first study dikes of the Spanish Peaks region in Colorado, USA – an often cited example of small radial dike swarm – and then focus on the two large dike datasets: dikes of the Columbia River Flood

Basalt Group (CRBG) and Deccan Traps Flood Basalts (DT). Given the large scale (100 - 1000s of km), significant amount of overlapping dike orientations, and generally complex spatial patterns of dike segments, these two systems provide a useful test case to test and illustrate the utility of our analysis method. These two CFBs also represent some of the best studied Phanerozoic LIPs in the context of volcanic stratigraphy, geochronology, and magmatic processes (V. Camp, Reidel, Ross, Brown, & Self, 2017; Mittal & Richards, 2021a). We envisage that, if useful, our methods can be easily generalized to other dike swarm datasets on Earth (e.g., Mackenzie dike swarm) as well as Venus and Mars.

Our study specifically focuses on the following questions:

1. Do dike swarms mapped as distributions of many disconnected segments actually represent a smaller set of structurally continuous structures?

2. Are LIP dikes organized into coherent spatial patterns at a sub-swarm or swarm scale?

3. Do multiscale dike structures differ between the CRBG and Deccan Traps, and if so does this imply differences in emplacement mechanics?

To investigate these questions, we have developed a workflow for linking and clustering dike segments based on the Hough Transform, an algorithm commonly used in image processing (Ballard, 1981; Duda & Hart, 1972; Hough, 1962). We then use Agglomerative Clustering to classify mesoscale groupings of dike segments in the Hough space (Everitt, 1980; Sneath, 1957). We show that this method increases the lengths of dike segments by up to 3 orders of magnitude and may better represent the true scale of dikes in geologic data.

4.3 Methods

4.3.1 Hough Transform. The Hough transform (HT) is a feature extraction method extensively used in image analysis and computer vision (Duda & Hart, 1972; Hough, 1962). Originally designed to detect lines in images, the algorithm has been adapted to detect arbitrary shapes (Ballard, 1981). Although magmatic dikes are typically linear, they can curve as they propagate through different stress fields and thus depend on the length scale of the stress fields (Acocella & Neri, 2009; Davis, Bagnardi, Lundgren, & Rivalta, 2021). To illustrate the method, we will focus primarily on straight features in the present study and will not link dikes that curve along their length. Curving dike segments are removed in a preprocessing step before linking (due to the linearity filter). In practice, a majority of the LIP dikes are linear segments, and our choice does not strongly affect the overall results (Figure 2). A full extension to curved features is beyond the scope of the present study.

We use the Hough transform to help accomplish two goals: first, to link short dike segments into longer dikes; and second to evaluate the mesoscale structure of the dike swarm. The Hough Transform is independent of Cartesian midpoint location allowing us to link dike segments together that are far away from each other. In the classic HT formulation, initially an edge detection method is applied to an image to find discontinuities that may constitute shapes or features (Ziou & Tabbone, 1998). Each edge point is then transformed according to the following equation (Duda & Hart, 1972):

$$\rho = x \cos\theta + y \sin\theta \tag{4.1}$$

where θ is angle from the x axis in counterclockwise direction, and ρ is the distance of a ray from the origin to the line defined by the point and θ. Lines in Cartesian space become points in Hough space (HS); points in Cartesian space are curves in Hough space (Figure 18).

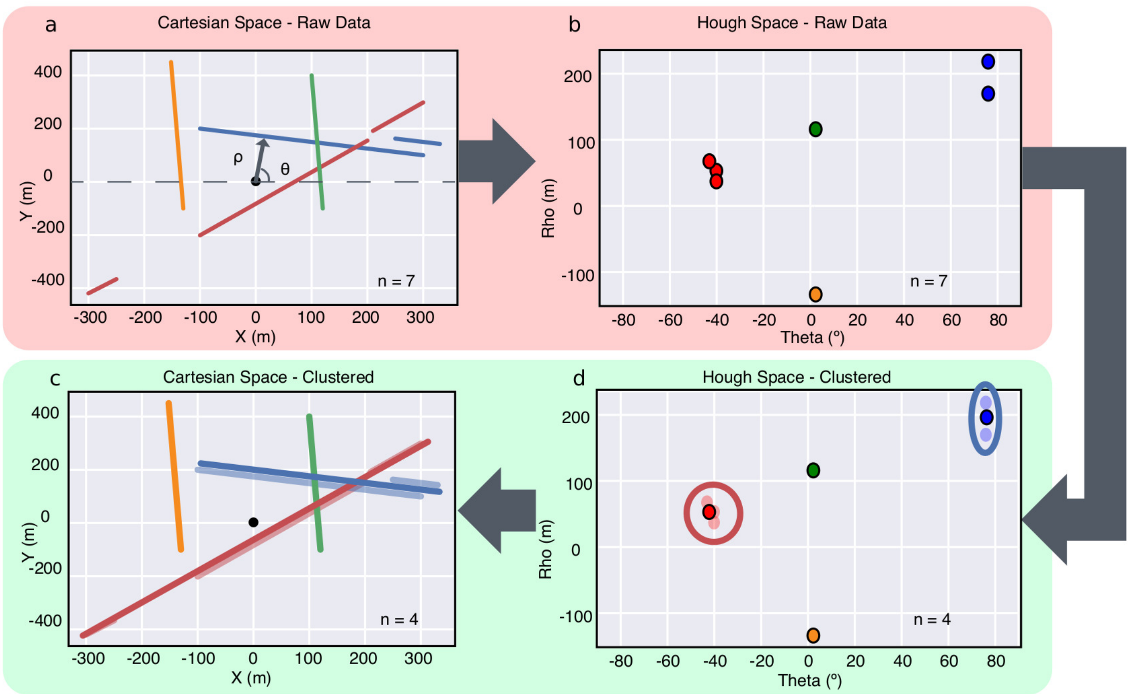

Figure 18. Dike linking algorithm using the Hough Transform. First, raw data in Cartesian space are converted into Hough space **A-B**. Agglomerative clustering is then performed on the data in Hough coordinates (**D**), in this example there are four dikes total and two (red and blue) clusters. The clusters are redrawn by connecting the endpoints of the segments in the cluster.

In the application here, we use dike segment maps derived from field mapping and remote sensing as data inputs. Each dike segment is pre-defined between two endpoints. We assume that dikes all represent straight lines (ignoring curving dike segments) and thus each dike segment is represented by a single point in the Hough space regardless of its length. For each dike segment in Cartesian space, we determine the angle (θ) using :

$$\theta = \tan^{-1}\left(\frac{x_2 - x_1}{y_1 - y_2}\right) = \tan^{-1}\left(-\frac{1}{m}\right) \tag{4.2}$$

where the dike segment is represented by its endpoints (x_i) and (y_i) $i = 1, 2$ and m is the slope of the line. Angle, measured in degrees, varies between $-90°$ and $90°$. The negative angles represent clockwise rotation from vertical (e.g., red line in Figure 18a) and the positive angles represent anticlockwise rotation (e.g., blue line in Figure 18a). An Hough angle of $0°$ represents a feature with North-South orientation or azimuthal bearing of $360°$. Angles of $-90°$ and $90°$ are equivalent representing a line of slope equal to zero or lineament oriented East-West. The perpendicular distance (ρ) is measured from a specified origin location and is calculated as

$$\rho = [(-m(x_1 - x_c) + y_1] \sin(\theta) = b \sin(\theta) \tag{4.3}$$

where b is the y-intercept of the line and either end point can be used to calculate ρ. The perpendicular distance ρ is measured in units of length and can be both positive and negative. Positive ρ indicates an intersection point to the right of the chosen Hough transform origin (e.g., red line in Figure 18 a), while a negative distance indicates an intersection to the left of the origin (e.g., orange line in Figure 18a).

An important part of our method is to choose an appropriate origin for the Hough transform, (x_c, y_c). The choice of origin modifies the resulting Hough space and the resulting clustering of line segmets. By default we set the center of transform to be the average of the midpoints of the dike segments. While this choice is not unique, we have found that our default choice produces physically reasonable results.

4.3.2 Clustering Dike Segments. To link dike segments, we apply Agglomerative Clustering as implemented by the SciPy library on the Hough-transformed datasets (Müllner, 2011; Virtanen et al., 2020)(Figure 18c). Agglomerative clustering is a bottom-up hierarchical clustering method that recursively pairs samples together with the closest nearby cluster until a set distance threshold is reached, after which clusters will not be merged.

We chose Agglomerative Hierarchical Clustering (AHC) due to the multiscale structure of the dike swarms and the observational dataset. On the dike scale level, field observations can include multiple segments of a dike structure oriented in the same direction. These segments have been unlinked due to exposure bias or small changes in surface expression such as en echelon segmentation. The dike scale is limited to the width of a 'single dike packet' in the system. The other scale is the mesoscale structure of the dike swarm wherein the packets of dikes are aligned due to magmatic or tectonic stress. Analysis of the large scale dike swarm structure can provide information about these forces change laterally/temporally and thus the nature of the magmatic system. Given the hierarchical nature of clustering, the AHC algorithm allows data analysis on the two (or more) scales in a natural manner.

The AHC algorithm requires the choice of two parameters for unsupervised clustering. First, the linkage method which determines how the proximity between two objects in a cluster is calculated. We choose complete linkage in which the proximity of two clusters is the distance between the two most distant objects

(Sorenson, 1948) since we found that it consistently provides the accurate and noise-robust results for a range of synthetic dike datasets.

The second parameter is the distance over which the clusters will not be merged (d). We find that this is the most critical algorithmic parameter. The goal of our clustering analysis is to link segments that may be on the same line or along a narrow axis. Thus, we use a scaled Euclidean distance metric to determine the distance between data in the HS, scaling it by the angle cutoff ($\delta\theta$) and intercept cutoff ($\delta\rho$). For each dataset, we choose strict angle cutoffs of 2° while setting the intercept cutoff to the mean length of the dike segments. We choose this limit because it is representative of the smaller segment-scale length in the databases. Our sensitivity analysis for the CJDS dataset suggests that changing the ρ cut off has minor impact on the results. In contrast, changing the angle cutoffs can, unsurprisingly, affect the results significantly.

We set the distance cutoff (d) in the AHC algorithm to 1. This implies that if two points are exactly parallel ($\theta_1 = \theta_2$), their distances must be less than or equal to $\delta\rho$ from each other in order to cluster together. A schematic illustration of the AHC and dike linkage process is shown in Figure 18.

4.3.2.1 Robustness and Dike Characteristics. After linking is performed on the Hough Space, we examine the clusters in both Hough and Cartesian coordinates for robustness. There are two ways in which transforming between Hough Space and Cartesian space can introduce distortion. First, the difference between two values of the line ρ is approximately equal to the perpendicular distance between two parallel lines. However, there is distortion of this value in HS far from the Cartesian coordinate origin. We show that this occurs increasingly for large differences in angle but can be avoided by comparing only segments with similar θ. We combat this by choosing a coordinate origin which is the mean of segment midpoints and by breaking up the large data sets into regional subswarms. Second, in Hough space, lines with $-90°$ and $90°$ have the same horizontal orientation (E-W from a map point of view). To solve this issue in Hough space clustering we simply rotate the dataset so that the median angle is centered on 20 degrees. This minimizes the number of clusters that cross $-90°$ and $90°$ and $0°$ for the datasets of interest.

Finally, in the Hough space, lines are assumed to be infinite so the clustering does not account for where a segment falls on the line. We calculate a variety of metrics to give a sense of how the segments in a cluster are oriented to give a sense of structure. In Cartesian space, to find a new line segment to represent the cluster, we take the average orientation from all segments and extend the line so that it's tips represent the extremity of the individual segment endpoints.

We fit a rectangular box around the group of segments to find the dike segment 'packet' length and the dike segment 'packet' width, where the length is oriented along the packet orientation and the width is measured perpendicular to the length. *When referring to cluster length or width, we are referring to this measure and not individual segments.* As another measure of cluster distribution in Cartesian space, we calculate the maximum Euclidean nearest-neighbor distances between segment midpoints. This value is then normalized by the length of the cluster. For a cluster of only two segments, this number is always 1. For larger clusters, this number represents the distance between the two furthest segments. We assume that clusters where the two furthest segments are significantly far from each other, over half the length of the cluster, are less robust. *In subsequent analysis, we will refer to the subset of clusters filtered first by cluster size (* > 3

segments) and by the maximum nearest-neighbors distance (< 0.5) as the 'filtered' database.

4.4 Datasets

In this study, we have chosen three datasets to focus on and apply our methods. First, the Spanish Peaks which likely represents a volcanic edifice scale structure. Second, the Columbia River Basalt Group data set which includes four subswarms (Ice Harbor, Chief Joseph, Monument, and Steens) with the majority of our attention paid to the largest, the Chief Joseph Dike swarm (CJDS). Finally, we apply our method to the CFB province scale and examine the Deccan Traps datasets and the major subswarms (Central, Coastal, Narmada-Tapi, and Saurashtra) (GSI District Resource Map, 2001; Mittal et al., 2021). The Spanish Peaks dataset acts mainly as a test dataset for our methods while we will compare the two CFB related swarms to investigate qualitatively the characteristics of CFB dikes. For each of the CFB datasets, the clustering is performed on the subswarm level to minimize Hough Transform (HT) distortion from the choice of an origin (refer to Table 3 for specific clustering parameters). It is important to note that these datasets have been compiled from various sources (mentioned later). These include varying levels of ground truthing and information about dike thickness and ages. Thus, the presence and exact location of each dike segment in the database has not been verified in this study, but it is the best data currently publicly available. Certainly there are more unmapped dikes which have not been included and in some cases the mapping quality cannot be easily verified (Morriss et al., 2020). All the datasets and descriptions of the processing steps are available in Kubo Hutchison et al. (2023).

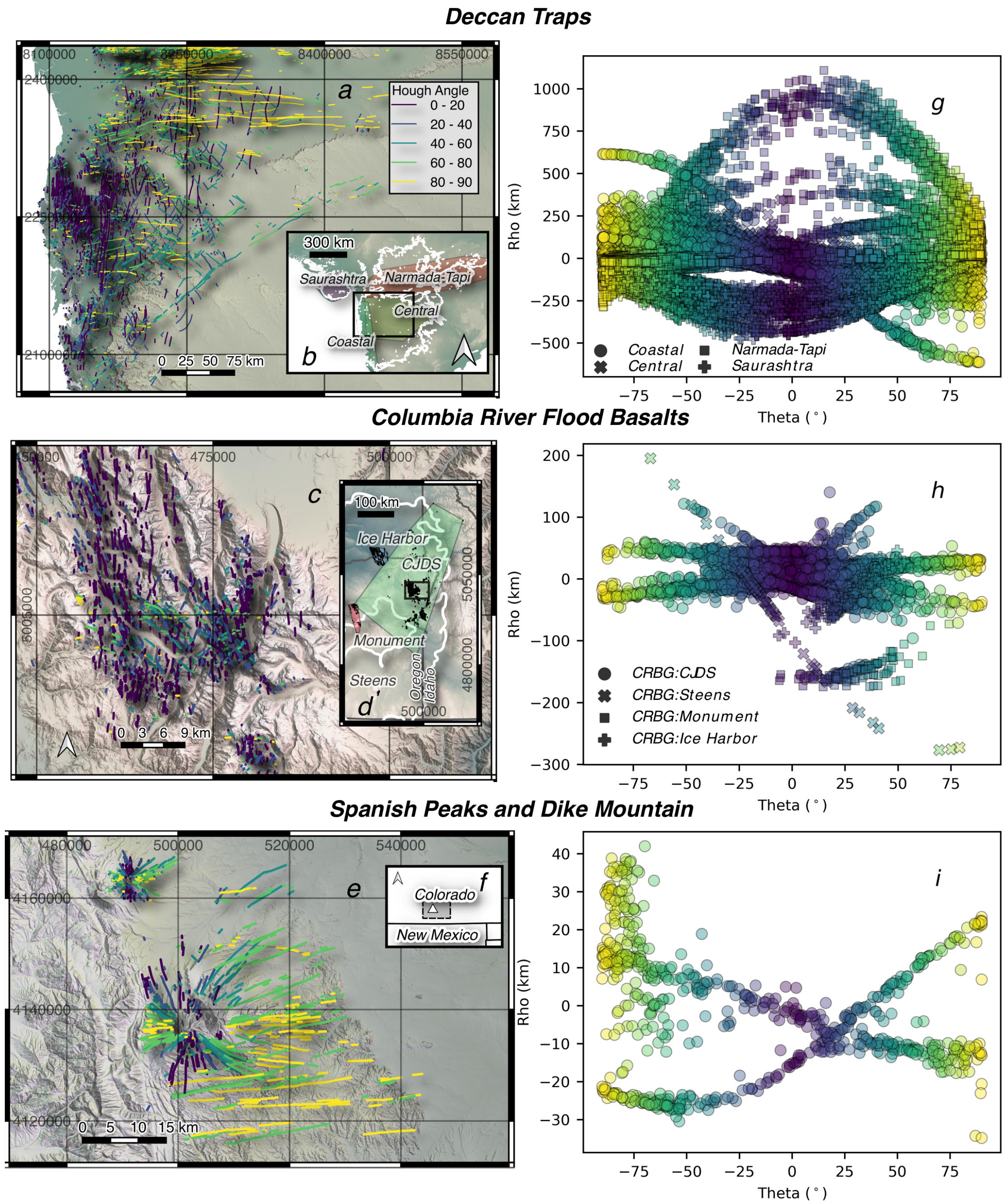

Figure 19. Map figures showing portions of the three datasets (**A.**,**C.**, **E.**) with the large scale structure show in the insets (**B.**,**D.**, **F.**) along with their respective structure in the Hough Transform space (**G.**,**H.**, **I.**). All figures show the absolute value of the dike segment angle (θ) in degrees colored in terms of the colorbar in **A.** White lines in the inset maps of **B.** and **D.** show the extent of mapped lavas.

4.4.1 The Spanish Peaks dike swarm.

The Spanish Peaks area is located in southern Colorado in the Rio Grande Rift and is made up of two intrusive stocks and associated dikes in Tertiary sediments (Figure 19e,f). Spanish Peaks is one of the most commonly cited and studied radial dike swarm (Johnson, 1961; Odé, 1957). Spanish Peaks dikes exhibit three major components, first a radial structure centered on West Peak, a linear trend that strikes N. 60° E, and a secondary radial structure centered on Dike Mountain also known as Silver Mountain. Each intrusive body and the associated dikes represent distinct magmatic phases and compositions (Penn & Lindsey, 2009). The radial swarm of the Spanish Peaks is diffusely centered on West Peak although some dikes intercept outside the Peaks or in East Peak. West Peak is a quartz syenite dated to 24.6 $\pm$ 0.13 Ma while the East Peak is composed of granite and granodiorite porphyry dated to 23.9 $\pm$ 0.08 Ma (Penn & Lindsey, 2009). The dike compositions range from gabbro lamprophyre to granite porphyry (Johnson, 1961). The nearby Dike Mountain or Silver Mountain lies 50 km NW of the Spanish Peaks, and its associated dikes are syenodiorite (Johnson, 1961). Although the exact relationship between the two stocks and Dike Mountain is unclear, the Dike Mountain is dated as older than the Spanish Peaks intrusions (Penn & Lindsey, 2009). We chose to include these dikes in our database to demonstrate the algorithm's ability to differentiate between two closely oriented radial swarms. Using this full dataset, we can also test our method's ability to devolve spatially overlapping radial and linear swarms. The dikes were digitized based on mapping in (Johnson, 1961) using QGIS software producing a shapefile of all dikes (linear and curving) which we have included in the supplementing information of Kubo Hutchison and Dufek (2021). These dike segments are then preprocessed using the steps described in

Kubo Hutchison et al. (2023). The final database used for clustering is available in Kubo Hutchison et al. (2023).

4.4.2 Columbia River Basalt Group Dataset. From the CRBG, we investigate the Chief Joseph, Ice Harbor, Steens Mountain, and and Monument dike swarms both individually and together as compiled in (Morriss et al., 2020) (Figure 19a,b). The CRBG is the youngest flood basalt province on Earth and covers an area of approximately $210,00$ km^2 (Reidel, Camp, Tolan, Kauffman, & Garwood, 2013). Like other CFBs a majority of the CRBG was erupted in a short 'main phase' pulse, 17.2 Ma to 15.9 Ma with narrowing windows in progressive studies (Kasbohm & Schoene, 2018; Reidel, Camp, Tolan, Kauffman, & Garwood, 2013). Previously, dike swarms associated with CRBG have been linked together to form a radial dike swarm originating from an extensive centralized magma chamber in eastern Oregon (V. E. Camp & Ross, 2004; Glen & Ponce, 2002; Wolff, Ramos, Hart, Patterson, & Brandon, 2008a).

The Ice Harbor subswarm is associated with post-main phase Saddle Mountain Ice Harbor flows dated ate 8.5 Ma (Reidel, Camp, Tolan, & Martin, 2013). The dike positions are inferred by high-resolution aeromagnetic survey (Blakely, Sherrod, Weaver, Wells, & Rohay, 2014; Morriss et al., 2020). The dikes appear mostly linear and strike N-NW at approximately $27 \pm 11°$. Monument dike swarm (Cahoon, Streck, Koppers, & Miggins, 2020; Fruchter & Baldwin, 1975) located in central Oregon was mapped to have a similar orientation to the Ice Harbor swarm $30 \pm 14°$. Our Steens dike database consists of 69 basaltic dikes exposed on the flanks of Steens Mountain mapped by satellite imagery in (Morriss et al., 2020). Steens dikes show a range of orientations and represent both the most southern exposures of dikes in the database. These dikes likely are linked to the

CRBG's earliest eruption of the Steens Basalt (Kasbohm & Schoene, 2018; Morriss et al., 2020).

The largest of the CRBG associated databases, the Chief Joseph Dikes Swarm (CJDS) is mainly located in the Wallowa mountain regions of Eastern Oregon covering an area 100 km wide by 350 km long. The CJDS has been linked via geochemistry to the main phase formations of the CRBG : the Imnaha and Grande Ronde basalts. However, geochemistry has also revealed compositions spanning nearly the entire range of CRBG eruption members with the swarm (Morriss et al., 2020; Petcovic & Dufek, 2005a). This suggests the area was a hub of overlapping intrusive activity for significant periods of time. This is also supported by the high segment density throughout the region of up to 5 segments/km^2. Overall, CJDS exhibits a linear orientation with strike NW at $6.0 \pm 30°$. However, significant secondary trends, offset in angle, are also present for the dike swarm which complicates the view of the swarm as singularly linear.

4.4.3 Deccan Traps Dataset. The Deccan Traps flood basalt consist of four main dike swarms the Saurashtra swarm, Narmada-Tapi, which extends from Saurashtra through the Mandla Lobe, the Coastal Western Ghats swarm, and east of that the Central Dike swarm or Nasik-Pune swarm (Mittal et al., 2021) (Figure 19c,d). The dike dataset was compiled by (Mittal et al., 2021) resulting in 29,000 dike segments based on a variety of sources including satellite imagery, district resource mapping, and digital elevation maps but the majority of segments are based from Geological Society of India field mapping (1:50k maps, (GSI District Resource Map, 2001)).

The western Narmada-Tapi region shows the highest density of dike segments and appears largely linear with ENE-WSW orientation along the riftgraben stucture (Ray et al., 2007; Shukla, Mallik, & Mondal, 2022). Dike segments decrease in frequency from west to east but are often clustered around rift-faults (Bhattacharji, Chatterjee, Wampler, Nayak, & Deshmukh, 1996). The Saurashtra subswarm shares strong ENE-WSW orientation but also exhibits a range of angles. The Coastal Swarm, located along the Western Indian coast, shows a N-S orientation along the Western Ghats escarpment (Vanderkluysen, Mahoney, Hooper, Sheth, & Ray, 2011). Finally, the Central or Nasik-Pune swarm shows little angle preference and has some of the longest individual segments lengths (up to 69 km, (Mittal et al., 2021)). In previous studies, the Central and Coastal swarms have been roughly separated by the Western Ghats escarpment. However, we choose to combine these two swarms due their large overlap in Hough Transform space and the presence of mapped dikes that cross this boundary (See Figure 19c,d). We will refer to it collectively as the Deccan Central swarm in the rest of the paper.

We anticipate that both the CFB datasets are likely incomplete due a combination of vegetation cover, lack of exposure, and the large areal extent. Thus, they are excellent candidates for our clustering algorithm to link individual dike segments. In both cases, the majority of outcrops occur at shallow paleodepths. The paleodepth of the CJDS is estimated to be $\approx$ 2 km (Morriss et al., 2020). The depth of original intrusions for Deccan is unknown but is also likely shallow (¡4 km) since a large majority of the dikes are emplaced in either Deccan basalt or shallow basement (Ray et al., 2007; H. C. Sheth & Cañón-Tapia, 2015; Shukla et al., 2022). Many other giant dike swarms have also been shown to have relatively shallow to mid crustal depths of $6-15$km (R. Ernst et al., 1995). The limited vertical exposure limits the inferences about the deep crustal plumbing systems in

Table 3. Hough transform and clustering parameters for each dataset

Dataset	**Dike Segments No.**	**Rho Threshold (m)**	**HT Center Location (UTM)**	**Total/Filtered**
Spanish Peaks	698	2013	(-11684090, 4503618)	191/28
CRBG:CJDS	4064	433	(475083, 4976408)	1057/91
CRBG:Monument	103	1201	(306813, 4943505)	20/1
CRBG:Ice Harbor	112	4410	(369188, 5104698)	31/1
CRBG:Steens	61	408	(370992, 4721712)	10/1
Deccan:Central	5512	3436	(8174542, 2237149)	1459/219
Deccan:Narmada-Tapi	11788	1730	(8403558, 2495692)	2279/600
Deccan:Saurastra	8638	1562	(7907507, 2440048)	2108/405

CFBs. Nevertheless, the dike swarms are extremely important for understanding how magma is erupted from CFBs and thus what effects such voluminous eruptions would have on the atmosphere and biosphere.

4.5 Clustering Results

We applied the Hough Transform to dike segment databases from the Spanish Peaks, Deccan Traps, and CRBG then performed clustering in the Hough space to link clusters with similar orientations. In Figure 19g,h,i, we show the corresponding data from the Hough Transform segment data for each of three datasets. As an example of what the algorithm does visually, we show three representative examples of three clusters from the Chief Joseph, Deccan Central, and Deccan Narmada-Tapi dike swarms respectively (Figure 20).

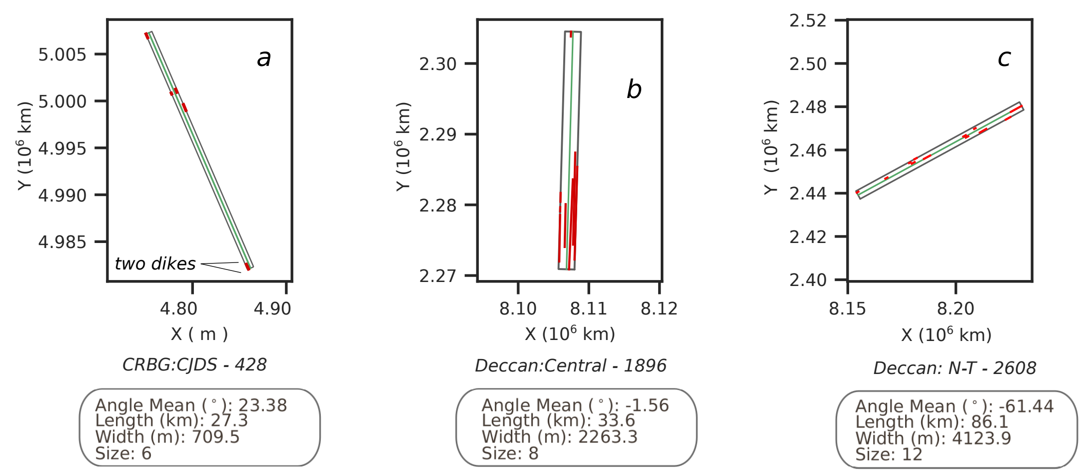

Figure 20. Example clusters from the Chief Joseph, Deccan Central, and Deccan Narmada-Tapi dike swarms (a,b,c respectively). The red lines show the mapped dike segments, the grey box shows a rectangle fitted around segments while the green line shows the average line of the cluster based on the HS orientation.

For each dataset, we see significant increases, by up to three orders of magnitude, in dike cluster length compared to the unclustered segment database (Figure 21). This is seen for all three full datasets and also at the subswarm scale.

Furthermore, the filtered dike dataset (clusters with size $>$ 3 and max nearest neighbors distance $<$ 0.5) are on average longer than the full clustered database. We do not account/incorporate clustered dike length in the filtering step and find that there is only a weak positive relationship of cluster size and cluster length (See Figure S3). We find that very long dike clusters ($>$ 200km) have cluster sizes of 2-18 although clusters of over 5 are relatively rare (Figures S2). Overall, the results of our dike linkage analysis for the three datasets suggests that dike swarms mapped as distributions of many disconnected segments likely represent a smaller set of continuous structures.

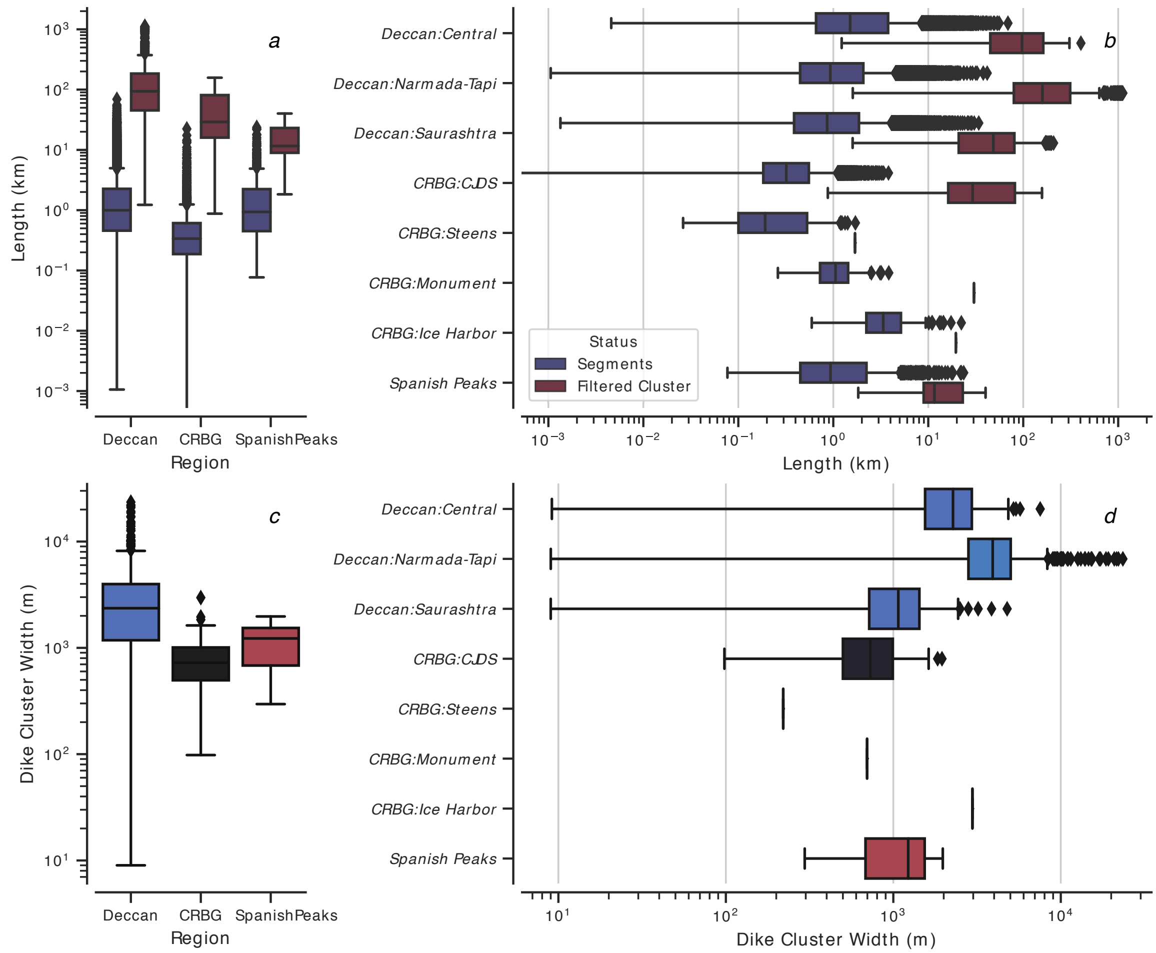

Figure 21. **A.** Log-scale lengths of the segment database and filtered linked database in blue and red, respectively for the three regional databases. **B.** Lengths broken down by subswarm for each region. **C.** Log-scale widths of dike clusters found in the linked database, and filtered linked database in blue and red respectively for the three regional databases. **D.** Dike cluster widths are shown broken down by subswarm for each region.

The Deccan Traps dikes show the longest dike clusters with the extrema reaching over 1000 km and a median length of 55 km (Figure 21). Although the individual segment lengths are roughly similar between the Saurashtra and Narmada-Tapi subswarms, the Narmada-Tapi swarm shows the longest linked dikes (1100 km) of all subswarms, eclipsing even the longer segments of the Central swarm. The utility of our linkage algorithm is even more clearly exemplified for the CRBG dataset. Before clustering, this dataset had the short segments with an average length of only 400 m. However, after linking, the dike clusters have a median length of 10.6 km with some dikes reaching over 200 km (Figure 21). Within the CRBG dataset, the Ice Harbor and CJDS show the longest lengths but we note that the Ice Harbor segments are inferred through aeromagnetic survey (Blakely et al., 2014) as opposed to field survey for CJDS dataset.

The second scale over which we can evaluate diking activity is dike or cluster width. The median dike segment width observed in the CJDS dataset is 8 m (Morriss et al., 2020). It is slightly higher for the Deccan dikes at 10 m, although the available segment width data on Deccan dikes is relatively sparse (Ray et al., 2007). After clustering, the Deccan shows higher dike packet widths ($\sim$ 2300 m) than the CRBG ($\sim$ 700 m) or Spanish Peaks ($\sim$ 1200 m). This is not surprising given the higher ρ clustering thresholds (See Section 4.3.2) for Deccan. Interestingly, the dike packet "width" is also the largest for the Narmada-Tapi swarm ($\sim$ 3 km) compared to $\sim$ 2 km and $\sim$ 1 km for the Central Deccan and the Saurashtra swarms respectively. This suggests that the longest Narmada-Tapi linked dikes are composed of a number of similarly oriented linear features.

4.6 What do the clusters physically represent?

Based on all our analysis above, we posit that the clusters found using our algorithm can present two possible interpretations: first, a cluster may represent a single fracture that is one continuous magma pathway including a set of en echelon fractures which have broken down due to rotations in the local stress field; secondly, it may represent a family of fractures which may have been emplaced over long periods of time. Figure 20 shows examples of these different possible interpretations. Figure 20a shows short dike segments aligned on a narrow area with high aspect ratio. Figure 20b however shows many segments overlapping over a range of 2.2km . Meanwhile, Figure 20c shows a long cluster (86 km) with many segments oriented evenly across it's length with some overlap. However, this still may not represent a single fracture but rather a series of related dikes emplaced over time, but being influenced by the same stress fields and re-using existing fracture pathways (from the previous dike). Whether the linked dike features represent lateral flow over 100s or 1000s of kilometers in a single dike cannot be confirmed just with our linking method and requires further follow-up geochemistry and geochronology of the connected segments. However, our results clearly suggest that stresses are maintained over 1000s of kilomaters and for the duration of emplacement of the dikes.

4.6.1 Linear Elastic Mechanics Analysis. Dikes are classically modeled as isolated Mode I fractures (Rubin, 1995). Dike widths and lengths are related to each other based on the magma overpressure and host rock properties (Gudmundsson, 2002; Rubin, 1995). Using linear elastic fracture mechanics (LEFM), the predicted scaling for the length to width ratio is

$$\frac{L}{W} = \frac{E}{2\Delta P(1 - v^2)} \tag{4.4}$$

where L is the length, W is the width, E is the Young's Modulus, v is the host rock Poisson's ration, and $\Delta\Delta P$ is the magmatic overpressure. Using typical values, $E = 10 - 30$ GPa, $v = 0.25$, and $P = 1 - 10MPa$), we expect this ratio to be $\sim 10^3 - 10^4$.

In Figure 22a we have plotted the dike cluster width and dike cluster length with three scaling ratio lines plotted over them (10^3, 10^1, 10^1) based on Equation 5. The CJDS data shows a bimodal distribution with one peak falling on the 10^2 line and the other falling between the 10^2 and 10^1 lines. The Deccan dikes are overall wider and longer than the CJDS dikes and fall mostly between the 10^2 and 10^1 lines but with a significant portion on or above the 10^2 ratio line. Breaking down the Deccan subswarms we find that Saurashtra subswarm shows overall shorter dike cluster lengths and widths more in line with the CJDS while the Deccan Central and Narmada-Tapi subswarms show significantly longer dikes. Overall, few clusters are close to the 10^3 ratio. Thus, we conclude that our dike clusters do not follow the expected LEFM predictions and are typically too wide. One potential explanation for the our results is that the effective crustal strength on large scales is weaker than the rock material properties due to presence of pre-existing fractures, thermal stresses from dike emplacement, and/or some viscoelastic stress relaxation (Eberhardt, 2012; Kavanagh & Pavier, 2014; Ma, Li, Wang, Wu, & Li, 2020; Thiele et al., 2020).

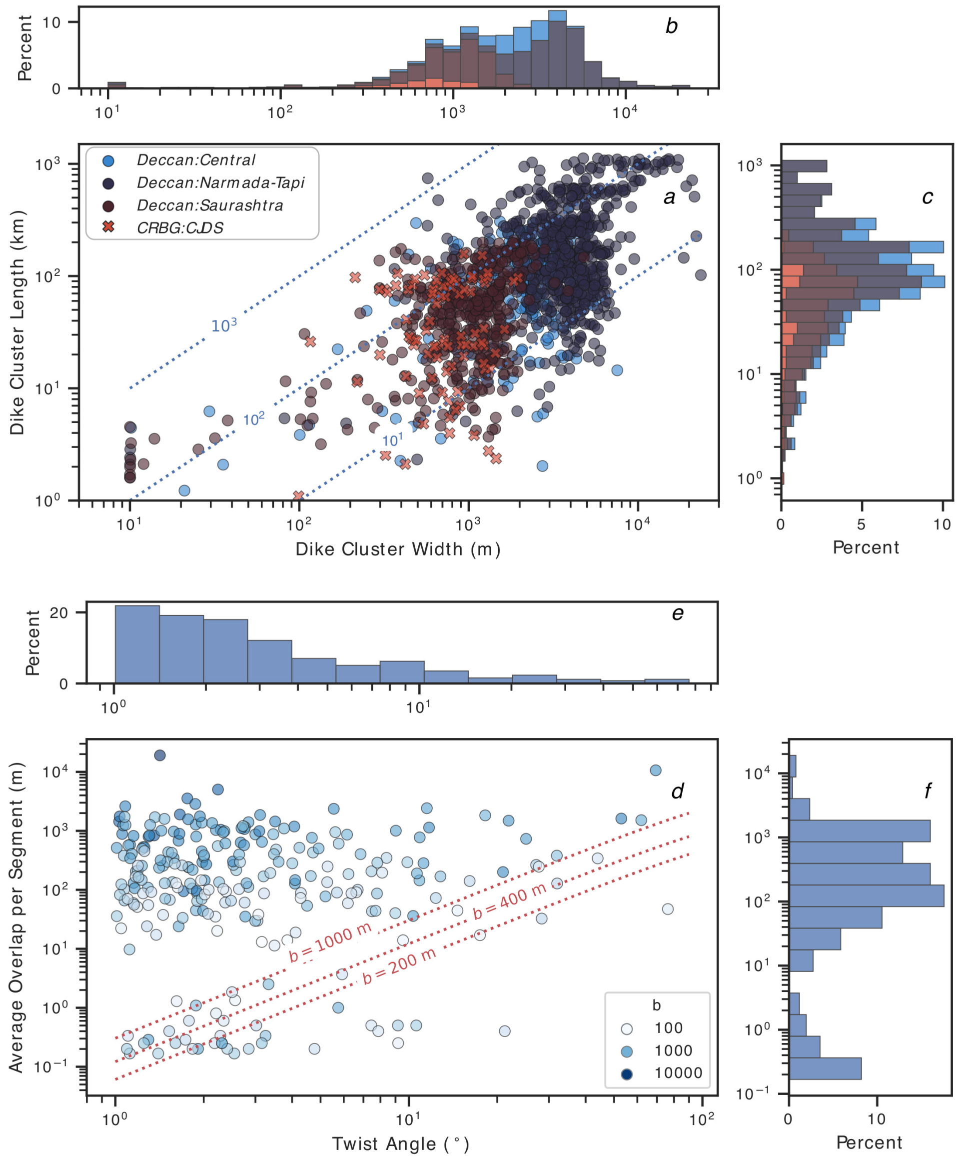

Figure 22. **A.** Log-scale widths of clusters plotted against the log-scale cluster lengths. Three trend lines (blue dashed lines) showing length to width ratios of 10^3, 10^2, 10^1. **B.** and **C** show the distribution of the dike cluster widths and lengths respectively. **D.** plots the twist angle in degrees versus the calculated average overlap per segment in meters (log-scale) only for a subset of the data ($n = 256$) which has twist angle greater than 1° and overlap greater than 0.1 m. The color of the dots indicates the half-segment length (b). In red dashed lines, three trend lines are plotted over the data indicating b of 200 m, 400 m, 1000 m. **E.** and **F** distribution of twist angle and overlap respectively.

To further evaluate intra-cluster distribution of segments, we examine predicted scaling for isolated dikes in a spatially variable (rotated) stress field, which often exhibit segmented or 'en echelon' distribution (Pollard, Segall, & Delaney, 1982). To do this we look at the overlap between segments and the twist angle (Figure 22). Twist angle is calculated as the difference between the mean angle of the cluster and the line of best fit over the cluster midpoints. A twist angle of zero indicates the segments are aligned with the other segment endpoints. A higher twist angle indicates that the segments are offset from the line of their midpoints which could indicate en echelon type fracturing.

En echelon type fractures mix Mode I and Mode II type fractures associated with changes in the regional or local stress field due to material inhomogeneities (Pollard et al., 1982; Rubin, 1995). We calculate the total overlap across the cluster in meters then divide by the size of the cluster to find the average overlap per segment. Twist angle and overlap can be related together for en echelon type fractures using the following equation:

$$\mathcal{O} = l(1 - \cos(\omega)) \tag{4.5}$$

where $\mathcal{O}$ is the overlap per segment, l is the segment half length, and ω is the twist angle based on equation 8b in (Pollard et al., 1982) when the distance between segment midpoints is approximately equal to the segment half length. Due to the clustering parameters, the distance between two segments is necessarily less than the segment average length. On Figure 22d, we show this calculation for various segment half lengths which span the representative values for the different datasets ($b = 200, 400, 1000$ m). Although some of the data is well represented by the lines, the majority of the data shows higher levels of overlap, or that the endpoints of dike segments within a packet are closer together. If the equation above holds true, this may suggest post-emplacement widening of the fractures by secondary processes as suggested in (Pollard et al., 1982) or mulitple generations of dikes being emplaced in the same areas.

The spacing between individual dike segments in a cluster (ρ) can also illuminate how the clusters were potentially formed. As a set of dikes fractures the host rock the energy necessary to maintain the growth of the dikes depends partially on how close they are together and how the strain of multiple dikes interact which is a topic of active research. (Bunger et al., 2013) established a scaling analysis for the spacing of first generation fractures in a dike swarm and found it to be primarily dependent on dike height (H) since the further apart between fractures reduces the energy necessary to maintain the fracture. They found that for a dike with time variable magma supply, two potential scalings can arise : $\rho/H \sim 0.3$ or $\rho/H \sim 2.5$. Taking dike height to be approximately crustal thickness for LIP dikes ($H \sim 30$) and using the standard deviation of ρ in a cluster as the dike segment spacing, we find that our clusters do not follow the predicted ratio (~ 0.05, still less than predicted even for $H \sim 10$ km). This suggests that dike segments are closer together than theoretical models which may indicate that successive dike emplacement occured between the first generation of dikes to maintain low interaction between newly forming fractures. Notably the cut off for clustering based on $\delta\rho$ is also significantly less than the (Bunger et al., 2013) scaling. Thus, our final conclusion isn't unexpected but it may support the idea that these clusters likely represent multiple generations of dike emplacement.

4.6.2 Dike Swarm associated crustal dilation. At a province scale, dilation due to diking can cause significant strain in the upper crust and has implications for the emplacement of the plumbing system and the crustal stress field (Thiele et al., 2020). Dilation is calculated as

$$D(x_i) = \sum_{n=1}^{N} \overline{w} \cos(\theta) \tag{4.6}$$

for the EW direction and

$$D(y_i) = \sum_{n=1}^{N} \overline{w} \sin(\theta) \tag{4.7}$$

for the NS direction where x_i and y_i are bins in the EW and NS directions, N is the number of dikes in each bin, $\overline{w}$ is the median width of the dike segment, and θ is the angle in Hough space. The average center of dilation is found by taking the weighted average of the bins using $D(x_i)$ and $D(y_i)$ as weights. These calculations can be performed for the segment or cluster database. The segment database provides a lower bound estimate of dilation while the linked clusters provide an upper bound, as long as our dike dataset is reasonably complete. We used a typical segement width of 8 and 10 m for the CRBG and Deccan respectively (Morriss et al., 2020; Ray et al., 2007; Shukla et al., 2022)

The CRBG is dominated by EW dilation as is expected by the dominantly NS trending CJDS (Figure 23). The maximum dilation seen in the segment database ($\sim$ 1300 m and $\sim$ 1000 m for the EW and NS dilation respectively) are similar in magnitude but on average EW dilation is higher. For the clustered dataset however, maximum EW dilation significantly eclipses NS dilation ($\sim$ 3100 m and $\sim$ 700 m for the EW and NS dilation respectively). The Deccan datasets show dominant NS dilation with $\sim 2,800$ m and $\sim 10,800$ m for the segment and linked databases respectively (Figure 23). The EW direction showed lower amounts of dilation with $\sim$ 2500 m and $\sim$ 4600 m for the segment and linked databases respectively. This leads to a maximum strain of approximately 1% for both the Deccan and CRBG datasets in their maximum directions of dilation and 0.3% and 0.14% in the minimum direction of dilation respectively. Strain is calculated using the maximum dilation over the NS and EW ranges of each dataset. Notably, in both LIP datasets, the area-weighted center of dilation implied by the clustered dike segments does not exactly align with dike outcrops (Figure 23 Dark blue dashed lines).

4.6.3 Summary Interpretation. In conclusion, dike cluster length does not necessarily represent one uninterrupted singular magma pathway or crack caused by fracturing (although in some clusters it may). Instead, dike packet width is likely the zone of influence that a dike may exert in the shallow crust. Dike clusters are indicative of sustained areas of diking activity from crustal magmatic system over a timescale when the regional stress field was relatively constant. Looking at the overlap within a cluster (Figure 22d), we see more overlaps than would occur in a simple en echelon fracture which may indicate that the observed overlaps are due to emplacement of multiple dikes in a zone of weakness over time by reactivation. Further, the continued magmatic emplacement in a localized region would reduce the crustal strength and introduce local stress heterogeneity that can further change the dike characteristics from the pure LEFM theoretical end-member. Notably, we are looking only at the end state of the magmatic plumbing system so the dike scale is integrated over the time of the activity.

Interpreting each cluster one-by-one is beyond the scope of this paper and would require other information about the dike segments such as geochemistry, paleomagnetic or radiometric dating, and more detailed field observations. Dating

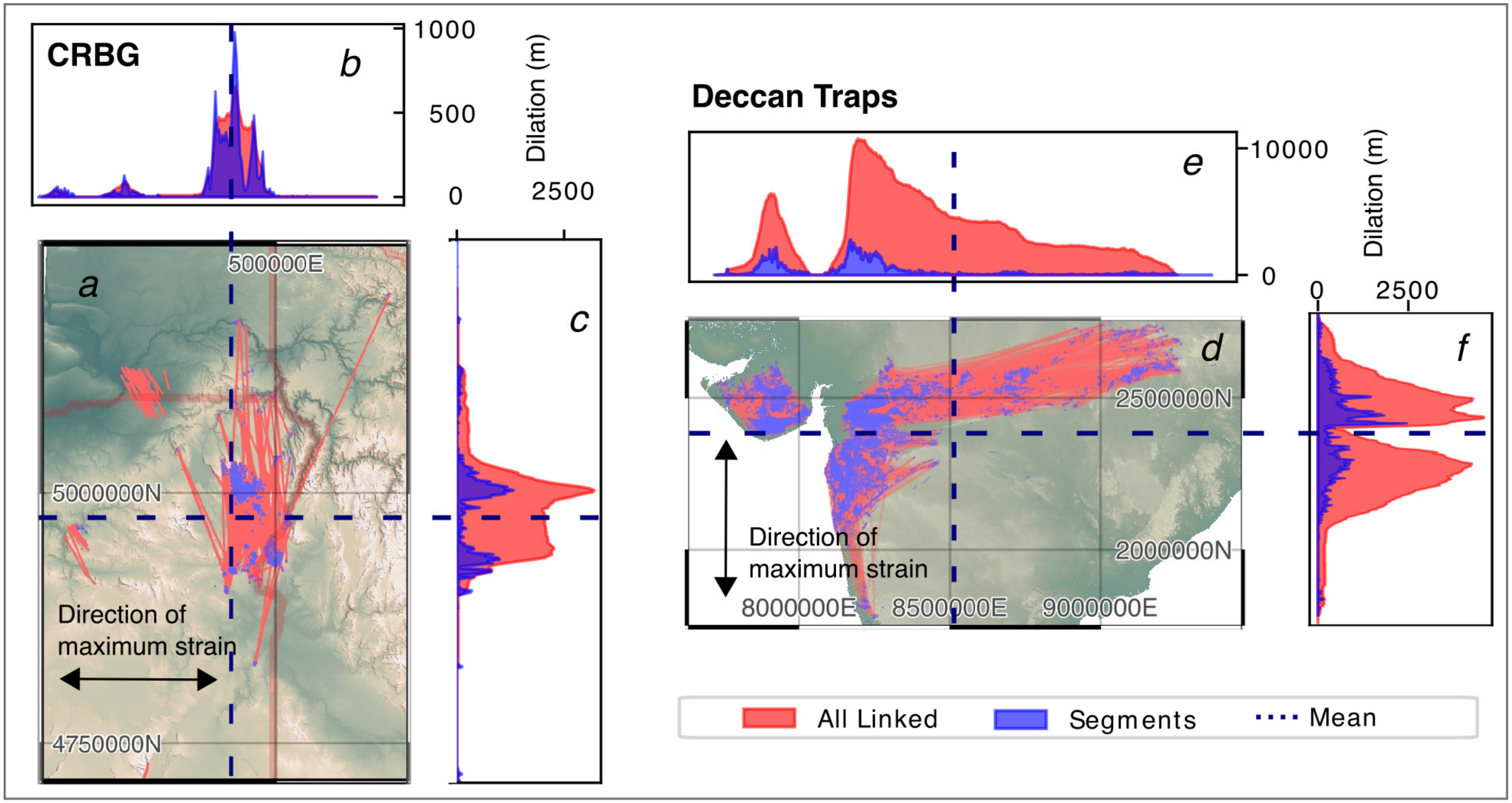

Figure 23. The left planel shows the CJDS while the right shows the Deccan dike swarms. **A.** and D. show the segment database (red) overlaid on the linked clusters (blue) while the two side panels **B.** and C. and **E.** and F. show the dilation in the NS and EW directions for the segments and linked clusters of the CRBG and Deccan datasets respectively. The dark lue dashed line shows the segment density weighted center of dilation.

of the dike segments could establish whether the segments were formed in the same pulse of magma or if it was emplaced over long periods of time. Geochemistry can change along the length of the dikes (Morriss et al., 2020) but can be used to link dikes to crustal storage and transport. Any additional data could be added to the clustering algorithm for a higher dimension of clustering. However, our analysis suggests that clusters generally represent multiple generations of dikes aligned along narrow axes of activity. This interpretation of large CFB dike swarms provides supporting evidence for a trans-crustal, multi-magma reservoir magmatic architecture model for CFBs (Mittal & Richards, 2021b). The spatio-temporal patterns in dike swarms may reflect an integrated lifecycle rather than a single time snapshot of the magmatic system (B. Black et al., 2021).

4.7 Structure of Dike Swarms in Hough Space

A key motivating question for our work is whether LIP dikes are organized into coherent spatial patterns at a sub-swarm or swarm scale. Spatial structure of dike swarms provides important constraints on dike-stress field interactions and external drivers of dike emplacement. Magma chambers (Gudmundsson, 2006; Karlstrom, Dufek, & Manga, 2009), regional tectonic stress (Wadge, Biggs, Lloyd, & Kendall, 2016), and topography such as edifices (Roman & Jaupart, 2014) have been inferred based on mesoscale patterns in the dike swarms. We show that the Hough Transform can be a useful tool in evaluating a range of structures in both the segment and linked databases, providing a means to overcome often incomplete and discontinuous observations.

4.7.0.1 Synthetic Mesoscale Structures. We will first focus on two end members of mesoscale dike swarm structure: linear and centrally localized (Figures 24A and B respectively). Roughly these two regimes represent either a spatially consistent least principal stress axis, such as implied by tectonic extension (Wadge et al., 2016), or a radially symmetric stress field such as implied by a magma chamber, volcanic edifice, or mantle plume head (R. Ernst et al., 1995). Centrally localized swarms can include both radial and circumferential swarms. These two end members can coexist spatially if the stress field changes with time. Of the two, radial swarms are more challenging to robustly identify in Cartesian space because apparent radial structure can arise from multiple misaligned linear swarms (Fig. 24B for example). These two end members are more easily identified in the Hough space where a linear swarm is represented by a vertical bar of points (Fig. 24a) and a radial swarm can be seen as a sinusoidal curve spanning a sufficiently large range of angles. This is illustrated in Fig. 24b,c, with synthetic line segment distributions. We also show some more complex swarm shapes and the associated difference in Hough Transform space shapes (Fig. 24d,e,f). The synthetics illustrate that Hough Transform space is very useful to distinguish amongst different kinds of dike mesoscale structure, although we focus only on end member patterns here.

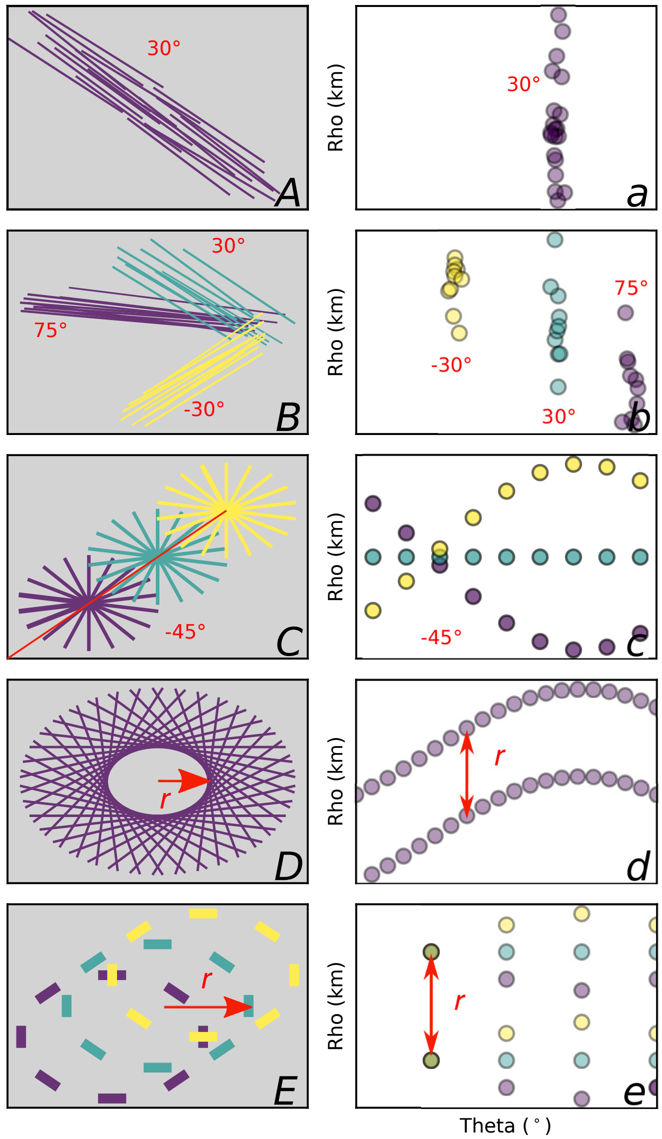

Figure 24. Synthetic dike swarms in a Cartesian space (gray background, uppercase label) and Hough Transform space (white background, lowercase label). **A.** shows as simple linear swarm oriented at 30°. **B.** shows three linear swarms at −30°, 30°, 75°. **C.** shows three radial swarms aligned at a −45° angle. The angle at which radial swarms intersect in the Hough Space is the angle of their relative orientation in Cartesian space. **D.** shows a circumferential swarm with the lines extending to show how it converges to Eq. 8. The radius of the circumferential swarm is equal to the spaceing of the parallel two curves in Hough Space. **E.** shows three circumferential swarms with the same radius aligned at −45° angle.

We use several criteria to distinguish ideal radial dike patterns from other structures. First, we require that a radial dike distribution has a range of constituent angles. Secondly, we assume that the structure has a small common area of dike intersection for interpreting this pattern as arising from a common magma source. To identify radial dikes, we return to the formulation of the Hough Transform in Eq. 4.1 and find an equation for a perfectly intersecting radial distribution of segments

$$\rho_r(\theta) = (x_r - x_c)\cos(\theta) + (x_r - y_c)\sin(\theta). \tag{4.8}$$

where x_r and y_r are the Cartesian location of the radial center adjusted by the chosen origin of the HT (x_c, y_c). Using Eq. 4.8 we can fit data in the Hough Transform space and find (x_r, y_r) a non-linear least squares to fit as implemented in Scipy Optimize library (Virtanen et al., 2020). We can then pick any line which falls within $\rho_r(\theta) - R_{max} < \rho(\theta) < \rho_r(\theta) + R_{max}$ which effectively draws a circle with radius R_{max} around the points (x_r, y_r) in cartesian space and an envelope of half-width R_{max} around the line calculated in Eq. 4.8.

Similar to ideal radial swarms, circumferential swarms form sinusoidal waves across Hough space with the center of the swarm described by Eq. 4.8 (Fig. 24D and E for example). However, in the case of a circumferential swarm there are two distinct and parallel sinusoidal waves at $\pm r$ where r is the radius of the circumferential swarm. To see why this is the case we show in Figure 24D that extending the lines of a circumferential swarm makes it appear similar to a radial swarm but without a point of intersection at the middle. Note again that the Hough transform does not include information about where the segments falls on the infinite line which would differentiate the radial and circumferential swarms. The two trends seen in the circumferential case are seperated by the radius of the swarm. Like the radial swarm, changing the center of the swarm changes the represenation in hough space as does changing the radius. For the circumferential swarm both the center and the radius has an effect on the hough space representation whereas only the center effects a radial swarms representation (Fig 24E). For both types of centrally localized swarms the center can be found in the Hough space by fitting Eq. 4.8 to the data. In the Hough space for a dataset with limited or sparse segments, it may be difficult to distinguish radial from circumferential swarms. However once the sinusoid is identified and fitted it can be inspected in Cartesian coordinates to determine which end member is appropriate. An advantage of using the Hough Space is that it allows the observer to isolate structures of certain orientations, and then inspect them for interpretation in Cartesian coordinates. By combining both parameter spaces, we can better understand complex overlapping patterns in the dike swarm and quantify the meso-scale structure.

Limitations of this method arise when the space over which line segments are spread is very great. Analysis of synthetic tests of radial swarms indicates that it is difficult to distinguish radial structures with centers whose distance in Cartesian coordinates is more than 2x the standard deviation of ρ from the HT origin. To account for this after fitting a radial swarm to the data one must both inspect it in Cartesian space and then recenter the HT on the radial center and run the fit again or cut the data into smaller sections to account for distortion.

4.7.0.2 Method Application to Spanish Peaks. To evaluate mesoscale structures in the Hough Transform space, we use the Spanish Peaks dataset as a clear example of diverse structures. The two radial structures and linear dikes overlap in Cartesian space but form distinct bands in Hough space (Figure 4.8). We apply the radial swarm equation to the Spanish Peaks dataset to find the center of the radial structures. First, we segment the data using Northing value of the segment midpoint into two sections ($Y > 4520000m$ and $4480000m < Y < 4520000m$) then fit Eq. 4.8 with a radius (R_{max}) of 2.5 km (See Figure 25a,b). We find two radial centers, one centered on West Peak (green, $R^2 = 0.75$) and another centered on Dike Mountain (purple, $R^2 = 0.93$). The distributions of angles in the radial swarm are mostly flat indicating even angular spacing except for slight increases around $-55° - 90°$ where some of the linear swarm dikes intersect with the radial swarm. For these specific dikes, it is ambiguous whether they should be counted as radial or linear. More data such as geochemistry or radiometric dating could help differentiate them.

4.8 What Multiscale structure exists in the CFB datasets?

4.8.1 Radial and Circumferential Patterns. The Hough Transform based analysis can be used to quantitatively test the dike meso-structure. Applying the methodology described above to find radial structures in the larger CFB datasets, we first attempt to fit the entire datasets for CRB and DT respectively to Eq. 4.8 to find a common origin for the entire datasets. This provides a quantitative way to evaluate whether a single radial center fits the datasets, as has been suggested to result from impingement of an idealized radial plume head on the lithosphere (Buchan & Ernst, 2021b; R. Ernst et al., 1995). For both the CRBG and DT segment datasets (or linked datasets), we do not find a well fit radial center for the entirety of the dataset ($R^2 = 0.005$ and 0.03 for CRBG and Deccan respectively, see Table 2). Thus, dike patterns, using a much larger dataset than previous work, do not support a model wherein either

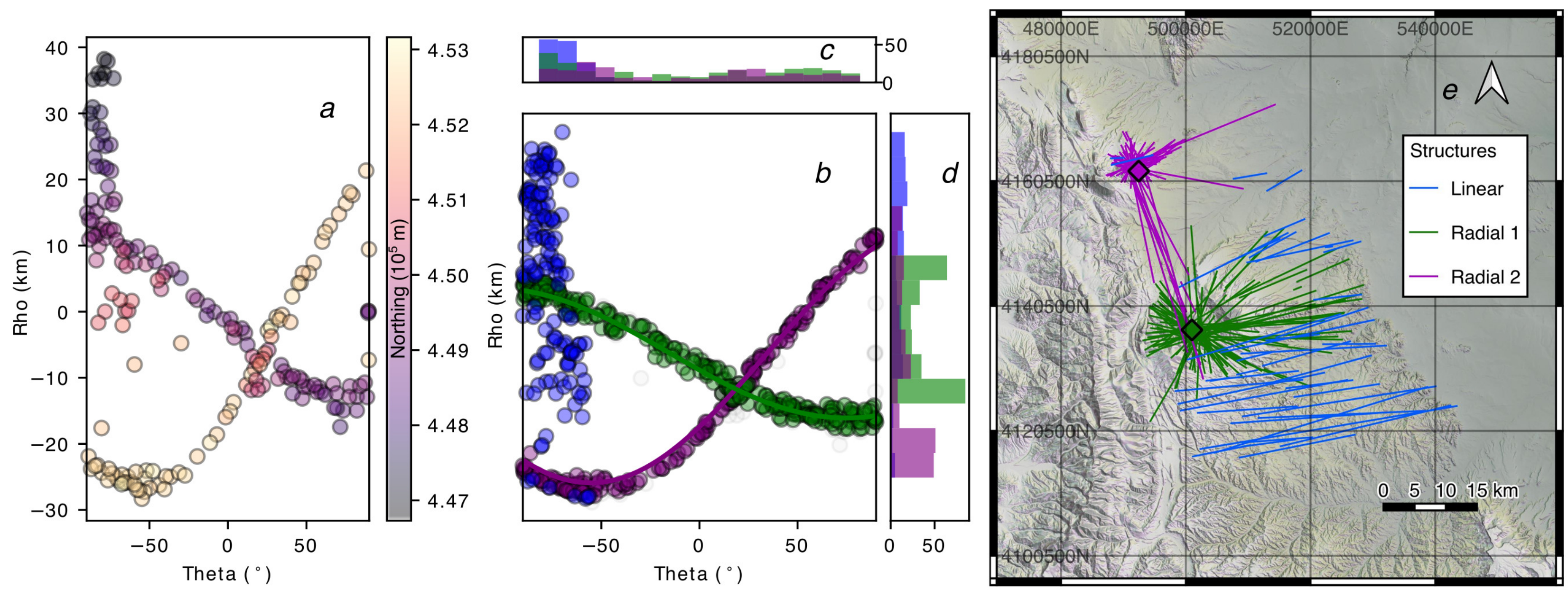

Figure 25. Analysis of the Spanish Peaks dataset. **A.** Hough Space colored by the segment midpoint Northing. **B.** Radial fits using Equation 4.8 and the segments which intersect within 2500 km of the centers and the remaining linear structure in blue. **C.** and **D.** show the distribution of θ and ρ respectively for the linear, and two radial structures. **E.** Clustered lines for the three identified structures in Cartesian coordinates. This figure can be replicated using the demo file in our linked Github repository.

an axisymmetric plume head or a single large magma reservoir controls the dike pattern. Likewise, a large circumferential swarm would show clearly in the data as two parallel sinusoids of $\approx 100 - 300$ km apart. We do not observe these structures with our current data.

However, looking at subsets of the data sets, filtered based on segment midpoint Northing, we do find mesoscale radial patterns in both CFBs wherein all the dikes have intersections within a radius (R_{max}) of 10 km. In the CRBG datasets, we find two candidate radial patterns – one centered in the Wallowa mountains region at (469438E, 5001913N - UTM Zone 11N, EPSG 26911 projection) and a second radial center south of the highest density of dike exposure in the CJDS (472343E, 4933589N). This second potential center (red in Figure 9e) lies the within proposed centralized magma storage of (Wolff, Ramos, Hart, Patterson, & Brandon, 2008b). In the CRBG, the magma chamber south of the Wallowa mountains has been proposed by previous studies based on a geochemical analysis (Wolff et al., 2008b). This potential magma source could explain the southern-most radial center found via the Hough Transform and aligns roughly with the inferred centroid of dilation in Figure 23. However, the goodness of fit for these structures is however low ($R_{sq} = 0.26, 0.15$ respectively). A more complex HS pattern may provide a better fit to the dike segment distribution but it's unclear what these complex patterns might mean for the stress conditions. Further work could be done to incorporate HS patterns and crustal stress modeling. We cannot rule out the possibility that apparent radial patterns in the CJDS simply arise from overlapping linear features with variable orientation. We believe that these apparent radial dike patterns in both CFBs warrant further study. However, the robustness of this structure is not very significant.

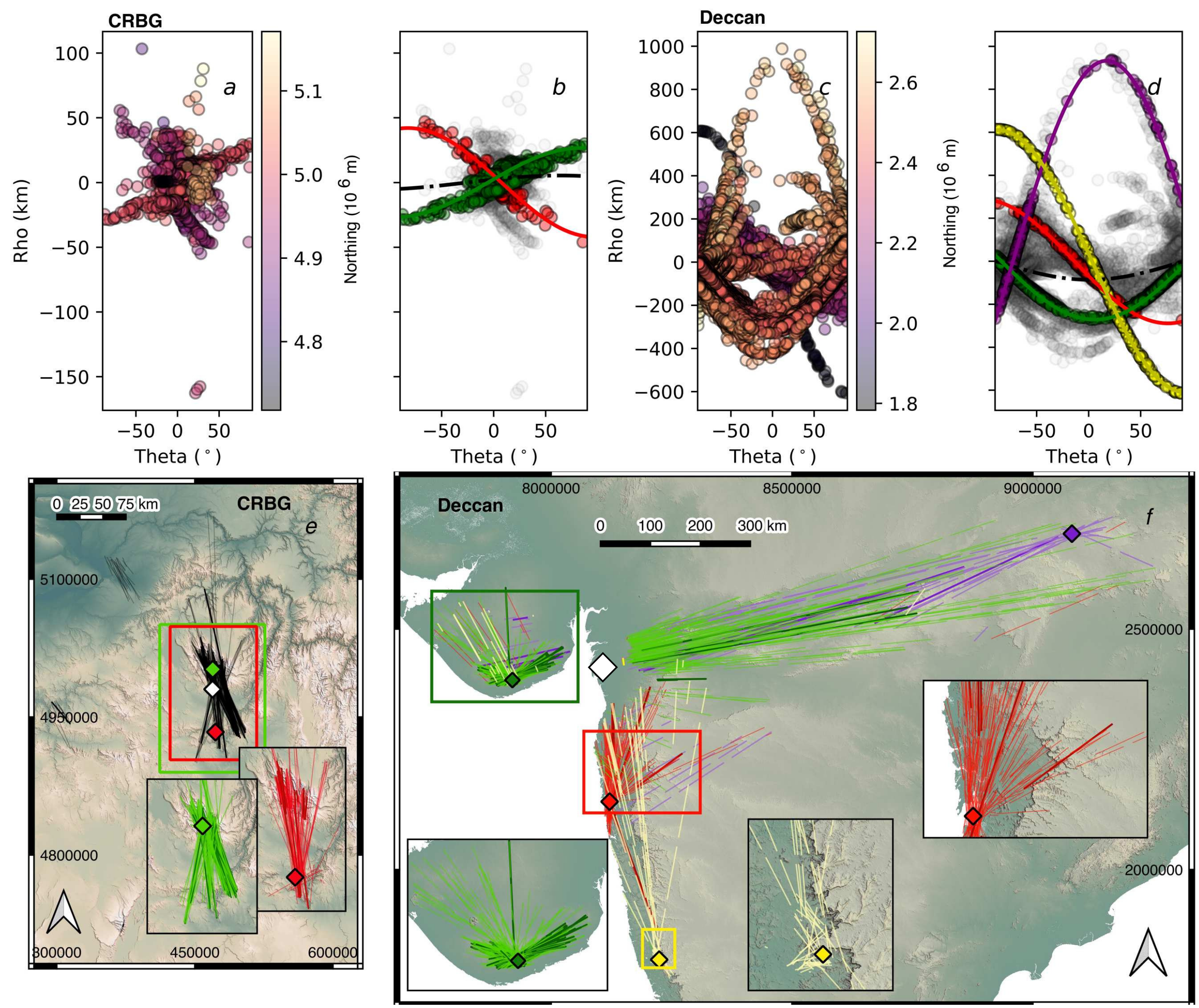

Figure 26. **A.** and **C.** show the Hough Space colored by the cluster midpoint Northing for the CRBG and Deccan respectively. **B.** and **D.** show possible radial fits using Equation 4.8. **E.** and **F.** show all clusters which fall within a 10 km radius of each radial center while the bold lines show the filtered lines which fall within this radius. White diamonds show in **E.** and **F.** show the locations of the best fit radial center for the whole dataset. Zoomed in panels of each inset with the radial centers and segments that fit them can be found in Kubo Hutchison et al. (2023) Exact locations of centers available in Table 2.

In the Deccan database, we find several possible radial structures with significantly better goodness of fits than what is seen in the CRBG. Firstly, we find a center (Figure 9f, green) centered in the Saurashtra subswarm (7919544E, 2394058N - Pseudo-Mercator, EPSG 3857) with goodness of fit of $R_{sq} = 0.91$ and 3600 dikes which intersect with this proposed center. Notably, this structure extends well into the Narmada-Tapi rift zone which is strongly linear and is 100s of kilometers away. The fits do not account for Cartesian endpoints of the segments or clusters. The second best fit center is centered near Mumbai at 8121286E, 2141444N (Figure 26, red) with goodness of fit of $R_{sq} = 0.81$. We show two other possible centers (Figure 26, purple and yellow) with high goodness of fit ($R_{sq} = 0.97$ and 0.99). However due their large distance from the Hough Transform origin of the dataset, we are unsure whether these swarms associations are physical (Figure 9f yellow inset). Looking at them in the Cartesian space, they do not appear as radiating fans which leads us to think that these linkages may be artifacts of Hough Transform distortion which occur due to the extremely large area over which the Hough Transform is taking place.Although the radial structures are more clear for the Deccan Traps, there is no clear geological or geophysical evidence of a localized magma reservoir associated with the center of the radial dike swarms to date (Dole, Das, & Kale, 2022; Rajaram, Anand, Erram, & Shinde, 2017; Rao, Ravikumar, & Golani, 2022; Self, Mittal, Dole, & Vanderkluysen, 2022). The radial patterns we observe may instead represent a time evolving stress state in which successive linear trends are emplaced with changes in angle such as in Fig 24B . Additional data is necessary to evaluate and assign physical interpretation to these structures. Our results thus provide useful targets for future targeted work that can help address important questions related to the magmatic architecture of CFBs.

4.8.2 Linear Trends.

We consider a linear swarm to be defined by a set of subparallel dikes oriented along an axis. A linear swarm has a length and width in Cartesian space that correspond to a range of angles and ρs in Hough Space. A narrow range in angles is essential. To identify orientations with linear activity we examine the histogram of the Hough Space and look for concentrations of dikes within narrow bins of θ and ρ in a method analogous to the traditional use of the Hough Transform accumulator array (Figure 27). Looking at the bins with the highest counts, we can establish packets of linearly oriented dikes. The top three bins of the Hough Transform histogram for CRBG and Deccan represent 11% and 12% of all segments respectively. In the CRBG, this represents a range of only 14° and each bin is adjacent to the others since it is strongly linear. In the Deccan, the top three bins represent a range of 21°.

In the Deccan, the major linear trends are in the Narmada-Tapi rift zone between $-85°$ and $-65°$ and extend for well over 100 km and slightly into the Saurashtra region (Figure 27d). These overlap with the radial swarms found above and can also be part of the radial swarm fits. The identification of dikes as being part of both a linear and radial structure gives interesting information about the structure. This may be indicative of the fact that the presence of a slowly rotating stress field leads to the formation of multiple linear type structures. These in turn overlap and forming a fanning structure (similar to what is shown in Figure B) rather than a true radial structure. In CRBG, we find two subparallel axes of linear dikes structure with high dike concentrations. These structures connect areas of high dike density which appear in the granites associated with the Wallowa mountains and isolated granite stocks to the south (Morriss et al., 2020; Petcovic & Grunder, 2003).

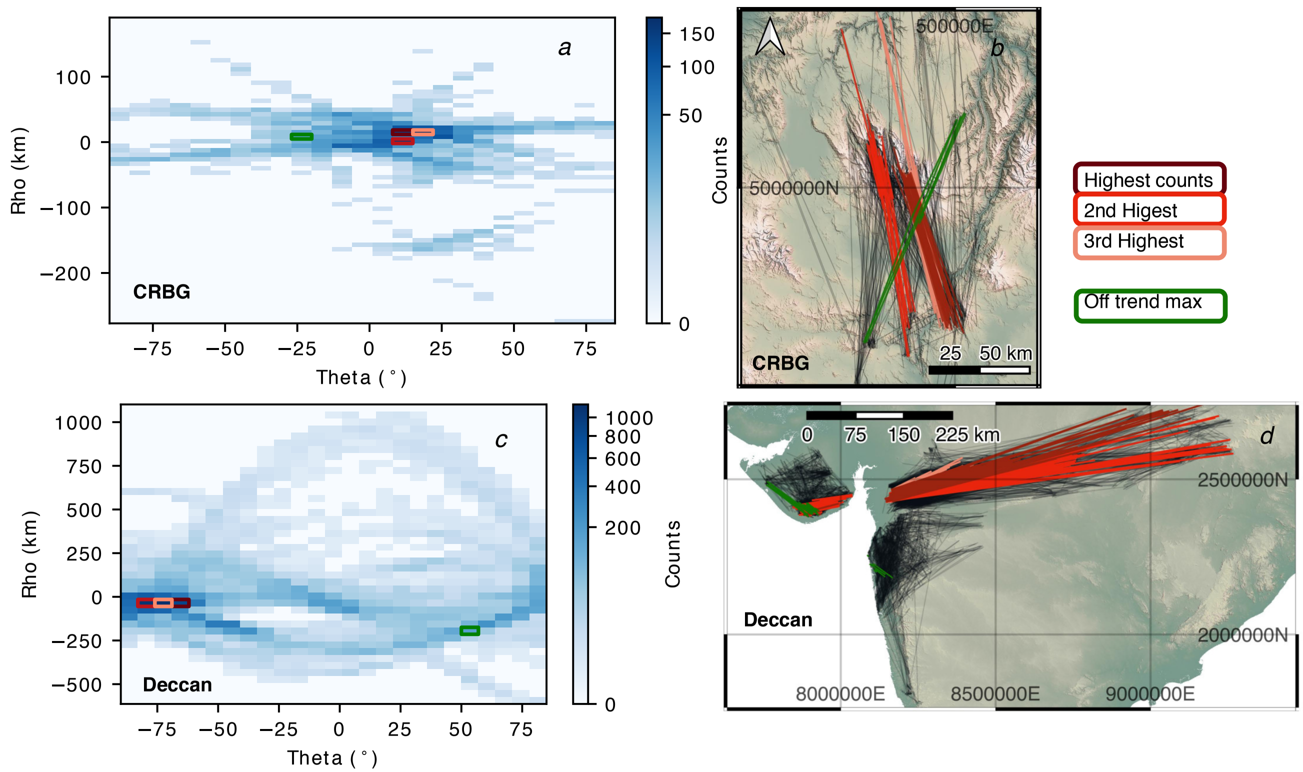

Figure 27. **A.** and **C.** show a histogram of the Hough transform segment database as a function of ρ and θ with dark blue colors indicating higher counts in that orientation. The bins of the histogram are set to be a width of 7° in angle and 2.5% of the range of ρ. **B.** and **D.** show the top three bins of the histogram (maroon, red, and pink) in Cartesian space along with an off-axis maximum shown in green. The off axis maximum is the highest bin more than 50° away from the main linear trend (red box). We use the segment orientations for the histograms but show the linked dikes for ease of viewing.

4.9 Comparing Deccan and Columbia River Flood Basalts

The Deccan Traps erupted volume is at least $6x$ greater than the CRBG in eruptive volume ($1,300,000$ km^3 vs $210,000$ km^3, Figure 28A) (Jay & Widdowson, 2008; Kasbohm & Schoene, 2018). Is this volumetric difference in erupted volume reflected in the shallow crustal dike swarm exposures? Most magma never erupts at the surface, so directly linking exposed dikes to eruptive volume in general is difficult (Gudmundsson, 2002; Townsend & Huber, 2020). Nevertheless, the large scale of upper crustal dike swarms as analyzed in this study provides a unique opportunity for comparison. Firstly, the Deccan dike segment database ($n = 25,938$) is larger than the CRBG ($n = 4340$) by a factor of 5.9, similar to the erupted volume ratio. Although there are significantly different observational biases, especially due to different exposures, in the CRBG and DT datasets we do posit that the difference in dike segment numbers scales with the erupted volume. In the unfiltered clustered database the ratio (DT to CRBG) is also approximately maintained at $5.2x$. The filtered database ratio is $13x$, but is less directly comparable due to the different ρ threshold for the Deccan swarm.

The median length of Deccan clusters as shown by the Hough Transform ($\sim$ 93 km) is significantly longer ($3x$) than the CRBG clusters ($\sim$ 29 km). Comparing the ratio of eruptive volume to median length we see similar ratios of 11 and 7 sauare kilometers. The median width of Deccan clusters ($\sim$ 2 km) is larger than the CRBG clusters ($\sim$ 0.7 km). Although this difference might be attributed to the ρ thresholds based on segment mean length between the CFBs, we note that similar widths arise if a comparable ρ threshold had been used for the CRBG. The median cluster aspect ratios are similar 53 vs 48 for the Deccan and CRBG respectively (Figure 28D). The similar cluster aspect ratios implies that the

H

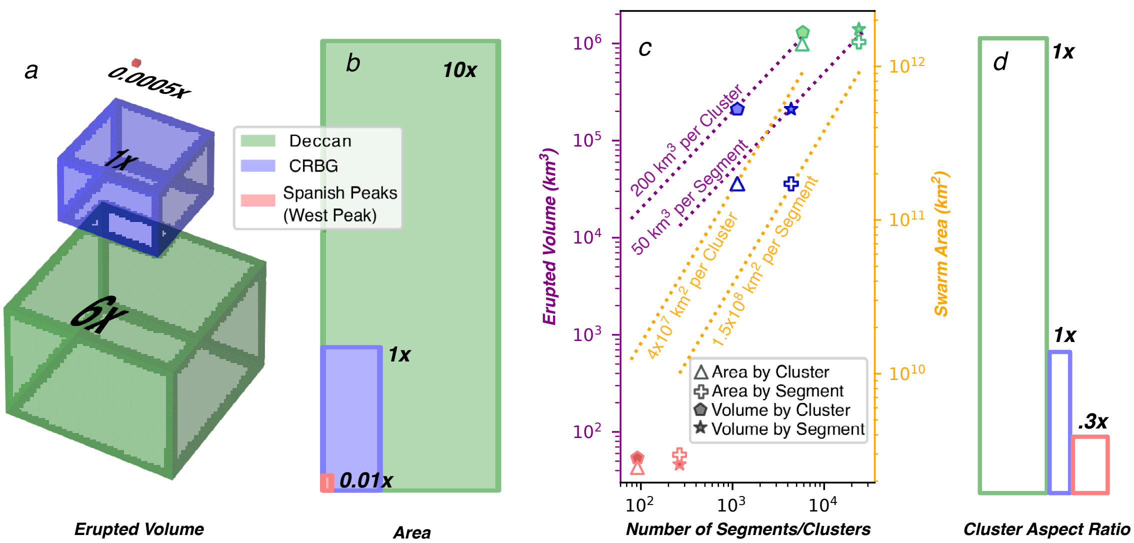

Figure 28. **A.** comparison of the erupted volume of Deccan Traps, CRBG, and Spanish Peaks specifically the West Peak on which the radial swarm is centered (Jay & Widdowson, 2008; Kasbohm & Schoene, 2018; Reidel, Camp, Tolan, & Martin, 2013). Since there are no extrusive deposits associated with Spanish Peaks, the West Peak erupted volume is estimated based on (Grosse et al., 2020) assuming an intrusive extrusive ratio of at least 1:2 and is used as a rough example of one eruptive center. **B.** compares the swarm areas. **C.** plots the number of dikes or clusters versus the erupted volume (left, purple, filled symbols) and the swarm area (right, orange, white symbols) for the three dike swarms. We have also plotted estimated lines of the erupted volume and area per segment and cluster which is roughly constant for the limited data. **D.** shows the relative dike cluster widths and lengths and is annotated with the ratios of dike cluster aspects which again are roughly constant for the three examples.

dike emplacement mechanics are the same for both swarms despite the significantly longer clustered dikes in the Deccan. Individual dike aspect ratios are predicted using LEFM however what we show are dike clusters also show similar aspect ratios implying that dike swarming mechanisms in both systems are similar. This could support the idea that the eruptions are fed by distributed magma reservoirs. Finally, the amount of estimated maximum dilational strain is similar for both swarms despite their difference in spatial area.

Together, these similarities between clustered dike segments, in the context of erupted volume ratios between CRBG and Deccan, suggest that spatial patterns of CFB magmatic geometry scales with total eruptive output. Such structural similarities, measured both on province scale and via dike cluster sizes, are remarkable. Although two examples is hardly a robust trend, the implications are interesting and unexpected given significant differences in other aspects of the CFBs. We can also roughly extend this to the Spanish Peaks although the different geologic setting and unknown volumes make direct comparisons difficult. We use the swarm centered on West Peak, which may represent the scale of a typical long-lived volcanic center and paleo-edifice (Harp, 2021), to examine the scaling between area and number of dikes to CFBs. We use an estimated "erupted" volume for West Peak based on averages of volcanic complexes compiled in O'Hara et al. (2020) and Grosse, van Wyk de Vries, Petrinovic, Euillades, and Alvarado (2009). Extending the scaling trend to West Peak over estimates the erupted volume and area by up to two orders of magnitude however the comparison between the West Peak an the voluminous LIP datasets is difficult to make especially considering the high uncertainty on the West Peak eruptive system.

If erupted volumes are imprinted on the spatial structure of the transcrustal magma transport system, this scaling provides a tool for connecting surface volcanic expression to deep transport that is hidden from view. Conversely, it is also of interest to connect exhumed transport systems such as Spanish Peaks, plutonic systems (Karlstrom et al., 2017), and ancient dike swarms (Baragar et al., 1996; Fahrig & Jones, 1969), or planetary examples (R. Ernst et al., 1995), to their surface expressions.

4.10 Conclusion

We have developed a tool based on the Hough Transform for objective extraction of structures in complex distributions of quasi-linear segments, such as are prevalent in terrestrial dike swarms. We have tested this tool with synthetic data and applied it to three dike swarms, associated with the Spanish Peaks, Colorado, USA, the Columbia River Flood Basalts, USA, and the Deccan Traps, India. We found that dike segments can be linked together into aligned structures that may represent dikes or packets of highly clustered dikes. Looking at the linked datasets we find significantly longer sustained structures which average 30 km in CFBs and can reach over 200 km. The Hough Transform also facilitates investigation of dike swarm mesoscale structure in two end members: linear and radial patterns. Firstly, we do not find that a single radial or circumferential center is well fit by the dike data in any of the three provinces. However, we do find that the dike swarms can be decomposed into smaller localized radial patterns which may represent rotating stress fields over time or the influence of an isotropic stress field.

For CFBs, the apparent generality of structures and scaling provide a template for future study both of the CRBG and Deccan as well as other flood basalt systems. We expect that future work incorporating compositions (Reidel, Camp, Tolan, & Martin, 2013), paleomagnetic polarity (Biasi & Karlstrom, 2021), and direct geochronology (Fendley et al., 2019b; Kasbohm & Schoene, 2018; Schoene, Eddy, Keller, & Samperton, 2021; H. Sheth, Vanderkluysen, Demonterova, Ivanov, & Savatenkov, 2019) will be necessary to robustly link individual segments together. Additional statistical characterization, such as analysis of the dendrogram generated via the hierarchical clustering methods (Jarman, 2020), could seek to establish the range of mesoscale structures that exist. Additionally, the Hough transform method could be generalized to include curvilinear segments, which are not uncommon in dike swarms but neglected here for simplicity. This method as described here which we applied to dike swarms could also be applied to many types of linear/curved structures including fracture sets, fault networks, and shear zones on Earth or on other planets.

CHAPTER V

CHAPTER 5: LINKINGLINES: USING THE HOUGH TRANSFORM TO CLUSTER LINE SEGMENTS AND MESOSCALE FEATURE EXTRACTION

This chapter was previous published in Hutchison et al., (2024). LinkingLines: Using the Hough Transform to Cluster Line Segments and Mesoscale Feature Extraction. Journal of Open Source Software, 9(98), 6147, https://doi.org/10.21105/joss.06147.

5.1 JOSS Paper

5.1.1 Summary.

Linear feature analysis plays a fundamental role in various scientific and geospatial applications, from detecting infrastructure networks to characterizing geological formations. In this paper, we introduce `linkinglines`, an open-source Python package tailored for the clustering, and feature extraction of linear structures in geospatial data. Our package leverages the Hough Transform, commonly used in image processing, performs clustering of line segments in the Hough Space then provides unique feature extraction methods and visualization. `linkinglines` empowers researchers, data scientists, and analysts across diverse domains to efficiently process, understand, and extract valuable insights from linear features, contributing to more informed decision-making and enhanced data-driven exploration. We have used `linkinglines` to map dike swarms with thousands of segments associated with Large Igneous Provinces in (Kubo Hutchison et al., 2023).

5.1.2 Statement of Need.

The `linkinglines` Python package addresses the need for quantitative and automated line clustering and analysis in geologic data. As the volume of data continues to grow, including remote sensing, computer vision, and geographic information systems (GIS), there is an increasing demand for tools that can simplify the extraction and analysis of linear features such as dikes, fractures, roads, lineaments.

The primary needs that the `linkinglines` package fulfills include:

1. Dissected Line Extraction or Data Reduction: In areas where land cover or data availability affects the complete mapping of linear features, this package can link together similarly oriented segments into lines in a quantitative automated way. This is also an data reduction technique.

2. Feature Extraction and Analysis: The `linkinglines` package provides functions to extract and then compute essential metrics and statistics on extracted linear, radial or circumferential type features which are commonly seen in dike swarms or fracture networks.

3. Geospatial data often involves complex relationships between various linear features. `linkinglines` integrates seamlessly with popular geospatial libraries like `pyproj` and `geopandas` to facilitate georeferenced data analysis and visualization.

4. Custom Plotting and Visualization: Effective visualization is critical for data interpretation. The package offers custom plotting scripts, making it easier to visualize results and communicate findings.

5.1.2.1 Statement of the Field. This package was originally developed to tackle the issue of mapping dike segments. Rugged terrain, vegetation cover, and a large area made it impossible to accurately map dikes. The length, density, and structure of the dike swarm affects how magma is transported and erupted. Scaling analysis indicated that for segments of widths of 10 m, dikes could be 10s to 100s of kilometers long; however observed segments were two orders of magnitude lower (Morriss et al., 2020). Additionally, the complex overlapping structure of the dike swarm was difficult to analyze. We designed `linkinglines` to extract not only lines from line segments but also help analyze the mesoscale structure of the dike swarm. Using the unique properties of the Hough Transform we can extract several unique mesoscale structures within a group of lines.

Issues with data coverage, incompleteness, and complexity occur in a wide range of Earth and Planetary science data products. As an example we show how this work can also be applied to lineaments on Venus and fracture networks in our documentation. Clustering and machine learning methods are commonly applied geosciences within the subdisciplines of seismology, geochemistry, and planetary science. There is currently available code to work with geospatial data clustering such as `geopandas` , `PySAL` , and others which perform the Hough Transform on images such as `scikit-image` or `OpenCV` , however this seems to be the first union of the two methods and specific to geoscience data applications. There is a clear use case for `linkinglines` to be applied to planetary science and the variety of linear features on Venus and Mars. For example, `linkinglines` can be used to quantitatively identify the centers of radial lineaments on Venus and relate the data back to volcanism and plate tectonics, although work has been done to map and qualitatively characterize these features `linkinglines` offers unique insight and quantitative measure (R. Ernst et al., 1995). Related packages which are specific to geosciences such as `fractopo` which focuses on network analysis of fractures could be utilized in parallel with `linkinglines` for additional analysis (Ovaskainen, 2023).

5.1.3 Algorithm.

`linkinglines` can read in any common geospatial data format using `geopandas` such as ESRI Shapefiles, GeoJSON, or Well Known Text (Jordahl et al., 2020). Preprocessing is applied to the dataset so that only straight lines are considered in the algorithm. This is done by loading in the points from each vector object and performing linear regression, only considering those that yield a line with a $p > 0.05$. The data is then formatted into a `pandas DataFrame`. This package heavily uses `pandas` as the database structure for ease of use, data manipulation, and integration with `numpy` and `scipy` (pandas development team, 2020).

The Hough Transform is an image processing technique used for detecting straight lines and other patterns in binary or edge-detection images (Hough, 1962). It achieves this by converting points in an image into parametric equations and identifying patterns through the accumulation of votes in a parameter space. The transform has been generalized to detect arbitrary shapes, making it a versatile tool for pattern recognition and image analysis (Ballard, 1981). Applications of the Hough Transform include object or motion detection, lane tracking for cars, road detection in geospatial data, and biometric authentication (Mukhopadhyay & Chaudhuri, 2015). After loading in the data, it is assumed to be already line structures, so the accumulator array of the Hough Transform is skipped, although this functionality could be added if needed. First, the angle of the line segment is found. In many methods, it is the left-hand corner of the image (Ballard, 1981), but we choose the average midpoint of the line segments (Figure 1B). Other origins can be specified in certain functions using the `xc` and `yc` arguments. We use the ρ, θ parameterization of /citehough.

After the coordinate transform, ρ and θ become the basis for the Agglomerative clustering step, where we utilize Scipy's clustering algorithm (Virtanen et al., 2020). The clustering algorithm takes two inputs: `dtheta` and `drho`, which are used to scale the Hough Transform data. Then the clustering distance is set to 1. Combined with the default complete linkage scheme, effectively, this prevents clusters from being formed that have ranges greater than either `dtheta` or `drho` and the linear combination of the two where:

$$d = \sqrt{\left(\frac{\theta_1 - \theta_2}{d\theta}\right)^2 + \left(\frac{\rho_1 - \rho_2}{d\rho}\right)^2} \tag{3}$$

where two members of a potential cluster are denoted by the subscripts 1 and 2. Other linkage or distance schemes could be considered and implemented based on the specific research applications.

After labels are assigned in the clustering portion of the algorithm, new lines are drawn using the endpoints of the clustered lines (Figure 1D). For each cluster, the nearest neighbors of the segment midpoints are calculated in Cartesian space, allowing for an analysis of the Cartesian spatial clustering of the lines. We also introduce an optional filtering step, which analyzes the maximum nearest neighbor difference of midpoints normalized by the total cluster length. This filters out clusters with segments that are not evenly clustered in Cartesian space.

5.1.3.1 Feature Extraction. Additionally, we leverage the unique properties of the Hough Transform to combine clustering with feature extraction. In the original usage case of overlapping complex dike swarms, two potential end members of swarm types are linear and radial or circumferential swarms (Figure 4.8.2). We can easily derive equations to describe these Cartesian patterns in the Hough Space, then perform a best-fit analysis using `scipy`.

In the case of a radial or circumferential pattern, the equation is actually the Hough Transform equation where the radial values of ρ_r can be expressed as:

$$\rho_r(\theta) = (x_r - x_c)\cos(\theta) + (x_r - y_c)\sin(\theta) \tag{4}$$

where the radial form is a function of θ and the center of the radial form, a Cartesian location (x_r, y_r) (Figure 18). Armed with this equation, we can apply a best-fit analysis of the data to find quantitative center locations for radial or circumferential patterns (Figure 18D,E). In the application of dike data, this may point to a central magma chamber or locus of stress. We can also then remove the lines which fit those patterns for feature extraction.

For extraction of linear features there are two options, one is the clustering step described above, the second can be applied with looking for mesoscale (mid-scale) clusters, i.e. cluster of clusters. We apply the Hough accumulator array, a 2D histogram of θ and ρ. You can set the size of bins in the histogram and if clusters fall within those boxes they can be thought of as mesoscale clusters. We allow for flexibility of cutoffs for these mesoscale feature extraction, so it can be tailored to each research or engineering application.

Overall, these capabilities can be separated from the clustering and linking steps but is combined for ease of use in the `linkinglines` package.

5.1.4 Future Work.

This package takes geospatial or other types of line segment data and clusters them based on their orientation. Currently, the implementation only works with linear features however it could be generalized to arbitrary shapes for more flexibility (Ballard, 1981). Additionally, future work could incorporate other shapes or patterns in the Hough Space and could extend the feature extraction methods laid out here. We invite collaboration to increase the capabilities of this code.

5.1.5 Acknowledgments. This paper was made possible by the "Crafting Quality Research Software and Navigating Publication in Software Journals" held by the Computational Infrastructure for Geodynamics in September 2023.

CHAPTER VI

CHAPTER 6: CONCLUSION

In this dissertation, we have explored the complex multiscale interactions between volcanic phenomena and their implications for humans and the environment. Our research harnesses cutting-edge three-dimensional multiphase models and innovative image processing techniques to address key challenges in volcanic hazard prediction and geological exploration.

Firstly in **Chapter Two**, the study on PDCs highlights their sensitivity to topographic features and emphasizes the critical nature of channel geometry in influencing the behavior of these fast-moving, high-temperature flows. By examining the effects of channel width, depth, and curvature on the overspill of PDCs, we have identified significant risk factors that contribute to the hazardous spread of these currents beyond confined valleys. Our findings underscore the necessity of incorporating three-dimensional modeling into disaster management strategies to better predict and mitigate the impact of PDCs, especially in populated areas built on or near volcanic terrains. We found that the runup and supereleveation as the bed load traversed increased with the curvature of the channel up to a certain point. After that critical level, the momentum removal was great enough that overspill volume removal decreased. The effect of adding a particle phase in the PDC clearly causes large vertical heterogeneity in density, temperature, and velocity which interacts with the topography.

After the high Reynolds number models, we move to the low Reynolds number regime in the subsurface. In **Chapter Three**, we modeled the hydrothermal circulation around an intruded andescite. The integration of the Idaho National Lab's MOOSE framework into our study further enhances our ability to simulate the cooling processes in dikes, factoring in the significant role of hydrothermal systems. This advanced modeling provides a deeper understanding of the thermal dynamics at play, which is vital for assessing the long-term stability of these geological structures and their effects on the surrounding environment. Application of MOOSE to volcanology has so far been limited and this work represents a major step to future modeling work enabled by this framework.

After examining a single dike, we move to the analysis of swarms of dikes in the subsurface in **Chapter Four and Five**. Our analysis of dike swarms in the Columbia River Flood Basalts and the Deccan Traps has revealed complex spatial structures that challenge traditional interpretations of their formation. By applying the Hough Transform and leveraging our custom-developed software, `linkinglines`, we have demonstrated a more nuanced method for understanding the intricate patterns of these magmatic features. This approach not only improves our geological mapping capabilities but also enriches our understanding of the processes that drive large igneous provinces and their associated climatic and ecological disruptions.

Collectively, the research presented in this dissertation not only advances our scientific knowledge in volcanic and geological studies but also offers practical tools and methodologies for modeling and mapping. The implications of this work are broad, impacting fields ranging from disaster readiness to environmental conservation and urban planning. Through a blend of sophisticated modeling techniques and analytical rigor, we contribute to safer, more informed interactions with our dynamic planet.

REFERENCES CITED

Abbey, A. L., Randolph-Flagg, N., Villa, K. d., Kim, S. L., & Shuster, D. L. (2024, February). Tracing short-lived hydrothermal circulation systems and water–rock interactions around small-scale intrusions. *Geochimica et Cosmochimica Acta*, *366*, 113–127. Retrieved 2024-05-30, from `https://www.sciencedirect.com/science/article/pii/S001670372300618X` doi: 10.1016/j.gca.2023.12.009

Acocella, V., & Neri, M. (2009). Dike propagation in volcanic edifices: Overview and possible developments. *Tectonophysics*, *471*(1-2), 67–77. doi: 10.1016/j.tecto.2008.10.002

Albino, F., Biggs, J., Escobar-Wolf, R., Naismith, A., Watson, M., Phillips, J. C., & Chigna Marroquin, G. A. (2020, November). Using TanDEM-X to measure pyroclastic flow source location, thickness and volume: Application to the 3rd June 2018 eruption of Fuego volcano, Guatemala. *Journal of Volcanology and Geothermal Research*, *406*, 107063. (Publisher: Elsevier B.V.) doi: 10.1016/j.jvolgeores.2020.107063

Andrews, B. J. (2014, September). Dispersal and air entrainment in unconfined dilute pyroclastic density currents. *Bulletin of Volcanology*, *76*(9), 1–14. Retrieved 2019-06-12, from `http://link.springer.com/10.1007/s00445-014-0852-4` (Publisher: Springer Berlin Heidelberg) doi: 10.1007/s00445-014-0852-4

Andrews, B. J., & Manga, M. (2012a). Counterintuitive effects of substrate roughness on PDCs. *AGU Fall Meeting*, *2012*, V11B–2753.

Andrews, B. J., & Manga, M. (2012b). Experimental study of turbulence, sedimentation, and coignimbrite mass partitioning in dilute pyroclastic density currents. *Journal of Volcanology and Geothermal Research*, *225-226*, 30–44. Retrieved from `http://dx.doi.org/10.1016/j.jvolgeores.2012.02.011` (Publisher: Elsevier B.V. ISBN: 0001-5563 (Print) 0001-5563 (Linking)) doi: 10.1016/j.jvolgeores.2012.02.011

Aramaki, S., & Akimoto, S. (1957, November). Temperature estimation of pyroclastic deposits by natural remanent magnetism. *American Journal of Science*, *255*(9), 619–627. (Publisher: American Journal of Science (AJS)) doi: 10.2475/ajs.255.9.619

Aravena, A., Cioni, R., Bevilacqua, A., de' Michieli Vitturi, M., Esposti Ongaro, T., & Neri, A. (2020). Tree-Branching-Based Enhancement of Kinetic Energy Models for Reproducing Channelization Processes of Pyroclastic Density Currents. *Journal of Geophysical Research: Solid Earth*, *125*(7), 1–20. doi: 10.1029/2019JB019271

Ayele, A., Jacques, E., Kassim, M., Kidane, T., Omar, A., Tait, S., ... King, G. (2007). The volcano-seismic crisis in Afar, Ethiopia, starting September 2005. *Earth and Planetary Science Letters*, *255*(1-2), 177–187. doi: 10.1016/j.epsl.2006.12.014

Babiker, M., & Gudmundsson, A. (2004). Geometry, structure and emplacement of mafic dykes in the Red Sea Hills, Sudan. *Journal of African Earth Sciences*, *38*(3), 279–292. doi: 10.1016/j.jafrearsci.2004.01.003

Balay: PETSc users manual - Google Scholar. (n.d.). Retrieved 2024-03-27, from `https://scholar.google.com/scholar_lookup?title=PETSc%20users%20manual%3A%20Technical%20report%2C%20ANL-9511%20-%20Revision%203.11&publication_year=2019&author=S.%20Balay&author=S.%20Abhyankar&author=M.F.%20Adams&author=J.%20Brown&author=P.%20Brune&author=K.%20Buschelman`

Ballard, D. (1981, January). Generalizing the Hough transform to detect arbitrary shapes. *Pattern Recognition*, *13*(2), 111–122. Retrieved 2024-06-11, from `https://linkinghub.elsevier.com/retrieve/pii/0031320381900091` doi: 10.1016/0031-3203(81)90009-1

Baragar, W. R., Ernst, R. E., Hulbert, L., & Peterson, T. (1996). Longitudinal petrochemical variation in the Mackenzie dyke swarm, Northwestern Canadian shield. *Journal of Petrology*, *37*(2), 317–359. doi: 10.1093/petrology/37.2.317

Baxter, P. J. (1990, September). Medical effects of volcanic eruptions - I. Main causes of death and injury. *Bulletin of Volcanology*, *52*(7), 532–544. (Publisher: Springer-Verlag) doi: 10.1007/BF00301534

Baxter, P. J., Boyle, R., Cole, P., Neri, A., Spence, R., & Zuccaro, G. (2005, April). The impacts of pyroclastic surges on buildings at the eruption of Soufriere Hills volcano, Montserrat. *Bulletin of Volcanology*, *67*(4), 292–313. Retrieved 2020-07-02, from `https://link.springer.com/article/10.1007/s00445-004-0365-7` (Publisher: Springer ISBN: 0044500403657) doi: 10.1007/s00445-004-0365-7

Baxter, P. J., Jenkins, S., Seswandhana, R., Komorowski, J. C., Dunn, K., Purser, D., ... Shelley, I. (2017). Human survival in volcanic eruptions: Thermal injuries in pyroclastic surges, their causes, prognosis and emergency management. *Burns*. doi: 10.1016/j.burns.2017.01.025

Benage, M. C., Dufek, J., Degruyter, W., Geist, D., Harpp, K., & Rader, E. (2014). Tying textures of breadcrust bombs to their transport regime and cooling history. *Journal of Volcanology and Geothermal Research*, *274*, 92–107. Retrieved from `http://dx.doi.org/10.1016/j.jvolgeores.2014.02.005` (Publisher: Elsevier B.V.) doi: 10.1016/j.jvolgeores.2014.02.005

Bernard, J., Kelfoun, K., Le Pennec, J. L., & Vallejo Vargas, S. (2014, September). Pyroclastic flow erosion and bulking processes: comparing field-based vs. modeling results at Tungurahua volcano, Ecuador. *Bulletin of Volcanology*, *76*(9), 1–16. (Publisher: Springer Verlag) doi: 10.1007/s00445-014-0858-y

Bhattacharji, S., Chatterjee, N., Wampler, J. M., Nayak, P. N., & Deshmukh, S. S. (1996). Indian intraplate and continental margin rifting, lithospheric extension, and mantle upwelling in deccan flood basalt volcanism near the K/T boundary: Evidence from mafic dike swarms. *Journal of Geology*, *104*(4), 379–398. doi: 10.1086/629835

Biasi, J., & Karlstrom, L. (2021). Timescales of magma transport in the Columbia River flood basalts, determined by paleomagnetic data. *Earth and Planetary Science Letters*, *576*, 117169. Retrieved from `https://doi.org/10.1016/j.epsl.2021.117169` (Publisher: Elsevier B.V.) doi: 10.1016/j.epsl.2021.117169

Bindeman, I. N., Greber, N. D., Melnik, O. E., Artyomova, A. S., Utkin, I. S., Karlstrom, L., & Colón, D. P. (2020). Pervasive Hydrothermal Events Associated with Large Igneous Provinces Documented by the Columbia River Basaltic Province. *Scientific Reports*, *10*(1), 1–9. (ISBN: 4159802067226) doi: 10.1038/s41598-020-67226-9

Black, B., Mittal, T., Lingo, F., Walowski, K., & Hernandez, A. (2021). Assessing the Environmental Consequences of the Generation and Alteration of Mafic Volcaniclastic Deposits During Large Igneous Province Emplacement. , 117–131. (ISBN: 9781119507444) doi: 10.1002/9781119507444.ch5

Black, B. A., Karlstrom, L., & Mather, T. A. (2021). The life cycle of large igneous provinces. *Nature Reviews Earth and Environment*, *2*(12), 840–857. (Publisher: Springer US ISBN: 0123456789) doi: 10.1038/s43017-021-00221-4

Blakely, R. J., Sherrod, B. L., Weaver, C. S., Wells, R. E., & Rohay, A. C. (2014, June). The Wallula fault and tectonic framework of south-central Washington, as interpreted from magnetic and gravity anomalies. *Tectonophysics*, *624-625*, 32–45. (Publisher: Elsevier) doi: 10.1016/j.tecto.2013.11.006

Bond, D. P. G., & Wignall, P. B. (2014). Large igneous provinces and mass extinctions: An update. *Special Paper of the Geological Society of America*, *505*(December 2015), 29–55. (ISBN: 9780813725055) doi: 10.1130/2014.2505(02)

Bourdier, J., & Abdurachman, E. (2001). Decoupling of small-volume pyroclastic flows and related hazards at Merapi volcano, Indonesia. *Bulletin of Volcanology*. doi: 10.1007/s004450100133

Brand, B. D., Gravley, D. M., Clarke, A. B., Lindsay, J. M., Bloomberg, S. H., Agustin-Flores, J., & Németh, K. (2014, April). A combined field and numerical approach to understanding dilute pyroclastic density current dynamics and hazard potential: Auckland Volcanic Field, New Zealand. *Journal of Volcanology and Geothermal Research*, *276*, 215–232. (Publisher: Elsevier) doi: 10.1016/j.jvolgeores.2014.01.008

Breard, E., & Lube, G. (2017, January). Inside pyroclastic density currents – uncovering the enigmatic flow structure and transport behaviour in large-scale experiments. *Earth and Planetary Science Letters*, *458*, 22–36. (Publisher: Elsevier B.V.) doi: 10.1016/j.epsl.2016.10.016

Breard, E., Lube, G., Jones, J. R., Dufek, J., Cronin, S. J., Valentine, G. A., & Moebis, A. (2016). Coupling of turbulent and non-turbulent flow regimes within pyroclastic density currents. *Nature Geoscience*, *9*(10), 767–771. Retrieved 2019-01-13, from `http://www.nature.com/articles/ngeo2794` (Publisher: Nature Publishing Group) doi: 10.1038/ngeo2794

Breard, E. C., Dufek, J., & Lube, G. (2018). Enhanced Mobility in Concentrated Pyroclastic Density Currents: An Examination of a Self-Fluidization Mechanism. *Geophysical Research Letters*. doi: 10.1002/2017GL075759

Breard, E. C., Dufek, J., & Roche, O. (2019). Continuum Modeling of Pressure - Balanced and Fluidized Granular Flows in 2 - D : Comparison With Glass Bead Experiments and Implications for Concentrated Pyroclastic Density Currents Journal of Geophysical Research : Solid Earth. , 5557–5583. doi: 10.1029/2018JB016874

Breard, E. C., Jones, J. R., Fullard, L., Lube, G., Davies, C., & Dufek, J. (2019, February). The Permeability of Volcanic Mixtures—Implications for Pyroclastic Currents. *Journal of Geophysical Research: Solid Earth*, *124*(2), 1343–1360. Retrieved 2019-05-13, from `https://onlinelibrary.wiley.com/doi/abs/10.1029/2018JB016544` doi: 10.1029/2018JB016544

Breard, E. C. P., Dufek, J., Charbonnier, S., Gueugneau, V., Giachetti, T., & Walsh, B. (2023, April). The fragmentation-induced fluidisation of pyroclastic density currents. *Nature Communications*, *14*, 2079. Retrieved 2024-03-26, from `https://www.ncbi.nlm.nih.gov/pmc/articles/PMC10097808/` doi: 10.1038/s41467-023-37867-1

Buchan, K. L., & Ernst, R. E. (2021a). Plumbing systems of large igneous provinces (LIPs) on Earth and Venus: Investigating the role of giant circumferential and radiating dyke swarms, coronae and novae, and mid-crustal intrusive complexes. *Gondwana Research*, *100*, 25–43. Retrieved from `https://linkinghub.elsevier.com/retrieve/pii/S1342937X21000757` (Publisher: Elsevier) doi: 10.1016/j.gr.2021.02.014

Buchan, K. L., & Ernst, R. E. (2021b, March). Plumbing systems of large igneous provinces (LIPs) on Earth and Venus: Investigating the role of giant circumferential and radiating dyke swarms, coronae and novae, and mid-crustal intrusive complexes. *Gondwana Research*, *100*, 25–43. Retrieved 2021-03-10, from `https://linkinghub.elsevier.com/retrieve/pii/S1342937X21000757` (Publisher: Elsevier) doi: 10.1016/j.gr.2021.02.014

Bunger, A. P., Menand, T., Cruden, A., Zhang, X., & Halls, H. (2013). Analytical predictions for a natural spacing within dyke swarms. *Earth and Planetary Science Letters*, *375*, 270–279. doi: 10.1016/j.epsl.2013.05.044

Bunger, A. P., Zhang, X., & Jeffrey, R. G. (2012). Parameters affecting the interaction among closely spaced hydraulic fractures. *SPE Journal*, *17*(1), 292–306. doi: 10.2118/140426-PA

Burgisser, A., & Bergantz, G. W. (2002). Reconciling pyroclastic flow and surge: The multiphase physics of pyroclastic density currents. *Earth and Planetary Science Letters*. (ISBN: 0012-821X) doi: 10.1016/S0012-821X(02)00789-6

Burgisser, A., Bergantz, G. W., Burgisser, A., Bergantz, G. W., Pyroclastic, R., & Physics, M. (2006). Reconciling Pyroclastic Flow and Surge : the Multiphase Physics of Pyroclastic Density Currents . To cite this version : HAL Id : hal-00022551 Reconciling Pyroclastic Flow and Surge : the Multiphase Physics of Pyroclastic Density Currents.

Bursik, M. I., & Woods, A. W. (1996). The dynamics and thermodynamics of large ash flows. *Bulletin of Volcanology*, *58*(2-3), 175–193. (ISBN: 0258-8900) doi: 10.1007/s004450050134

Cahoon, E. B., Streck, M. J., Koppers, A. A., & Miggins, D. P. (2020, April). Reshuffling the Columbia river basalt chronology-picture gorge basalt, the earliest-and longest-erupting formation. *Geology*, *48*(4), 348–352. Retrieved 2022-09-23, from `https://doi.org/10.1130/G47122.1` (Publisher: GeoScienceWorld) doi: 10.1130/G47122.1

Calder, E. S., Cole, P. D., Dade, W. B., Druitt, T. H., Hoblitt, R. P., Huppert, H. E., … Young, S. R. (1999, March). Mobility of pyroclastic flows and surges at the Soufriere Hills Volcano, Montserrat. *Geophysical Research Letters*, *26*(5), 537–540. Retrieved 2019-05-13, from `http://doi.wiley.com/10.1029/1999GL900051` (Publisher: John Wiley & Sons, Ltd ISBN: 0094-8276) doi: 10.1029/1999GL900051

Calder, E. S., Sparks, R. S., & Gardeweg, M. C. (2000, December). Erosion, transport and segregation of pumice and lithic clasts in pyroclastic flows inferred from ignimbrite at Lascar Volcano, Chile. *Journal of Volcanology and Geothermal Research*, *104*(1-4), 201–235. Retrieved 2019-01-13, from `https://www.sciencedirect.com/science/article/pii/S0377027300002079` (Publisher: Elsevier) doi: 10.1016/S0377-0273(00)00207-9

Calder, E. S., Sparks, R. S., & Woods, A. W. (1997). Dynamics of co-ignimbrite plumes generated from pyroclastic flows of Mount St. Helens (7 August 1980). *Bulletin of Volcanology*, *58*(6), 432–440. doi: 10.1007/s004450050151

Callot, J. P., Geoffroy, L., Aubourg, C., Pozzi, J. P., & Mege, D. (2001). Magma flow directions of shallow dykes from the East Greenland volcanic margin inferred from magnetic fabric studies. *Tectonophysics*, *335*(3-4), 313–329. doi: 10.1016/S0040-1951(01)00060-9

Camp, V., Reidel, S., Ross, M., Brown, R., & Self, S. (2017). Field-Trip Guide to the Vents , Dikes , Stratigraphy , and Structure of the Columbia River Basalt Group , Eastern Oregon and Southeastern Washington. *Scientific Investigations Report 2017-5022-N*(October), 88 p. doi: 10.3133/sir20175022N

Camp, V. E., & Ross, M. E. (2004). Mantle dynamics and genesis of mafic magmatism in the intermontane Pacific Northwest. *Journal of Geophysical Research: Solid Earth*, *109*(8), 1–14. doi: 10.1029/2003JB002838

Capra, L., Macías, J. L., Cortés, A., Dávila, N., Saucedo, R., Osorio-Ocampo, S., … Vázquez, R. (2016). Preliminary report on the July 10-11, 2015 eruption at Volcán de Colima: Pyroclastic density currents with exceptional runouts and volume. *Journal of Volcanology and Geothermal Research*, *310*, 39–49. (Publisher: Elsevier B.V.) doi: 10.1016/j.jvolgeores.2015.11.022

Capra, L., Sulpizio, R., Márquez-Ramirez, V. H., Coviello, V., Doronzo, D. M., Arambula-Mendoza, R., & Cruz, S. (2018, April). The anatomy of a pyroclastic density current: the 10 July 2015 event at Volcán de Colima (Mexico). *Bulletin of Volcanology*, *80*(4). (Publisher: Springer Verlag) doi: 10.1007/s00445-018-1206-4

Cashman, K. V., Stephen, R., & Sparks, J. (2013). How volcanoes work: A 25 year perspective. *Bulletin of the Geological Society of America*, *125*(5-6), 664–690. (ISBN: 0016-7606) doi: 10.1130/B30720.1

Charbonnier, S. J., & Gertisser, R. (2008). Field observations and surface characteristics of pristine block-and-ash fl ow deposits from the 2006 eruption of Merapi Volcano , Java , Indonesia. *Journal of Volcanology and Geothermal Research*, *177*(4), 971–982. Retrieved from `http://dx.doi.org/10.1016/j.jvolgeores.2008.07.008` (Publisher: Elsevier B.V.) doi: 10.1016/j.jvolgeores.2008.07.008

Charbonnier, S. J. J., Germa, A., Connor, C. B. B., Gertisser, R., Preece, K., Komorowski, J.-C. C., … Connor, L. (2013). Evaluation of the impact of the 2010 pyroclastic density currents at Merapi volcano from high-resolution satellite imagery, field investigations and numerical simulations. *Journal of Volcanology and Geothermal Research*, *261*, 295–315. Retrieved from `https://www.sciencedirect.com/science/article/pii/S0377027313000036` (Publisher: Elsevier)

Cheng, P., & Verma, A. K. (1980, December). *Boiling Heat Transfer from a Dike* (Tech. Rep. No. SGP-TR-50-33). University of Hawaii at Manoa, Honolulu, Hawaii. Retrieved 2024-05-30, from `https://www.osti.gov/biblio/889193`

Chester, D., Degg, M., Duncan, A., & Guest, J. (2000, September). The increasing exposure of cities to the effects of volcanic eruptions: a global survey. *Global Environmental Change Part B: Environmental Hazards*, *2*(3), 89–103. Retrieved 2024-03-25, from `https://linkinghub.elsevier.com/retrieve/pii/S1464286701000043` doi: 10.1016/S1464-2867(01)00004-3

Clarke, A. B., & Voight, B. (2000, July). Pyroclastic current dynamic pressure from aerodynamics of tree or pole blow-down. *Journal of Volcanology and Geothermal Research*, *100*(1-4), 395–412. (Publisher: Elsevier) doi: 10.1016/S0377-0273(00)00148-7

Cole, P. D., Calder, E. S., Druitt, T. H., Hoblitt, R., Robertson, R., Sparks, R. S., & Young, S. R. (1998, September). Pyroclastic flows generated by gravitational instability of the 1996-97 lava dome of Soufriere Hills Volcano, Montserrat. *Geophysical Research Letters*, *25*(18), 3425–3428. (Publisher: American Geophysical Union) doi: 10.1029/98GL01510

Cole, P. D., Calder, E. S., Sparks, R. S. J., Clarke, A. B., Druitt, T. H., Young, S. R., . . . Norton, G. E. (2002, January). Deposits from dome-collapse and fountain-collapse pyroclastic flows at Soufrière Hills Volcano, Montserrat. *Geological Society Memoir*, *21*(1), 231–262. Retrieved 2019-05-13, from `http://mem.lyellcollection.org/lookup/doi/10.1144/GSL.MEM.2002.021.01.11` (Publisher: Geological Society of London) doi: 10.1144/GSL.MEM.2002.021.01.11

Crane, K., & Bohanon, A. (2021). Dike Propagation During Global Contraction: Making Sense of Conflicting Stress Histories on Mercury. *Frontiers in Earth Science*, *9*(December), 1–14. doi: 10.3389/feart.2021.752864

Dade, W. B., & Huppert, H. E. (1995, June). A box model for non-entraining, suspension-driven gravity surges on horizontal surfaces. *Sedimentology*, *42*(3), 453–470. Retrieved 2019-06-12, from `http://doi.wiley.com/10.1111/j.1365-3091.1995.tb00384.x` (Publisher: John Wiley & Sons, Ltd (10.1111)) doi: 10.1111/j.1365-3091.1995.tb00384.x

Dade, W. B., & Huppert, H. E. (1996, June). Emplacement of the Taupo ignimbrite by a dilute turbulent flow. *Nature*, *381*(6582), 509–512. Retrieved 2019-06-12, from `http://www.nature.com/articles/381509a0` (Publisher: Nature Publishing Group) doi: 10.1038/381509a0

Dartevelle, S., Rose, W. I., Stix, J., Kelfoun, K., & Vallance, J. W. (2004). Numerical modeling of geophysical granular flows: 2. Computer simulations of plinian clouds and pyroclastic flows and surges. *Geochemistry, Geophysics, Geosystems*, *5*(8), 1–36. doi: 10.1029/2003GC000637

Davis, T., Bagnardi, M., Lundgren, P., & Rivalta, E. (2021). Extreme Curvature of Shallow Magma Pathways Controlled by Competing Stresses: Insights From the 2018 Sierra Negra Eruption. *Geophysical Research Letters*, *48*(13), 1–10. doi: 10.1029/2021GL093038

Delaney, P. T., Pollard, D. D., Ziony, J. I., & McKee, E. H. (1986). Field relations between dikes and joints: Emplacement processes and paleostress analysis. *Journal of Geophysical Research*, *91*(B5), 4920. doi: 10.1029/jb091ib05p04920

Delannay, R., Valance, A., Mangeney, A., Roche, O., & Richard, P. (2017). Granular and particle-laden flows: From laboratory experiments to field observations. *Journal of Physics D: Applied Physics*, *50*(5). doi: 10.1088/1361-6463/50/5/053001

Dellino, P., Dioguardi, F., Isaia, R., Sulpizio, R., & Mele, D. (2021, March). The impact of pyroclastic density currents duration on humans: the case of the AD 79 eruption of Vesuvius. *Scientific Reports*, *11*(1), 4959. Retrieved 2024-03-26, from `https://www.nature.com/articles/s41598-021-84456-7` (Publisher: Nature Publishing Group) doi: 10.1038/s41598-021-84456-7

Dellino, P., Zimanowski, B., Büttner, R., La Volpe, L., Mele, D., & Sulpizio, R. (2007, April). Large-scale experiments on the mechanics of pyroclastic flows: Design, engineering, and first results. *Journal of Geophysical Research: Solid Earth*, *112*(4), 4202. Retrieved 2021-03-11, from `http://doi.wiley.com/10.1029/2006JB004313` (Publisher: Blackwell Publishing Ltd) doi: 10.1029/2006JB004313

Denlinger, R. P. (1987). A Model for Generation of Ash Clouds by Pyroclastic Flows , With Application to the 1980 Eruptions at Mount St . Helens , Washington Our understanding of a large number of geologic processes The interstitial fluid velocity is sufficient to su- is limited. *Journal of Geophysical Research*, *92*, 284–298.

Dole, G., Das, S., & Kale, V. S. (2022). Tectonic framework of geomorphic evolution of the Deccan Volcanic Province, India. *Earth-Science Reviews*, *228*, 103988. (Publisher: Elsevier)

Doronzo, D. M., & Dellino, P. (2011, October). Interaction between pyroclastic density currents and buildings: Numerical simulation and first experiments. *Earth and Planetary Science Letters*, *310*(3-4), 286–292. (Publisher: Elsevier) doi: 10.1016/j.epsl.2011.08.017

Doyle, E. E., Hogg, A. J., Mader, H. M., & Sparks, R. S. (2008, February). Modeling dense pyroclastic basal flows from collapsing columns. *Geophysical Research Letters*, *35*(4). doi: 10.1029/2007GL032585

Druitt, T. H., Calder, E. S., Cole, P. D., Hoblitt, R. P., Loughlin, S. C., Norton, G. E., ... Voight, B. (2002). Small-volume, highly mobile pyroclastic flows formed by rapid sedimentation from pyroclastic surges at Soufrière Hills Volcano, Montserrat: an important volcanic hazard. *Geological Society Memoir*, *21*(1), 263–279. doi: 10.1144/GSL.MEM.2002.021.01.12

Duda, R. O., & Hart, P. E. (1972). Use of the Hough Transformation to Detect Lines and Curves in Pictures. *Communications of the ACM*, *15*(1), 11–15. doi: 10.1145/361237.361242

Dufek, J. (2016). The Fluid Mechanics of Pyroclastic Density Currents. *Annual Review of Fluid Mechanics*, *48*(September), 459–485. doi: 10.1146/annurev-fluid-122414-034252

Dufek, J., & Bergantz, G. W. (2007). Suspended load and bed-load transport of particle-laden gravity currents: The role of particle-bed interaction. *Theoretical and Computational Fluid Dynamics*, *21*, 119–145. (ISBN: 0935-4964) doi: 10.1007/s00162-007-0041-6

Dufek, J., Esposti Ongaro, T., & Roche, O. (2015). Pyroclastic Density Currents : Processes and Models. *The Encyclopedia of Volcanoes*, 617–629. Retrieved from `http://dx.doi.org/10.1016/B978-0-12-385938-9.00035-3` (ISBN: 9780123859389) doi: 10.1016/B978-0-12-385938-9.00035-3

Eberhardt, E. (2012). The hoek–brown failure criterion. In *The ISRM Suggested Methods for Rock Characterization, Testing and Monitoring: 2007-2014* (pp. 233–240). Springer.

Ellison, T. H., & Turner, J. S. (1959, October). Turbulent entrainment in stratified flows. *Journal of Fluid Mechanics*, *6*(03), 423. Retrieved 2019-06-12, from `http://www.journals.cambridge.org/abstract_S0022112059000738` (Publisher: Cambridge University Press) doi: 10.1017/S0022112059000738

Engelund, F. (1974). FLOW AND BED TOPOGRAPHY IN CHANNEL BENDS. *J. HYDRAUL. DIV. PROC. A.S.C.E.*, *100 , HY11*((NOVEMBER, 1974)), 1631–1648. doi: 10.1061/jyceaj.0004109

Ernst, R., Head, J. W., Parfitt, E., Grosfils, E., & Wilson, L. (1995). Giant radiating dyke swarms on Earth and Venus. *Earth Science Reviews*, *39*(1-2), 1–58. doi: 10.1016/0012-8252(95)00017-5

Ernst, R. E., Bond, D. P. G., Zhang, S., Buchan, K. L., Grasby, S. E., Youbi, N., ... Doucet, L. S. (2021a). Large Igneous Province Record Through Time and Implications for Secular Environmental Changes and Geological Time-Scale Boundaries. (January), 1–26. (ISBN: 9781119507444) doi: 10.1002/9781119507444.ch1

Ernst, R. E., Bond, D. P. G., Zhang, S., Buchan, K. L., Grasby, S. E., Youbi, N., ... Doucet, L. S. (2021b). Large Igneous Province Record Through Time and Implications for Secular Environmental Changes and Geological Time-Scale Boundaries. (January), 1–26. (ISBN: 9781119507444) doi: 10.1002/9781119507444.ch1

Esposti Ongaro, T., Cavazzoni, C., Erbacci, G., Neri, A., & Salvetti, M. V. (2007). A parallel multiphase flow code for the 3D simulation of explosive volcanic eruptions. *Parallel Computing*, *33*(7-8), 541–560. (ISBN: 9781860949630) doi: 10.1016/j.parco.2007.04.003

Esposti Ongaro, T., Neri, A., Menconi, G., de'Michieli Vitturi, M., Marianelli, P., Cavazzoni, C., ... Baxter, P. J. (2008). Transient 3D numerical simulations of column collapse and pyroclastic density current scenarios at Vesuvius. *Journal of Volcanology and Geothermal Research*, *178*(3), 378–396. Retrieved from `http://dx.doi.org/10.1016/j.jvolgeores.2008.06.036` (Publisher: Elsevier B.V.) doi: 10.1016/j.jvolgeores.2008.06.036

Esposti Ongaro, T., Orsucci, S., & Cornolti, F. (2016). A fast, calibrated model for pyroclastic density currents kinematics and hazard. *Journal of Volcanology and Geothermal Research*. doi: 10.1016/j.jvolgeores.2016.08.002

Everitt, B. (1980). *Cluster analysis* (Vol. 14). (Publication Title: Quality and Quantity Issue: 1 ISSN: 00335177) doi: 10.1007/BF00154794

Fahrig, W. F., & Jones, D. L. (1969). Paleomagnetic evidence for the extent of Mackenzie igneous events. *Canadian Journal of Earth Sciences*, *6*(4), 679–688. doi: 10.1139/e69-065

Fendley, I. M., Mittal, T., Sprain, C. J., Marvin-DiPasquale, M., Tobin, T. S., & Renne, P. R. (2019a). Constraints on the volume and rate of Deccan Traps flood basalt eruptions using a combination of high-resolution terrestrial mercury records and geochemical box models. *Earth and Planetary Science Letters*, *524*, 115721. Retrieved from `https://doi.org/10.1016/j.epsl.2019.115721` (Publisher: Elsevier B.V.) doi: 10.1016/j.epsl.2019.115721

Fendley, I. M., Mittal, T., Sprain, C. J., Marvin-DiPasquale, M., Tobin, T. S., & Renne, P. R. (2019b). Constraints on the volume and rate of Deccan Traps flood basalt eruptions using a combination of high-resolution terrestrial mercury records and geochemical box models. *Earth and Planetary Science Letters*, *524*, 115721. Retrieved from `https://doi.org/10.1016/j.epsl.2019.115721` (Publisher: Elsevier B.V.) doi: 10.1016/j.epsl.2019.115721

Fisher, R. V., & Schmincke, H.-U. (1984). *Pyroclastic Rocks*. Berline,: Springer Science & Business Media. (Publication Title: Pyroclastic Rocks) doi: 10.1007/978-3-642-74864-6_11

Flynn, I. T., & Ramsey, M. S. (2020). Pyroclastic density current hazard assessment and modeling uncertainties for Fuego volcano, Guatemala. *Remote Sensing*, *12*(17). doi: 10.3390/RS12172790

Fruchter, J. S., & Baldwin, S. F. (1975). Correlations between dikes of the Monument swarm, central Oregon, and Picture Gorge Basalt flows. *Geological Society of America Bulletin*, *86*(4), 514–516. (Publisher: Geological Society of America)

Fujii, T., & Nakada, S. (1999, April). The 15 September 1991 pyroclastic flows at Unzen Volcano (Japan): a flow model for associated ash-cloud surges. *Journal of Volcanology and Geothermal Research*, *89*(1-4), 159–172. Retrieved 2019-08-15, from `https://linkinghub.elsevier.com/retrieve/pii/S0377027398001309` (Publisher: Elsevier) doi: 10.1016/S0377-0273(98)00130-9

Gardner, J. E., Andrews, B. J., & Dennen, R. (2017). Liftoff of the 18 May 1980 surge of Mount St. Helens (USA) and the deposits left behind. *Bulletin of Volcanology*, *79*(1). (Publisher: Springer Verlag) doi: 10.1007/s00445-016-1095-3

Gaston, D. R., Permann, C. J., Peterson, J. W., Slaughter, A. E., Andrš, D., Wang, Y., ... Martineau, R. C. (2015, October). Physics-based multiscale coupling for full core nuclear reactor simulation. *Annals of Nuclear Energy*, *84*, 45–54. Retrieved 2024-05-31, from `https://www.sciencedirect.com/science/article/pii/S030645491400543X` doi: 10.1016/j.anucene.2014.09.060

Geographical and Geological Survey of the Rocky Mountain Region (U . S.), C. E. D. (1880). *... Report on the Geology of the High Plateaus of Utah, with Atlas*. Govt. Print. Off. Retrieved 2024-06-11, from `http://archive.org/details/reportongeology02duttgoog`

Gertisser, R., Cassidy, N. J., Charbonnier, S. J., Nuzzo, L., & Preece, K. (2012, January). Overbank block-and-ash flow deposits and the impact of valley-derived, unconfined flows on populated areas at Merapi volcano, Java, Indonesia. *Natural Hazards*, *60*(2), 623–648. Retrieved 2019-06-14, from `http://link.springer.com/10.1007/s11069-011-0044-x` (Publisher: Springer Netherlands) doi: 10.1007/s11069-011-0044-x

Glazner, A. F., & Mills, R. D. (2012). Interpreting two-dimensional cuts through broken geologic objects: Fractal and non-fractal size distributions. *Geosphere*, *8*(4), 902–914. doi: 10.1130/GES00731.1

Glen, J. M., & Ponce, D. A. (2002). Large-scale fractures related to inception of the Yellowstone hotspot. *Geology*, *30*(7), 647–650. doi: 10.1130/0091-7613(2002)030⟨0647:LSFRTI⟩2.0.CO;2

Gonnermann, H., & Taisne, B. (2015). Magma Transport in Dikes Author ' s personal copy. *Encyclopedia of Volcanoes*, 215–224. (ISBN: 9780123859389)

Green, C., Jackson, S. J., Gunning, J., Wilkins, A., & Ennis-King, J. (2024, March). Modelling the FluidFlower: Insights from Characterisation and Numerical Predictions. *Transport in Porous Media*, *151*(5), 1093–1111. Retrieved 2024-06-07, from `https://doi.org/10.1007/s11242-023-01969-7` doi: 10.1007/s11242-023-01969-7

Grosfils, E. B., & Head, J. W. (1994). The global distribution of giant radiation dike swarms on Venus : Implications for the global stress state. *Geophysical Research Letters*, *21*(8), 701–704.

Grosse, P., Ochi Ramacciotti, M. L., Escalante Fochi, F., Guzmán, S., Orihashi, Y., & Sumino, H. (2020). Geomorphology, morphometry, spatial distribution and ages of mafic monogenetic volcanoes of the Peinado and Incahuasi fields, southernmost Central Volcanic Zone of the Andes. *Journal of Volcanology and Geothermal Research*, *401*, 106966. Retrieved from `https://doi.org/10.1016/j.jvolgeores.2020.106966` (Publisher: Elsevier B.V.) doi: 10.1016/j.jvolgeores.2020.106966

Grosse, P., van Wyk de Vries, B., Petrinovic, I. A., Euillades, P. A., & Alvarado, G. E. (2009). Morphometry and evolution of arc volcanoes. *Geology*, *37*(7), 651–654. doi: 10.1130/G25734A.1

GSI District Resource Map. (2001). *District Resource Maps - India* (Tech. Rep.). (Publication Title: Geol. Surv. India (GSI))

Gudmundsson, A. (1995). Infrastructure and mechanics of volcanic systems in Iceland. *Journal of Volcanology and Geothermal Research*, *64*(1-2), 1–22. doi: 10.1016/0377-0273(95)92782-Q

Gudmundsson, A. (2002). Emplacement and arrest of sheets and dykes in central volcanoes. *Journal of Volcanology and Geothermal Research*, *116*(3-4), 279–298. doi: 10.1016/S0377-0273(02)00226-3

Gudmundsson, A. (2006). How local stresses control magma-chamber ruptures, dyke injections, and eruptions in composite volcanoes. *Earth-Science Reviews*, *79*(1-2), 1–31. doi: 10.1016/j.earscirev.2006.06.006

Gueugneau, V., Kelfoun, K., Charbonnier, S., Germa, A., & Carazzo, G. (2020). Dynamics and Impacts of the May 8th, 1902 Pyroclastic Current at Mount Pelée (Martinique): New Insights From Numerical Modeling. *Frontiers in Earth Science*, *8*(July). doi: 10.3389/feart.2020.00279

Gunaydin, D., Peirce, A. P., & Bunger, A. P. (2021, January). Laboratory Experiments Contrasting Growth of Uniformly and Nonuniformly Spaced Hydraulic Fractures. *Journal of Geophysical Research: Solid Earth*, *126*(1). Retrieved 2022-12-20, from `https://onlinelibrary.wiley.com/doi/full/10.1029/2020JB020107` (Publisher: John Wiley & Sons, Ltd) doi: 10.1029/2020JB020107

Harp, A. G. (2021). Magma propagation and emplacement within the central intrusive complex of Summer Coon stratovolcano, Colorado. *Journal of Volcanology and Geothermal Research*, *419*, 107372. Retrieved from `https://doi.org/10.1016/j.jvolgeores.2021.107372` (Publisher: The Author) doi: 10.1016/j.jvolgeores.2021.107372

Hough, P. V. C. (1962). *A method and means for recognition complex patterns.* (Pages: 6 Publication Title: US Patent)

Hudspith, V. A., Scott, A. C., Wilson, C. J., & Collinson, M. E. (2010). Charring of woods by volcanic processes: An example from the Taupo ignimbrite, New Zealand. *Palaeogeography, Palaeoclimatology, Palaeoecology*, *291*(1-2), 40–51. (Publisher: Elsevier B.V.) doi: 10.1016/j.palaeo.2009.06.036

Hákonardóttir, K. M., Hogg, A. J., Batey, J., & Woods, A. W. (2003, December). Flying avalanches. *Geophysical Research Letters*, *30*(23), n/a–n/a. Retrieved 2020-11-25, from `http://doi.wiley.com/10.1029/2003GL018172` (Publisher: American Geophysical Union) doi: 10.1029/2003GL018172

Ingebritsen, S. E., Geiger, S., Hurwitz, S., & Driesner, T. (2010, March). Numerical simulation of magmatic hydrothermal systems. *Reviews of Geophysics*, *48*(1), RG1002. Retrieved 2024-05-30, from `http://doi.wiley.com/10.1029/2009RG000287` doi: 10.1029/2009RG000287

Ingebritsen, S. E., & Hayba, D. O. (1994). Fluid flow and heat transport near the critical point of H2O - Ingebritsen - 2012 - Geophysical Research Letters - Wiley Online Library. , *21*(20), 2199–2202.

Jarman, A. M. (2020). Hierarchical Cluster Analysis: Comparison of Single linkage,Complete linkage, Average linkage and Centroid Linkage Method. , 1–13. Retrieved from https://www.researchgate.net/publication/339443595_Hierarchical_Cluster_Analysis_Comparison_of_Single_linkageComplete_linkage_Average_linkage_and_Centroid_Linkage_Method

Jay, A. E., & Widdowson, M. (2008). Stratigraphy, structure and volcanology of the SE Deccan continental flood basalt province: Implications for eruptive extent and volumes. *Journal of the Geological Society*, *165*(1), 177–188. doi: 10.1144/0016-76492006-062

J. Branney, M., & Kokelaar, P. (2002). *Pyroclastic density currents and the sedimentation of ignimbrites.* Geological Society. (arXiv: gr-qc/9809069v1 Publication Title: Geological Society Memoir No. 27 ISSN: 0022-1376)

Jenkins, S., Komorowski, J.-C. C., Baxter, P. J. J., Spence, R., Picquout, A., Lavigne, F., & Surono. (2013). The Merapi 2010 eruption: An interdisciplinary impact assessment methodology for studying pyroclastic density current dynamics. *Journal of Volcanology and Geothermal Research*, *261*, 316–329. Retrieved from https://www.sciencedirect.com/science/article/pii/S0377027313000632 (Publisher: Elsevier B.V.) doi: 10.1016/j.jvolgeores.2013.02.012

John, D. U. G. S., Wallace, A. U. G. S., Ponce, D., Fleck, R., & Conrad, J. (2000). New Perspectives on the Geology and Origin of the Northern Nevada Rift..

Johnson, R. (1961). Patterns and Origin of Radial Dike Swarms Associated with West Spanish Peak and Dike Mountain, South-Central Colorado. *Geological Society of America Bulletin*, *72*(April), 579–590.

Jolly, R. J. H., & Sanderson, D. J. (1995). Variation in the form and distribution of dykes in the Mull swarm, Scotland. *Journal of Structural Geology*, *17*(11), 1543–1557. doi: 10.1016/0191-8141(95)00046-G

Jordahl, K., Bossche, J. V. D., Fleischmann, M., Wasserman, J., McBride, J., Gerard, J., … Leblanc, F. (2020, July). *geopandas/geopandas: v0.8.1.* [object Object]. Retrieved 2024-06-11, from https://zenodo.org/record/3946761 doi: 10.5281/ZENODO.3946761

Josephy, A. M. (1997). *The Nez Perce Indians and the opening of the Northwest.* Boston, Mass: Houghton Mifflin.

Karlstrom, L., Dufek, J., & Manga, M. (2009). Organization of volcanic plumbing through magmatic lensing by magma chambers and volcanic loads. *Journal of Geophysical Research: Solid Earth*, *114*(10), 1–16. doi: 10.1029/2009JB006339

Karlstrom, L., Paterson, S. R., & Jellinek, A. M. (2017). A reverse energy cascade for crustal magma transport. *Nature Geoscience*, *10*(8), 604–608. doi: 10.1038/NGEO2982

Kasbohm, J., & Schoene, B. (2018). Rapid eruption of the Columbia River flood basalt and correlation with the mid-Miocene climate optimum. *Science Advances*, *4*(9), 8223. Retrieved from `https://www.science.org/doi/10.1126/sciadv.aat8223` (Publisher: American Association for the Advancement of Science) doi: 10.1126/SCIADV.AAT8223/SUPPL{_}FILE/AAT8223{_}TABLE{_}S1.XLS

Kavanagh, J. L., Boutelier, D., & Cruden, A. R. (2015). The mechanics of sill inception, propagation and growth: Experimental evidence for rapid reduction in magmatic overpressure. *Earth and Planetary Science Letters*, *421*, 117–128. doi: 10.1016/j.epsl.2015.03.038

Kavanagh, J. L., Burns, A. J., Hilmi Hazim, S., Wood, E. P., Martin, S. A., Hignett, S., & Dennis, D. J. C. (2018). Challenging dyke ascent models using novel laboratory experiments: Implications for reinterpreting evidence of magma ascent and volcanism. *Journal of Volcanology and Geothermal Research*, *354*, 87–101. Retrieved from `https://doi.org/10.1016/j.jvolgeores.2018.01.002` (Publisher: The Authors) doi: 10.1016/j.jvolgeores.2018.01.002

Kavanagh, J. L., Menand, T., & Sparks, R. S. J. (2006). An experimental investigation of sill formation and propagation in layered elastic media. *Earth and Planetary Science Letters*, *245*(3-4), 799–813. doi: 10.1016/j.epsl.2006.03.025

Kavanagh, J. L., & Pavier, M. J. (2014). Rock interface strength influences fluid-filled fracture propagation pathways in the crust. *Journal of Structural Geology*, *63*, 68–75. (Publisher: Elsevier)

Kelfoun, K., & Druitt, T. H. (2005, December). Numerical modeling of the emplacement of Socompa rock avalanche, Chile. *Journal of Geophysical Research: Solid Earth*, *110*(12), 1–13. (Publisher: Blackwell Publishing Ltd) doi: 10.1029/2005JB003758

Kelfoun, K., Gueugneau, V., Komorowski, J.-C., Aisyah, N., Cholik, N., & Merciecca, C. (2017, June). Simulation of block-and-ash flows and ash-cloud surges of the 2010 eruption of Merapi volcano with a two-layer model. *Journal of Geophysical Research: Solid Earth*, *122*(6), 4277–4292. Retrieved 2020-12-01, from `http://doi.wiley.com/10.1002/2017JB013981` (Publisher: Blackwell Publishing Ltd) doi: 10.1002/2017JB013981

Kirk, B. S., Peterson, J. W., Stogner, R. H., & Carey, G. F. (2006, December). libMesh: a C++ library for parallel adaptive mesh refinement/coarsening simulations. *Engineering with Computers*, *22*(3), 237–254. Retrieved 2024-03-27, from `https://doi.org/10.1007/s00366-006-0049-3` doi: 10.1007/s00366-006-0049-3

Komorowski, J.-C., Jenkins, S., Baxter, P. J., Picquout, A., Lavigne, F., Charbonnier, S., … Surono (2013). Paroxysmal dome explosion during the Merapi 2010 eruption: Processes and facies relationships of associated high-energy pyroclastic density currents. *Journal of Volcanology and Geothermal Research*, *261*, 260–294. Retrieved from `https://www.sciencedirect.com/science/article/pii/S0377027313000176` (Publisher: Elsevier) doi: 10.1016/J.JVOLGEORES.2013.01.007

Krumbholz, M., Hieronymus, C. F., Burchardt, S., Troll, V. R., Tanner, D. C., & Friese, N. (2014). Weibull-distributed dyke thickness reflects probabilistic character of host-rock strength. *Nature Communications*, *5*, 1–7. (Publisher: Nature Publishing Group) doi: 10.1038/ncomms4272

Kubo Hutchison, A., & Dufek, J. (2021). Generation of Overspill Pyroclastic Density Currents in Sinuous Channels. *Journal of Geophysical Research. Solid Earth*. doi: 10.1029/2021JB022442

Kubo Hutchison, A., Karlstrom, L., & Mittal, T. (2023). Multiscale spatial patterns in giant dike swarms identified through objective feature extraction. *Geochemistry, Geophysics, Geosystems*, *24*(9), e2022GC010842. (Publisher: Wiley Online Library) doi: 10.1029/2022GC010842

Lindsay, A., Giudicelli, G., German, P., Peterson, J., Wang, Y., Freile, R., … Schunert, S. (2023). MOOSE Navier–Stokes module. *SoftwareX*, *23*, 101503. Retrieved from `https://doi.org/10.1016/j.softx.2023.101503` (Publisher: Elsevier B.V.) doi: 10.1016/j.softx.2023.101503

Loughlin, S. C., Baxter, P. J., Aspinall, W. P., Darroux, B., Harford, C. L., & Miller, A. D. (2002). Eyewitness accounts of the 25 June 1997 pyroclastic flows and surges at Soufrière Hills Volcano, Montserrat, and implications for disaster mitigation. *Geological Society Memoir*, *21*(1), 211–230. doi: 10.1144/GSL.MEM.2002.021.01.10

Lube, G., Breard, E. C., Cronin, S. J., & Jones, J. (2015). Synthesizing large-scale pyroclastic flows: Experimental design, scaling, and first results from PELE. *Journal of Geophysical Research: Solid Earth*, *120*(3), 1487–1502. doi: 10.1002/2014JB011666

Lube, G., Breard, E. C., Jones, J., Fullard, L., Dufek, J., Cronin, S. J., & Wang, T. (2019). Generation of air lubrication within pyroclastic density currents. *Nature Geoscience*, *12*(5), 381–386. doi: 10.1038/s41561-019-0338-2

Lube, G., Breard, E. C. P., Esposti-Ongaro, T., Dufek, J., & Brand, B. (2020). Multiphase flow behaviour and hazard prediction of pyroclastic density currents. *Nature Reviews Earth & Environment*, *1*(7), 348–365. Retrieved from `http://dx.doi.org/10.1038/s43017-020-0064-8%0Ahttp://www.nature.com/articles/s43017-020-0064-8%0Ahttp://www.nature.com/articles/s43017-020-0064-8` (Publisher: Springer US) doi: 10.1038/s43017-020-0064-8

Lube, G., Cronin, S. J., Thouret, J. C., & Surono, S. (2011). Kinematic characteristics of pyroclastic density currents at merapi and controls on their avulsion from natural and engineered channels. *Bulletin of the Geological Society of America*, *123*(5), 1127–1140. doi: 10.1130/B30244.1

Ma, L., Li, Z., Wang, M., Wu, J., & Li, G. (2020). Applicability of a new modified explicit three-dimensional Hoek-Brown failure criterion to eight rocks. *International Journal of Rock Mechanics and Mining Sciences*, *133*, 104311. (Publisher: Elsevier)

Macorps, E., Charbonnier, S. J., Varley, N. R., Capra, L., Atlas, Z., & Cabré, J. (2018). Stratigraphy, sedimentology and inferred flow dynamics from the July 2015 block-and-ash flow deposits at Volcán de Colima, Mexico. *Journal of Volcanology and Geothermal Research*, *349*, 99–116. Retrieved from `https://doi.org/10.1016/j.jvolgeores.2017.09.025` (Publisher: Elsevier B.V.) doi: 10.1016/j.jvolgeores.2017.09.025

Martí, J., Doronzo, D. M., Pedrazzi, D., & Colombo, F. (2019, October). Topographical controls on small-volume pyroclastic flows. *Sedimentology*, *66*(6), 2297–2317. Retrieved 2020-08-14, from `https://onlinelibrary.wiley.com/doi/abs/10.1111/sed.12600` (Publisher: Blackwell Publishing Ltd) doi: 10.1111/sed.12600

McPhee, J. A. (1990). *Basin and range: Farrar, Straus and Giroux* (1. Farrar, Straus and Giroux paperb. ed ed.). New York: Selbstverl.

Mittal, T., & Richards, M. A. (2021a). The Magmatic Architecture of Continental Flood Basalts: 2. A New Conceptual Model. *Journal of Geophysical Research: Solid Earth*, *126*(12). doi: 10.1029/2021JB021807

Mittal, T., & Richards, M. A. (2021b). The Magmatic Architecture of Continental Flood Basalts: 2. A New Conceptual Model. *Journal of Geophysical Research: Solid Earth*, *126*(12). doi: 10.1029/2021JB021807

Mittal, T., Richards, M. A., & Fendley, I. M. (2021). The Magmatic Architecture of Continental Flood Basalts I: Observations From the Deccan Traps. *Journal of Geophysical Research: Solid Earth*, *126*(12), 1–81. doi: 10.1029/2021jb021808

Morriss, M. C., Karlstrom, L., Nasholds, M. W., & Wolff, J. A. (2020). The chief Joseph dike swarm of the Columbia river flood basalts, and the legacy data set of William H. Taubeneck. *Geosphere*, *16*(4), 1793–1817. doi: 10.1130/GES02173.1

Morton, B., Taylor, G., & Turner, J. (1956, January). Turbulent gravitational convection from maintained and instantaneous sources. *Proceedings of the Royal Society of London. Series A. Mathematical and Physical Sciences*, *234*(1196), 1–23. (Publisher: The Royal Society) doi: 10.1098/rspa.1956.0011

Mukhopadhyay, P., & Chaudhuri, B. B. (2015, March). A survey of Hough Transform. *Pattern Recognition*, *48*(3), 993–1010. Retrieved 2024-06-11, from `https://linkinghub.elsevier.com/retrieve/pii/S0031320314003446` doi: 10.1016/j.patcog.2014.08.027

Muller, O. H., & Pollard, D. D. (1977). The stress state near Spanish Peaks, colorado determined from a dike pattern. *Pure and Applied Geophysics PAGEOPH*, *115*(1-2), 69–86. doi: 10.1007/BF01637098

Mège, D., & Korme, T. (2004). Dyke swarm emplacement in the Ethiopian Large Igneous Province: Not only a matter of stress. *Journal of Volcanology and Geothermal Research*, *132*(4), 283–310. (Publisher: Elsevier) doi: 10.1016/S0377-0273(03)00318-4

Müllner, D. (2011). Modern hierarchical, agglomerative clustering algorithms. (1973), 1–29. Retrieved from `http://arxiv.org/abs/1109.2378` (arXiv: 1109.2378)

Nerburn, K. (2005). *Chief Joseph & the flight of the Nez Perce: the untold story of an American tragedy* (1st ed. ed.). New York, NY: HarperSanFrancicso. (OCLC: 62154088)

Nicolas, A., Boudier, F., Koepke, J., France, L., Ildefonse, B., & Mevel, C. (2008). Root zone of the sheeted dike complex in the Oman ophiolite. *Geochemistry, Geophysics, Geosystems*, *9*(5). (Publisher: Wiley Online Library)

Odé, H. (1957). Mechanical analysis of the dike pattern of the Spanish peaks area, Colorado. *Bulletin of the Geological Society of America*, *68*(5), 567–576. doi: 10.1130/0016-7606(1957)68[567:MAOTDP]2.0.CO;2

Ogburn, S. E. (2012). FlowDat: Mass flow Database. *Vhub*, *V2.2*.

Ogburn, S. E., & Calder, E. S. (2017). The relative effectiveness of empirical and physical models for simulating the dense undercurrent of pyroclastic flows under different emplacement conditions. *Frontiers in Earth Science*, *5*(November). doi: 10.3389/feart.2017.00083

Ogburn, S. E., Calder, E. S., Cole, P. D., & Stinton, A. J. (2014). Chapter 10 The effect of topography on ash-cloud surge generation and propagation. *Geological Society, London, Memoirs*, *39*(1), 179–194. (Publisher: Geological Society of London) doi: 10.1144/m39.10

Ovaskainen, N. (2023, May). fractopo: A Python package for fracture network analysis. *Journal of Open Source Software*, *8*(85), 5300. Retrieved 2024-06-11, from `https://joss.theoj.org/papers/10.21105/joss.05300` doi: 10.21105/joss.05300

O'Hara, D., Karlstrom, L., & Ramsey, D. W. (2020, July). Time-evolving surface and subsurface signatures of Quaternary volcanism in the Cascades arc. *Geology*, *48*(11), 1088–1093. Retrieved from `https://doi.org/10.1130/G47706.1` doi: 10.1130/G47706.1

pandas development team, T. (2020, February). *pandas-dev/pandas: Pandas.* Zenodo. Retrieved from `https://doi.org/10.5281/zenodo.3509134` doi: 10.5281/zenodo.3509134

Paquet, F., Dauteuil, O., Hallot, E., & Moreau, F. (2007). Tectonics and magma dynamics coupling in a dyke swarm of Iceland. *Journal of Structural Geology*, *29*(9), 1477–1493. doi: 10.1016/j.jsg.2007.06.001

Patra, A. K., Bauer, A. C., Nichita, C. C., Pitman, E. B., Sheridan, M. F., Bursik, M., … Renschler, C. S. (2005). Parallel adaptive numerical simulation of dry avalanches over natural terrain. *Journal of Volcanology and Geothermal Research*, *139*(1-2), 1–21. doi: 10.1016/j.jvolgeores.2004.06.014

Penn, B. S., & Lindsey, D. A. (2009). 40Ar/39Ar dates for the Spanish Peaks intrusions in south-central Colorado. *Rocky Mountain Geology*, *44*(1), 17–32. doi: 10.2113/gsrocky.44.1.17

Pensa, A., Capra, L., & Giordano, G. (2019). Ash clouds temperature estimation. Implication on dilute and concentrated PDCs coupling and topography confinement. *Scientific Reports*, *9*(1), 1–14. Retrieved from http://dx.doi.org/10.1038/s41598-019-42035-x (Publisher: Springer US) doi: 10.1038/s41598-019-42035-x

Pensa, A., Capra, L., Giordano, G., & Corrado, S. (2018, May). Emplacement temperature estimation of the 2015 dome collapse of Volcán de Colima as key proxy for flow dynamics of confined and unconfined pyroclastic density currents. *Journal of Volcanology and Geothermal Research*, *357*, 321–338. Retrieved from https://linkinghub.elsevier.com/retrieve/pii/S0377027317307412 doi: 10.1016/j.jvolgeores.2018.05.010

Pensa, A., Porreca, M., Corrado, S., Giordano, G., & Cas, R. (2015, February). Calibrating the pTRM and charcoal reflectance (Ro%) methods to determine the emplacement temperature of ignimbrites: Fogo A sequence, São Miguel, Azores, Portugal, as a case study. *Bulletin of Volcanology*, *77*(3), 1–19. Retrieved 2020-11-24, from https://link.springer.com/article/10.1007/s00445-015-0904-4 (Publisher: Springer Verlag) doi: 10.1007/s00445-015-0904-4

Permann, C. J., Gaston, D. R., Andrš, D., Carlsen, R. W., Kong, F., Lindsay, A. D., … Martineau, R. C. (2020, January). MOOSE: Enabling massively parallel multiphysics simulation. *SoftwareX*, *11*. Retrieved 2024-03-25, from https://www.softxjournal.com/article/S2352-7110(19)30297-3/fulltext (Publisher: Elsevier) doi: 10.1016/j.softx.2020.100430

Petcovic, H. L., & Dufek, J. (2005a). Modeling magma flow and cooling in dikes: Implications for emplacement of Columbia River flood basalts. *Journal of Geophysical Research: Solid Earth*, *110*(10), 1–15. doi: 10.1029/2004JB003432

Petcovic, H. L., & Dufek, J. D. (2005b, October). Modeling magma flow and cooling in dikes: Implications for emplacement of Columbia River flood basalts. *Journal of Geophysical Research: Solid Earth*, *110*(B10), 2004JB003432. Retrieved 2024-05-30, from https://agupubs.onlinelibrary.wiley.com/doi/10.1029/2004JB003432 doi: 10.1029/2004JB003432

Petcovic, H. L., & Grunder, A. L. (2003). Textural and thermal history of partial melting in tonalitic wallrock at the margin of a basalt dike, Wallowa Mountains, Oregon. *Journal of Petrology*, *44*(12), 2287–2312. (Publisher: Oxford University Press)

Piper, D. J., & Normark, W. R. (1983). Turbidite depositional patterns and flow characteristics, Navy Submarine Fan, California Borderland. *Sedimentology*, *30*, 681–694. (ISBN: 9781444304473) doi: 10.1002/9781444304473.ch33

Pollard, D. D., Segall, P., & Delaney, P. T. (1982). Formation and interpretation of dilatant echelon cracks. *Geological Society of America Bulletin*, *93*(12), 1291–1303. doi: 10.1130/0016-7606(1982)93⟨1291:FAIODE⟩2.0.CO;2

Rajaram, M., Anand, S. P., Erram, V. C., & Shinde, B. N. (2017). Insight into the structures below the Deccan Trap-covered region of Maharashtra, India from geopotential data. *Geological Society, London, Special Publications*, *445*(1), 219–236. (Publisher: Geological Society of London)

Raju, N., & Meiburg, E. (1995). The accumulation and dispersion of heavy particles in forced two-dimensional mixing layers. Part 2: The effect of gravity. *Physics of Fluids*, *7*, 1241. Retrieved 2021-01-28, from `https://doi.org/10.1063/1.868581` doi: 10.1063/1.868581

Rao, J. V., Ravikumar, B., & Golani, P. R. (2022). What lies beneath the Deccan volcanic province? Perspective on tectonic elements and sub-trappean geology from gravity signatures. *Journal of Earth System Science*, *131*(1), 1–20. (Publisher: Springer)

Ray, R., Sheth, H. C., & Mallik, J. (2007). Structure and emplacement of the Nandurbar-Dhule mafic dyke swarm, Deccan Traps, and the tectonomagmatic evolution of flood basalts. *Bulletin of Volcanology*, *69*(5), 537–551. doi: 10.1007/s00445-006-0089-y

Reidel, S. P., Camp, V. E., Tolan, T. L., Kauffman, J. D., & Garwood, D. L. (2013). Tectonic evolution of the Columbia River flood basalt province. *Special Paper of the Geological Society of America*, *497*(August), 293–324. (ISBN: 9780813724973) doi: 10.1130/2013.2497(12)

Reidel, S. P., Camp, V. E., Tolan, T. L., & Martin, B. S. (2013). The Columbia River flood basalt province: Stratigraphy, areal extent, volume, and physical volcanology. *Special Paper of the Geological Society of America*, *497*, 1–43. (Publisher: Geological Society of America ISBN: 9780813724973) doi: 10.1130/2013.2497(01)

Richard, J., & Ogba, C. (2016). Analysis of Accuracy of Differential Global Positioning System (DGPS) and Google Earth Digital Terrain Model (DTM) Data using Geographic Information System Techniques Analysis of Accuracy of Differential Global Positioning System (DGPS) and Google Earth D. *Journal of Geodesy and Geomatics Engineering*, *2*, 52–61. doi: 10.17265/2332-8223/2016.02.006

Rivalta, E., Taisne, B., Bunger, A. P., & Katz, R. F. (2015). A review of mechanical models of dike propagation: Schools of thought, results and future directions. *Tectonophysics*, *638*(C), 1–42. doi: 10.1016/j.tecto.2014.10.003

Rivas-Dorado, S., Ruíz, J., & Romeo, I. (2022, September). Giant dikes and dike-induced seismicity in a weak crust underneath Cerberus Fossae, Mars. *Earth and Planetary Science Letters*, *594*, 117692. (Publisher: Elsevier) doi: 10.1016/j.epsl.2022.117692

Roche, O. (2012a, October). Depositional processes and gas pore pressure in pyroclastic flows: an experimental perspective. *Bulletin of Volcanology*, *74*(8), 1807–1820. Retrieved 2019-06-12, from `http://link.springer.com/10.1007/s00445-012-0639-4` (Publisher: Springer-Verlag) doi: 10.1007/s00445-012-0639-4

Roche, O. (2012b, October). Depositional processes and gas pore pressure in pyroclastic flows: an experimental perspective. *Bulletin of Volcanology*, *74*(8), 1807–1820. Retrieved 2019-06-12, from `http://link.springer.com/10.1007/s00445-012-0639-4` (Publisher: Springer-Verlag) doi: 10.1007/s00445-012-0639-4

Roche, O., Buesch, D. C., & Valentine, G. A. (2016). Slow-moving and far-travelled dense pyroclastic flows during the Peach Spring super-eruption. *Nature Communications*, *7*. doi: 10.1038/ncomms10890

Roche, O., Niño, Y., Mangeney, A., Brand, B., Pollock, N., & Valentine, G. A. (2013). Dynamic pore-pressure variations induce substrate erosion by pyroclastic flows. *Geology*, *41*(10), 1107–1110. doi: 10.1130/G34668.1

Roman, A., & Jaupart, C. (2014). The impact of a volcanic edifice on intrusive and eruptive activity. *Earth and Planetary Science Letters*, *408*, 1–8. Retrieved from `http://dx.doi.org/10.1016/j.epsl.2014.09.016` (Publisher: Elsevier B.V.) doi: 10.1016/j.epsl.2014.09.016

Rubin, A. M. (1995). Propogation of Magma-filled Cracks. *Annual Review of Earth {\&} Planetary Sciences*, 287–336.

Saucedo, R., Macıas, J., Bursik, M., Mora, J., Gavilanes, J., & Cortes, A. (2002, September). Emplacement of pyroclastic flows during the 1998–1999 eruption of Volcán de Colima, México. *Journal of Volcanology and Geothermal Research*, *117*(1-2), 129–153. Retrieved 2019-10-06, from `https://linkinghub.elsevier.com/retrieve/pii/S037702730200241X` doi: 10.1016/S0377-0273(02)00241-X

Scharff, L., Hort, M., & Varley, N. R. (2019, December). First in-situ observation of a moving natural pyroclastic density current using Doppler radar. *Scientific Reports*, *9*(1). Retrieved 2020-01-10, from `https://www.nature.com/articles/s41598-019-43620-w` (Publisher: Nature Publishing Group) doi: 10.1038/s41598-019-43620-w

Schoene, B., Eddy, M. P., Keller, C. B., & Samperton, K. M. (2021). An evaluation of Deccan Traps eruption rates using geochronologic data. *Geochronology*, *3*(1), 181–198. doi: 10.5194/gchron-3-181-2021

Self, S., Mittal, T., Dole, G., & Vanderkluysen, L. (2022, May). Toward Understanding Deccan Volcanism. *Annual Review of Earth and Planetary Sciences*, *50*(Volume 50, 2022), 477–506. Retrieved 2024-03-25, from `https://www.annualreviews.org/content/journals/10.1146/annurev-earth-012721-051416` (Publisher: Annual Reviews) doi: 10.1146/annurev-earth-012721-051416

Self, S., Widdowson, M., Thordarson, T., & Jay, A. E. (2006). Volatile fluxes during flood basalt eruptions and potential effects on the global environment: A Deccan perspective. *Earth and Planetary Science Letters*, *248*(1-2), 518–532. doi: 10.1016/j.epsl.2006.05.041

Sheridan, M. F. (1979). Emplacement of pyroclastic flows: A review. , 125–136. doi: 10.1130/spe180-p125

Sheth, H., Vanderkluysen, L., Demonterova, E. I., Ivanov, A. V., & Savatenkov, V. M. (2019). Geochemistry and 40 Ar/ 39 Ar geochronology of the Nandurbar-Dhule mafic dyke swarm: Dyke-sill-flow correlations and stratigraphic development across the Deccan flood basalt province. *Geological Journal*, *54*(1), 157–176. doi: 10.1002/gj.3167

Sheth, H. C., & Cañón-Tapia, E. (2015). Are flood basalt eruptions monogenetic or polygenetic? *International Journal of Earth Sciences*, *104*(8), 2147–2162. Retrieved from `http://dx.doi.org/10.1007/s00531-014-1048-z` (Publisher: Springer Berlin Heidelberg) doi: 10.1007/s00531-014-1048-z

Shimizu, H. A., Koyaguchi, T., & Suzuki, Y. J. (2017). A numerical shallow-water model for gravity currents for a wide range of density differences. *Progress in Earth and Planetary Science*. doi: 10.1186/s40645-017-0120-2

Shukla, G., Mallik, J., & Mondal, P. (2022, November). Dimension-scaling relationships of Pachmarhi dyke swarm and their implications on Deccan magma emplacement. *Tectonophysics*, *843*, 229602. (Publisher: Elsevier) doi: 10.1016/J.TECTO.2022.229602

Simpson, J. E. (1987). *Gravity Currents: In the environment and the laboratory.* Cambridge University Press.

Small, C., & Naumann, T. (2001, January). The global distribution of human population and recent volcanism. *Global Environmental Change Part B: Environmental Hazards*, *3*(3), 93–109. Retrieved 2024-03-25, from https://doi.org/10.3763/ehaz.2001.0309 (Publisher: Taylor & Francis _eprint: https://doi.org/10.3763/ehaz.2001.0309) doi: 10.3763/ehaz.2001.0309

Sneath, P. H. (1957, August). The application of computers to taxonomy. *Journal of general microbiology*, *17*(1), 201–226. Retrieved 2022-11-15, from https://www.microbiologyresearch.org/content/journal/micro/10.1099/00221287-17-1-201 (Publisher: Microbiology Society) doi: 10.1099/00221287-17-1-201

Sorenson, T. (1948). A method of establishing groups of equal amplitude in plant sociology based on similarity of species content and its application to analyses of the vegetation on Danish commons. *Biologiske Skrifter*, *5*, 1–34.

Sparks, R. S., Gardeweg, M. C., Calder, E. S., & Matthews, S. J. (1997). Erosion by pyroclastic flows on Lascar Volcano, Chile. *Bulletin of Volcanology*, *58*(7), 557–565. doi: 10.1007/s004450050162

Sparks, R. S. J. (1976). Grain size variations in ignimbrites and implications for the transport of pyroclastic flows. *Sedimentology*, *23*(2), 147–188. doi: 10.1111/j.1365-3091.1976.tb00045.x

Straub, K. M., Mohrig, D., McElroy, B., Buttles, J., & Pirmez, C. (2008, March). Interactions between turbidity currents and topography in aggrading sinuous submarine channels: A laboratory study. *Bulletin of the Geological Society of America*, *120*(3-4), 368–385. (Publisher: GeoScienceWorld) doi: 10.1130/B25983.1

Sulpizio, R., Capra, L., Sarocchi, D., Saucedo, R., Gavilanes-Ruiz, J. C., & Varley, N. R. (2010, June). Predicting the block-and-ash flow inundation areas at Volcán de Colima (Colima, Mexico) based on the present day (February 2010) status. *Journal of Volcanology and Geothermal Research*, *193*(1-2), 49–66. doi: 10.1016/j.jvolgeores.2010.03.007

Sulpizio, R., Dellino, P., Doronzo, D. M., & Sarocchi, D. (2014). Pyroclastic density currents: State of the art and perspectives. *Journal of Volcanology and Geothermal Research*, *283*, 36–65. doi: 10.1016/j.jvolgeores.2014.06.014

Sulpizio, R., Zanella, E., Macías, J. L., & Saucedo, R. (2015). Deposit temperature of pyroclastic density currents emplaced during the El Chichón 1982 and Colima 1913 eruptions. *Geological Society Special Publication*, *396*, 39–49. doi: 10.1144/SP396.5

Syamlal, M. (1998). MFIX documentation numerical technique Gasification View project Gas Separations Carbon Capture View project MFIX Documentation Numerical Technique. Retrieved from `https://www.researchgate.net/publication/242368478` doi: 10.2172/656644

Thiele, S. T., Cruden, A. R., Micklethwaite, S., Bunger, A. P., & Köpping, J. (2020). Dyke apertures record stress accumulation during sustained volcanism. *Scientific Reports*, *10*(1), 1–9. Retrieved from `https://doi.org/10.1038/s41598-020-74361-w` (Publisher: Nature Publishing Group UK ISBN: 4159802074361) doi: 10.1038/s41598-020-74361-w

Townsend, M., & Huber, C. (2020). A critical magma chamber size for volcanic eruptions. *Geology*, *48*(5), 431–435. doi: 10.1130/G47045.1

Trolese, M., Cerminara, M., Esposti Ongaro, T., & Giordano, G. (2019, December). The footprint of column collapse regimes on pyroclastic flow temperatures and plume heights. *Nature Communications*, *10*(1), 1–10. Retrieved 2020-07-26, from `https://doi.org/10.1038/s41467-019-10337-3` (Publisher: Nature Publishing Group) doi: 10.1038/s41467-019-10337-3

Trolese, M., Giordano, G., Komorowski, J. C., Jenkins, S. F., Baxter, P. J., Cholik, N., ... Corrado, S. (2018, June). Very rapid cooling of the energetic pyroclastic density currents associated with the 5 November 2010 Merapi eruption (Indonesia). *Journal of Volcanology and Geothermal Research*, *358*, 1–12. (Publisher: Elsevier B.V.) doi: 10.1016/j.jvolgeores.2018.06.004

Turcotte, D. L., & Schubert, G. (2002). *Geodynamics*. Cambridge University Press.

Turner, J. S. (1986, December). No Title. *Journal of Fluid Mechanics*, *173*, 431–471. Retrieved 2019-06-12, from `https://www.cambridge.org/core/product/identifier/S0022112086001222/type/journal_article` (Publisher: Cambridge University Press) doi: 10.1017/S0022112086001222

Ui, T., Matsuwo, N., Sumita, M., & Fujinawa, A. (1999, April). Generation of block and ash flows during the 1990-1995 eruption of Unzen Volcano, Japan. *Journal of Volcanology and Geothermal Research*, *89*(1-4), 123–137. doi: 10.1016/S0377-0273(98)00128-0

Urbani, S., Acocella, V., & Rivalta, E. (2018). What Drives the Lateral Versus Vertical Propagation of Dikes? Insights From Analogue Models. *Journal of Geophysical Research: Solid Earth*, *123*(5), 3680–3697. doi: 10.1029/2017JB015376

Valentine, G. A. (1998, December). Damage to structures by pyroclastic flows and surges, inferred from nuclear weapons effects. *Journal of Volcanology and Geothermal Research*, *87*(1-4), 117–140. (Publisher: Elsevier Sci B.V.) doi: 10.1016/S0377-0273(98)00094-8

Valentine, G. A., Doronzo, D. M., Dellino, P., & de Tullio, M. D. (2011, October). Effects of volcano profile on dilute pyroclastic density currents: Numerical simulations. *Geology*, *39*(10), 947–950. (Publisher: GeoScienceWorld) doi: 10.1130/G31936.1

Vanderkluysen, L., Mahoney, J. J., Hooper, P. R., Sheth, H. C., & Ray, R. (2011). The feeder system of the Deccan Traps (India): Insights from dike geochemistry. *Journal of Petrology*, *52*(2), 315–343. doi: 10.1093/petrology/egq082

Virtanen, P., Gommers, R., Oliphant, T. E., Haberland, M., Reddy, T., Cournapeau, D., … Vázquez-Baeza, Y. (2020, March). SciPy 1.0: fundamental algorithms for scientific computing in Python. *Nature Methods*, *17*(3), 261–272. Retrieved 2024-06-11, from https://www.nature.com/articles/s41592-019-0686-2 doi: 10.1038/s41592-019-0686-2

Voight, B., & Davis, M. J. (2000, July). Emplacement temperatures of the November 22, 1994 nuée ardente deposits, Merapi Volcano, Java. *Journal of Volcanology and Geothermal Research*, *100*(1-4), 371–377. (Publisher: Elsevier) doi: 10.1016/S0377-0273(00)00146-3

Wadge, G., Biggs, J., Lloyd, R., & Kendall, J. M. (2016). Historical volcanism and the state of stress in the east African rift system. *Frontiers in Earth Science*, *4*(September). doi: 10.3389/feart.2016.00086

Werner, M. (2001, March). Shuttle Radar Topography Mission (SRTM) mission overview. *Frequenz*, *55*(3-4), 75–79. Retrieved 2020-07-24, from https://www.degruyter.com/view/journals/freq/55/3-4/article-p75.xml (Publisher: Fachverlag Schiele und Sohn GmbH) doi: 10.1515/FREQ.2001.55.3-4.75

Wibowo, H. E., Purnama Edra, A., Harijoko, A., & Anggara, F. (2018, December). Emplacement Temperature of the Overbank and Dilute-Detached Pyroclastic Density Currents of Merapi 5 November 2010 Events using Reflectance Analysis of Associated Charcoal. *Journal of Applied Geology*, *3*(1), 41. (Publisher: Universitas Gadjah Mada) doi: 10.22146/jag.42445

Wilkins, A., Green, C. P., & Ennis-King, J. (2020, November). PorousFlow: a multiphysics simulation code for coupled problems in porous media. *Journal of Open Source Software*, *5*(55), 2176. Retrieved 2024-03-25, from `https://joss.theoj.org/papers/10.21105/joss.02176` doi: 10.21105/joss.02176

Wilson, C. J. (1985, June). The Taupo Eruption, New Zealand II. The Taupo ignimbrite. *Philosophical Transactions of the Royal Society A: Mathematical, Physical and Engineering Sciences*, *314*(1529), 229–310. Retrieved 2021-03-11, from `https://royalsocietypublishing.org/doi/abs/10.1098/rsta.1985.0020` (Publisher: Royal Society Publishing) doi: 10.1098/rsta.1985.0020

Wilson, C. J. N. (1980). The role of fluidization in the emplacement of pyroclastic claws: An experimental approach. *Journal of Volcanology and Geothermal Research*, *8*(2-4), 231–249. Retrieved from `https://www.sciencedirect.com/science/article/pii/0377027380901067` (Publisher: Elsevier) doi: 10.1016/0377-0273(80)90106-7

Wolff, J. A., Ramos, F. C., Hart, G. L., Patterson, J. D., & Brandon, A. D. (2008a). Columbia River flood basalts from a centralized crustal magmatic system. *Nature Geoscience*, *1*(3), 177–180. doi: 10.1038/ngeo124

Wolff, J. A., Ramos, F. C., Hart, G. L., Patterson, J. D., & Brandon, A. D. (2008b). Columbia River flood basalts from a centralized crustal magmatic system. *Nature Geoscience*, *1*(3), 177–180. Retrieved from `www.nature.com/naturegeoscience` doi: 10.1038/ngeo124

Woods, A. W., Bursik, M. I., Kurbatov, A. V., Woods, A. W., Bursik, M. I., & Kurbatov, A. V. (1998). *The interaction of ash flows with ridges* (Tech. Rep.). Springer-Verlag. (Volume: 60)

Yale, L. B., & Carpenter, S. J. (1998). Large igneous provinces and giant dike swarms: Proxies for supercontinent cyclicity and mantle convection. *Earth and Planetary Science Letters*, *163*(1-4), 109–122. doi: 10.1016/S0012-821X(98)00179-4

Zeba, K., Rehana, A., Meghwar, S. L., Jatoi, M. A., & Shaikh, F. A. (2017). Accuracy Measurement of Google Earth Using GPS and Manual Calculations. In *International Conference on Sustainable Development in Civil Engineering (ICSDC 2017).* Pakistan. Retrieved 2021-03-11, from `https://www.researchgate.net/publication/323292318`

Ziou, D., & Tabbone, S. (1998). Edge detection techniques - an overview. *Pria*, 1–41.

Zobin, V. M. (2018, February). Development of the 10–11 July 2015 two-stage sequence of multiple emplacements of pyroclastic density currents at Volcán de Colima, México: Insight from associated seismic signals. *Journal of Volcanology and Geothermal Research*, *351*, 29–40. (Publisher: Elsevier B.V.) doi: 10.1016/j.jvolgeores.2017.12.012